Master's thesis

NTNU
Norwegian University of Science and Technology
Faculty of Engineering
Department of Mechanical and Industrial Engineering

Simen Ulleberg Tråstadkjølen

Influence of Prior Corrosion on the Fatigue Behavior of Recycled Al

Master's thesis in Mechanical Engineering
Supervisor: Nima Razavi
Co-supervisor: Aritra Sarkar
June 2024

NTNU
Norwegian University of
Science and Technology

Simen Ulleberg Tråstadkjølen

Influence of Prior Corrosion on the Fatigue Behavior of Recycled Al

Master's thesis in Mechanical Engineering
Supervisor: Nima Razavi
Co-supervisor: Aritra Sarkar
June 2024

Norwegian University of Science and Technology
Faculty of Engineering
Department of Mechanical and Industrial Engineering

NTNU
Norwegian University of
Science and Technology

Preface

This master thesis has been written to fulfill requirements for a master's degree in mechanical engineering with a specialization in product development and materials at the Norwegian University of Science and Technology (NTNU) during the spring of 2024. The work has been carried out at the Department of Mechanical and Industrial Engineering. The thesis is a continuation of a specialization project done during the autumn of 2023 by the author.

I would like to thank my supervisor Associate Professor Nima Razavi and my co-supervisor Dr. Aritra Sarkar for guidance throughout the work with this master thesis. I would also like to thank Dr. Håvard Wilson at SINTEF for assistance with laboratory work on corrosion and for guidance in assessing corrosion damage. Further I would like to thank personnel at the Department of Mechanical and Industrial Engineering at NTNU and at SINTEF for glass bead blasting, machining, and assistance in microstructure examination.

Trondheim, June 10th, 2024

Simen U. Tråstadkjølen

Abstract

This master thesis investigates the influence of prior corrosion on the high cycle fatigue behavior of a recycled 6082 aluminum alloy. Recycled aluminum alloys typically contain a high content of undesirable impurity elements compared to primary aluminum alloys. Understanding the influence of these impurities on pre-corroded fatigue can aid in determining which applications recycled alloys are suitable for.

The influence of impurities on pre-corroded fatigue was assessed by fatigue testing specimens made from a 6082 alloy containing undesirable impurities with different levels of pre-corrosion. Pre-corrosion was done by immersion in an acidic solution, containing NaCl and HCl, for different durations of time. Fatigue testing was done with the same loading conditions for all corrosion levels, comparing the resulting fatigue lives. Surface treatment with glass bead blasting prior to pre-corrosion was investigated as a possible method for improving pre-corroded fatigue behavior. Testing with several supplementary testing forms was conducted to explain the observed fatigue behavior.

Fatigue lives for pre-corroded specimens were substantially reduced compared with uncorroded specimens. This was likely the result of a severe reduction in crack initiation life caused by intergranular corrosion resulting from impurities in the recycled alloy. The difference between corrosion levels was small compared with the reduction from uncorroded to corroded. Glass bead blasting improved the uncorroded and corroded fatigue behavior. This was likely a result of introducing compressive residual stresses close to the surface. However, glass bead blasting did not improve life enough to be a viable method for improving pre-corroded fatigue for the corrosion levels tested.

Sammendrag

Denne masteroppgaven undersøker påvirkningen av tidligere korrosjon på høysyklusutmattingsoppførselen til en resirkulert 6082 aluminiumslegering. Resirkulert aluminium har typisk høyt innhold av uønskede forurensningselementer sammenlignet med nye aluminiumslegeringer. Forståelse for påvirkningen disse forurensningene har på utmatting med tidligere korrosjon kan bidra i å avgjøre hvilke bruksområder resirkulerte legeringer er egnede for.

Påvirkningen av forurensninger på utmatting med tidligere korrosjon ble undersøkt ved utmattingstesting av prøver med ulike grader av korrosjon laget av en forurenset 6082-legering. Korrosjonen ble gjennomført ved å plassere prøvene i en sur løsning, som inneholdt NaCl og HCl, i ulike varigheter. Utmattingstesting ble gjort med samme belastning for alle korrosjonsgrader, og resultatene ble sammenlignet med hensyn på utmattingslevetid. Overflatebehandling med glasskuleblåsing ble undersøkt som en mulig metode for forbedring av utmattingsoppførsel med tidligere korrosjon. Testing med flere supplerende testmetoder ble gjennomført for å forklare utmattingsoppførselen.

Utmattingslevetiden for korroderte prøver var betydelig redusert sammenlignet med ukorroderte prøver. Dette var sannsynligvis et resultat av en betraktelig reduksjon i sprekkdannelseslevetiden forårsaket av interkrystallinsk korrosjon som et resultat av forurensningene i den resirkulerte legeringen. Forskjellen mellom ulike grader av korrosjon var liten i forhold til forskjellen fra ukorrodert til korrodert. Glasskuleblåsing forbedret den ukorroderte og korroderte utmattingsoppførselen, men forbedret ikke utmattingslevetiden nok til å være en aktuell metode for forbedring av utmattingsoppførsel med tidligere korrosjon for korrosjonsgradene testet.

Contents

Figures

Tables

1. Introduction

1.1. Background

Aluminum alloys have several advantageous properties making them a preferable material choice for many applications. Due to a combination of high strength and low density, aluminum alloys often allow for design solutions with lower weight than would be possible with other material options. This is especially beneficial in the transportation sector, as it improves performance and energy efficiency. Aluminum alloys generally also have good corrosion resistance, allowing them to be used in a wide range of environments.

Production of primary aluminum alloys is a very energy demanding process. On the other hand, recycling of aluminum only requires around 5% of the energy of primary aluminum [1]. Recycling of aluminum is therefore highly beneficial, as it allows for reduction in energy consumption and improvement in utilization of natural resources. However, recycled aluminum alloys may contain a high content of undesirable impurity elements compared to primary aluminum alloys [1]. These impurities can have a negative influence on certain material properties, such as fatigue behavior and corrosion resistance.

The work done in this master thesis is part of the AluGreen project. AluGreen is a collaborative research project between several industrial partners and research institutions [2, 3]. Some notable partners in AluGreen are Norsk Hydro, SINTEF, and NTNU. The aim of AluGreen is to conduct necessary research to facilitate wider use of recycled aluminum. A key factor in this is investigating the effects of impurities on material properties.

1.2. Objective

The work described in this thesis aims to understand the influence of pre-corrosion on the high cycle fatigue behavior recycled aluminum. The content of impurity elements in recycled alloys influences both corrosion and fatigue behavior. The total influence of impurities on pre-corroded fatigue behavior is therefore a combination of both factors. The aluminum alloy investigated is a 6082 alloy with a chemical composition representing the impurities expected from recycling. The approach to achieving the objective is relating experimental fatigue behavior to characterization of prior corrosion damage, in terms of influence on crack initiation and fatigue life. In addition, surface treatment with glass bead blasting is investigated as a possible method of improving the pre-corroded fatigue behavior of the recycled alloy.

1.3. Scope

In this work, the scope is to investigate the impact and role of prior corrosion damage in fatigue failure. The influence of the chemical composition and microstructure of recycled alloys on the corrosion form and resulting surface topography is also briefly covered, to the extent that is relevant in understanding the overall effects of impurities on pre-corroded fatigue. However, the corrosion behavior in and of itself, such as corrosion mechanisms and effects of different environments, is outside the scope of this work.

This work studies the effects of prior corrosion damage on fatigue through its role in crack initiation. Corrosion-fatigue, where corrosion and fatigue loading occur simultaneously to influence crack propagation, is outside the scope of this work. The reason for testing pre-corroded fatigue as opposed to corrosion-fatigue, is that true corrosion-fatigue only occurs in very corrosive environments. Due to the impurities in recycled alloys considerably reducing corrosion resistance, very corrosive environments are not suitable areas of application for recycled alloys. Therefore, the influence of corrosion on crack initiation is of primary interest, as this is the main mechanism through which corrosion will affect fatigue behavior in most practical applications of recycled alloys.

This thesis is a continuation of a specialization project done by the author. The specialization project consisted of a literature review on pre-corroded fatigue and corrosion-fatigue in heat treatable aluminum alloys and on recycling methods for aluminum. In addition, preliminary corrosion testing and baseline fatigue testing on uncorroded specimens was also done. Direct use of work from the specialization project in this thesis is specified when applicable.

2. Theory and Literature Review

This chapter provides background theory on topics relevant in assessing the influence of pre-corrosion on recycled aluminum alloys. Topics covered are background on aluminum alloys, background on corrosion with emphasis on intergranular corrosion in 6000-series aluminum, and background on fatigue and influencing factors relevant to this thesis. The literature review section provides a description and comparison of existing literature on fatigue behavior of pre-corroded 6000-series aluminum alloys. Finally, relevant results from prior corrosion testing in AluGreen are presented.

2.1. Aluminum Alloys

This section provides background theory on the designation of aluminum alloys by composition and temper, the age hardening mechanism, a description of the alloy investigated in this thesis, 6082, and finally a description of the main challenges with the properties of recycled aluminum alloys.

2.1.1. Aluminum Alloy Designations

Aluminum is commonly alloyed with other elements to create aluminum alloys with improved properties compared with pure aluminum. As with other alloys, the alloying elements can take different positions in the microstructure [4]. The atoms of the alloying elements can be dissolved into aluminum matrix in substitutional or interstitial positions or form precipitates as pure or intermetallic phases in the microstructure. The distribution of alloying elements in the microstructure is in large part determined by production process and thermal history of the material. The alloying elements and their distribution in the microstructure together play a major role in determining the alloys properties. Alloying elements are typically added to improve the tensile strength of alloys. However, this can have undesirable side effects such as decreased corrosion resistance, ductility, and fatigue strength.

For classifying wrought aluminum alloys, a four-digit number is assigned based on its chemical composition [4, 5]. Aluminum alloys based on the same primary alloying elements often have similar properties and applications. Therefore, aluminum alloys are categorized into series by chemical compositions based on their primary alloying elements. This is represented by the first number in the four-digit alloy designation. Table 1 provides an overview of the wrought aluminum series, and their defining alloying elements.

Table 1: Wrought aluminum alloy series. Adapted from [4] and [5].

Wrought alloy series	Defining alloying element(s)
1XXX	None, >99% Al
2XXX	Cu (or Cu and Li)
3XXX	Mn
4XXX	Si (or Si and Mg)
5XXX	Mg
6XXX	Mg and Si
7XXX	Mg and Zn
8XXX	Other

In addition to chemical composition, the processing and heat treatment conditions are determining factors in the properties of an aluminum alloy [4]. This is referred to as the temper of the alloy. The temper state is designated by a letter and potentially a number following the four-digit number designating the chemical composition [4, 5]. Table 2 shows the temper designation for aluminum alloys.

Table 2: Aluminum alloy temper designations. Adapted from [4] and [5].

Temper	Description
F	As-fabricated (hot worked, forged, cast, etc.).
O	Annealed.
H	Cold worked. Followed by a number to designate the level of cold working.
W	Solution treated.
T	Age hardened. Followed by a number to designate the aging process.

2.1.2. Age Hardening

Age hardening, also known as precipitation hardening, is a heat treatment process that can be used for some aluminum alloys depending on their chemical composition [4]. Age hardening can be done for 2000-series, 6000-series, 7000-series, and 8000-series alloys, and these series are therefore often referred to as heat-treatable or age hardenable [4]. 4000-series can also be heat-treatable depending on the composition [4]. The following paragraph provides a description of the age hardening process based on [4].

The age hardening process starts with solution treatment. In this step the alloy is heated to where the alloying elements are dissolved into the aluminum matrix. The alloy is then rapidly cooled, quenched, to room temperature. This prevents the alloying elements from diffusing out of the matrix, as diffusion of atoms requires some time. As a result, the microstructure becomes a supersaturated solid solution, where the aluminum grains contain a higher content of dissolved foreign atoms than what would normally be stable at room temperature. This is called a

metastable condition. After solution treatment, the alloy is aged by heating the material to a controlled temperature for a prescribed length of time. At this elevated temperature the foreign atoms can slowly diffuse out of the aluminum matrix to form uniformly distributed inclusions of precipitate phases. This increases the strength of the alloy. If the alloy is at this elevated temperature for too long, the uniformly distributed precipitates will join up to form larger inclusions. This is generally undesirable as it decreases the strength of the alloy.

An aging state where the aging has not advanced to where the alloy has reached its maximum strength is referred to as under-aging. Peak-aging refers to the aging state where the alloy is aged to its maximum strength, generally meaning the alloying elements form uniformly distributed precipitates in the microstructure. Over-aging refers to the condition where the alloy is aged past its maximum strength and the alloying elements have joined to form larger inclusions. Some alloys can be aged at room temperature, this is referred to as natural aging [4, 5]. Natural aging requires more time to produce peak aging but prevents over-aging [4]. Aging at an elevated temperature is referred to as artificial aging [4, 5]. Table 3 presents the designations for different aging conditions.

Table 3: Age hardening designations. Adapted from [4] and [5].

Age hardening designation	Aging process
T1	Cooled from fabrication temperature and naturally aged.
T2	Cooled from fabrication temperature, cold worked, and naturally aged.
T3	Solution treated, cold worked, and naturally aged.
T4	Solution treated and naturally aged.
T5	Cooled from fabrication temperature and artificially aged.
T6	Solution treated and artificially aged.
T7	Solution treated and stabilized by over-aging.
T8	Solution treated, cold worked, and artificially aged.
T9	Solution treated, artificially aged, and cold worked.
T10	Cooled from fabrication temperature, cold worked, and artificially aged.

2.1.3. 6082 Aluminum Alloy

6000-series aluminum alloys are used in a wide range of applications due to having a good balance of advantageous properties, such as being heat treatable to high strength, good corrosion resistance, formability, and weldability [6]. The defining alloying elements are Mg and Si. These alloying elements form the intermetallic phase Mg_2Si, which is the main strengthening phase in the alloy [7]. Precipitation of Mg_2Si makes 6000-series alloys age

treatable [7]. Other alloying elements commonly added to alloys in the 6000-series to improve their mechanical properties are Cu, Mn, and Cr [7].

6082 is one of the commonly used alloys from the 6000-series. It is typically formed through extrusion, stamping, or rolling. 6082 is one of the strongest of the commonly used 6000-series alloys, with a yield strength up to around 310 MPa with heat treatment [8]. Table 4 presents the chemical composition of 6082.

Table 4: Chemical composition of 6082 [8, 9].

Alloying element	Content [wt.%]
Cr	<0.25
Cu	<0.1
Fe	<0.5
Mg	0.6 - 1.2
Mn	0.4 -1.0
Si	0.7 - 1.3
Ti	<0.1
Zn	<0.2
Al	Balance

2.1.4. Recycled Aluminum

Recycling of aluminum is very advantageous due to recycling of aluminum only requiring a small fraction, around 5%, of the energy needed to produce primary aluminum [1, 10]. Aluminum is not found in a pure state naturally. New aluminum is primarily made from extracting alumina, aluminum oxide (Al_2O_3), from Bauxite ore with the Bayer process [1]. Aluminum is then refined from the alumina by electrolysis with the Hall-Héroult process [1]. The electrolysis process is very energy demanding. Recycled aluminum, or secondary aluminum, is made from remelting aluminum scrap and is far less energy demanding. In addition to requiring less energy, recycling of aluminum also reduces waste and slows depletion of available Bauxite as a natural resource [1]. New methods based on solid state recycling, removing the need for remelting, are being developed to further reduce the energy consumption of recycling aluminum [11].

The primary challenge with recycled aluminum is that it generally has a considerable content of undesirable impurity elements [1]. These impurities have a negative impact on the properties of the resulting material [1]. The content of many undesirable impurities is difficult to control or remove compared with other metals [12]. One of the most challenging impurities is Fe, which is usually found in greater quantities in recycled aluminum compared to primary aluminum [1]. Fe forms brittle intermetallic compounds that greatly affect the mechanical properties of aluminum alloys. Technologies exist to control the content of impurities in aluminum alloys both by improving physical scrap sorting before remelting and by chemical separation during remelting [12]. However, techniques enabling production of recycled aluminum with low impurity levels are costly and can be energy demanding [12].

The presence of impurities makes recycled aluminum unsuited for use in many alloys intended for demanding application, which have strict requirements for chemical composition [10]. Recycled aluminum is therefore primarily used in cast alloys and low grade wrought alloys which do not have as strict requirements [10]. For use in higher grade alloys, recycled aluminum needs to be mixed with primary aluminum to reduce the overall fraction of impurities [10, 12]. This limits the extent of aluminum recycling compared with primary aluminum production [12]. As will be explained in the next section, some properties, such as corrosion resistance, are highly sensitive to changes in chemical compositions. Therefore, even variation in composition resulting from recycling within the chemical composition limits set by the relevant standards may have a considerable influence on an alloy's properties.

2.2. Corrosion

Corrosion of metals refers to mechanisms where material is deteriorated from reacting with the environment [13]. Corrosion can be either chemical or electrochemical depending on the material and environment. This section provides background on the fundamental mechanism of electrochemical corrosion, some important concepts for corrosion in aluminum alloys, and a description of intergranular corrosion in 6000-series aluminum alloys and why this corrosion form is particularly relevant for recycled alloys.

2.2.1. Electrochemical Corrosion

In metals, the most common form of corrosion is electrochemical corrosion [14]. Electrochemical corrosion occurs when an electrochemical cell is formed between two areas of one metal, or between two different metals, connected electrically and in contact with an electrolyte solution. Two electrochemical reactions occur in the electrochemical cell, one at the anode and one at the cathode [14]. The reaction at the anode is called an oxidation reaction. At the anode, electrons are lost the cathode through the physical electric connection and the metal atoms become ions and dissolve in the electrolyte or form stable metal oxides. The reaction at the cathode is called a reduction reaction. Different reduction reactions can occur depending on the metal and the electrolyte [14]. Corrosion products in the form of solids, liquids or gases are formed at the cathode [14].

For corrosion of a single metal, different areas may act as the cathode and anode due to local differences in electrode potential that can occur from several factors [14]. Some of the potential reasons are local differences in chemical composition, grain structure, mechanical stresses, and differences in concentration of the reactive elements in the electrolyte between different surface areas [14]. The anodic and cathodic areas can change and move over time as corrosion progresses [14].

2.2.2. Corrosion in Aluminum

Aluminum rapidly reacts to form a thin oxide layer covering the surface when exposed to the atmosphere [15]. This oxide layer prevents further corrosion. As a result, aluminum and aluminum alloys generally show good corrosion resistance in many environments [15]. This is known as passivation. However, the natural oxide layer on aluminum contains weaknesses that can allow for initiation of corrosion in aggressive environments. Whether the oxide layer is

capable of hindering corrosion depends on several factors, notably the environment and the chemical composition of the alloy. As a result, aluminum alloys can be almost completely resistant to corrosion in some environments and corrode rapidly in others.

Corrosion in aluminum can occur in different forms depending on the alloy and environment. Typical corrosion forms in bare aluminum alloys are localized corrosion forms such as pitting corrosion and intergranular corrosion [15]. Uniform corrosion, which is common in other metals, is not typically seen in aluminum due to the passive oxide layer [15]. Uniform corrosion of aluminum alloys is usually only observed in aggressive conditions with very low or high pH, where the oxide layer loses its protective effect entirely [15].

Pitting corrosion is a common form of corrosion in aluminum alloys [15]. Pitting corrosion refers to the formation of small corrosion pits on the surface which grow in number and size as corrosion progresses. Corrosion pits are formed when weak sites of oxide layer are broken down, exposing the underlying aluminum to the electrolyte [13, 15]. An electrochemical cell is formed between the exposed aluminum in the pit and particles penetrating the oxide layer connecting the aluminum to the electrolyte. The bottom of the pit becomes the anode and rapidly corrodes. This leads to an increased electrolyte concentration in the pit, further accelerating the corrosion there [15].

Intergranular corrosion is another important corrosion form in aluminum alloys, particularly in heat treatable alloys [15]. Intergranular corrosion is localized to the grain boundaries, and grows along these from the surface into the material [13, 15]. This is caused by precipitate phases at or close to the grain boundaries. Differences in the electrode potential between particles, phases, and the aluminum grains can lead to formation of electrochemical cells at the grain boundaries driving intergranular corrosion [13]. Which phases and particles drives intergranular corrosion depends on the chemical composition and microstructure of the alloy.

Overall, it is worth noting that the extent and form of corrosion observed in aluminum alloys is very sensitive to a variety of different factors. Only minor changes in composition, microstructure, or temper can drastically affect how an aluminum alloy corrodes.

2.2.3. Intergranular Corrosion of 6000-series Aluminum Alloys

6000-series aluminum is normally more resistant to intergranular corrosion than other heat treatable alloy series such as the 2000- and 7000-series [16]. However, they can be susceptible to intergranular corrosion depending on chemical composition and microstructure. In 6000-series alloys the intergranular corrosion mechanism is usually related to the excessive amounts of Si [13, 16] or the presence of Cu at the grain boundaries [17]. However, other alloying elements, such as Zn, can also contribute to increased susceptibility to intergranular corrosion [18]. The distribution of Cu in the microstructure is influenced by processing conditions such as the forming process and heat treatment [19]. As Cu is one of the undesired impurities that can be found in recycled 6000-series aluminum alloys, they can be expected to be susceptible to intergranular corrosion.

The content of Cu is the main determining factor in intergranular corrosion in 6000-series aluminum alloys [20, 21]. The most important phases in relation to intergranular corrosion is

the Q-phase, which is an intermetallic phase consisting of Al, Mg, Si and Cu which typically forms coarse particles at the grain boundaries, and a continuous Cu film formed along the grain boundaries [19]. Both these phases are cathodic to precipitate free zones of the Al grains close to the grain boundaries [20]. This allows for an electrochemical cell between the precipitate phases and precipitate free zones, causing the anodic Al matrix along the grain boundaries to corrode and being dissolve. The Cu containing microstructure allowing for intergranular corrosion in 6000-series alloys is shown in Figure 1. Other alloying elements than Cu can also influence intergranular corrosion by forming other active phases at the grain boundaries [20].

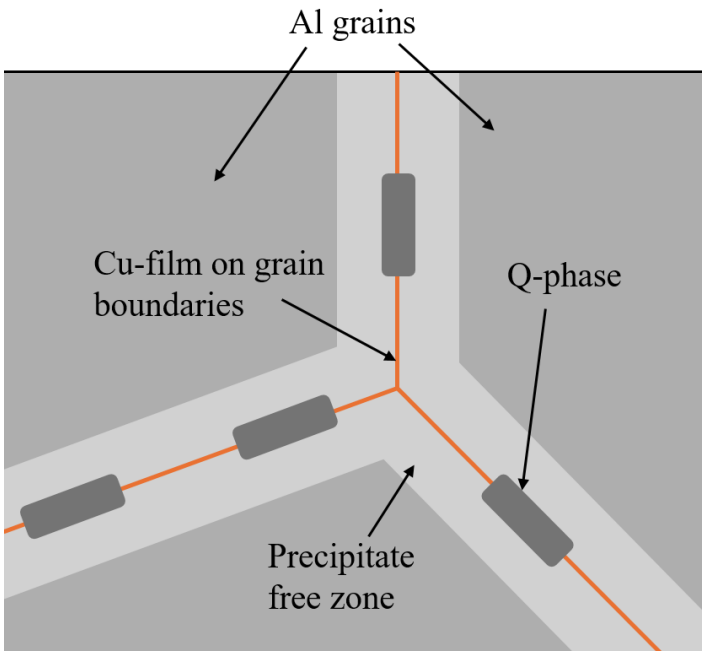

Figure 1: Distribution of Cu in age hardened 6000-series aluminum alloys. Adapted from [19].

Heat treatment can be a determining factor in determining susceptibility to intergranular corrosion, depending on the alloy composition [19]. This is due to influencing the distribution of alloying elements as particles or intermetallic phases. In 6000-series aluminum with Cu, the distribution of Cu at the grain boundaries is greatly affected by aging [19]. Which aging levels facilitate intergranular corrosion, pitting corrosion, or decreases susceptibility to corrosion depends on alloy and production process. Typically, under-aged conditions cause rapid intergranular corrosion, due to having continuous Cu films along the grain boundaries [19]. As the alloy in aged more the Cu accumulated in larges particles and the continuous film is broken up. This can increase the alloy's resistance to intergranular corrosion [19]. With further aging, precipitates of alloying elements accumulate to form larger particles [19]. This can cause the main corrosion form to change from intergranular corrosion to pitting corrosion [19]. Different relationships between aging level and intergranular corrosion susceptibility are possible, with the most severe intergranular corrosion occurring when under-aged [19], peak-aged [20], or over-aged [21].

2.3. Fatigue

This section describes the mechanism responsible for fatigue failure in metals, the stress based and crack growth approaches to describing fatigue, and finally factors influencing fatigue which are relevant to fatigue of extruded aluminum alloys with pre-corrosion and glass bead blasting.

2.3.1. Fatigue Mechanism

Fatigue is the failure of a material from repeated cycles of mechanical loading [22]. The fundamental mechanism behind fatigue failure is the formation and growth of a crack that gradually decreases the load bearing cross section. Once the cross section is reduced to where remaining cross section cannot support the load, final fracture occurs.

As real dynamic loading situations can be complicated, fatigue loading is usually considered as a sinusoidal curve alternating between a maximum and minimum stress level [22]. If an observed or predicted loading history includes a combination of cycles at different loading ranges, this can also be considered. Table 5 presents commonly used values for quantifying fatigue loading.

Table 5: Fatigue loading definitions. Adapted from [22].

Symbol	Description/definition	Unit
σ_{max}	Maximum stress level during loading cycle	MPa
σ_{min}	Minimum stress level during loading cycle	MPa
$\sigma_a = \frac{\sigma_{max} - \sigma_{min}}{2}$	Alternating stress / Stress amplitude	MPa
$\sigma_m = \frac{\sigma_{max} + \sigma_{min}}{2}$	Mean stress	MPa
$\Delta\sigma = \sigma_{max} - \sigma_{min}$	Stress range	MPa
$R = \frac{\sigma_{min}}{\sigma_{max}}$	Stress ratio	Unitless
N_f	Fatigue life	Cycles

A materials response to fatigue loading can be described in three stages [23]. First is crack initiation, where highly localized plastic deformation leads to damage accumulation until the formation of a fatigue crack. This usually occurs from defects at the surface. Once a fatigue crack is initiated, the crack propagation stage begins. During this stage the fatigue crack grows steadily across the cross section of the material. Once the fatigue crack has grown such that the remaining area can no longer support the applied load, the material will reach final fracture.

2.3.2. Stress Based Approach

The relation between applied alternating stress and resulting fatigue life is described with an S-N curve [22]. Figure 2 shows an S-N curve representing the typical fatigue behavior of a metal. The S-N curve is generated from fatigue testing a material at several stress levels. Fatigue testing generally has a substantial amount of scatter in the results. This means that many tests

are required to provide solid statistical basis for the S-N behavior. It also means the fatigue life can only be approximately predicted based on the experimental data.

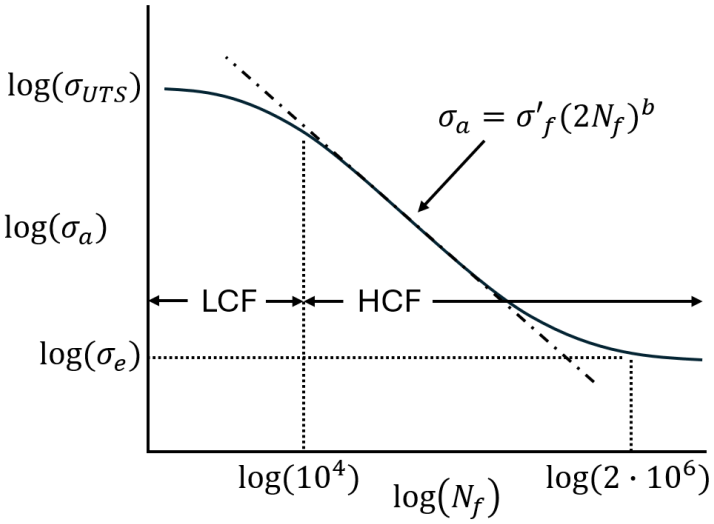

Figure 2: S-N curve. Made by author.

A distinction is often made between low cycle fatigue (LCF) and high cycle fatigue (HCF) [22, 23]. In LCF a crack is initiated early, and most of the fatigue life is spent in the crack propagation stage. Therefore, the fatigue resistance is primarily determined by resistance to crack growth, which correlates with the ductility of the material. In HCF most of the fatigue life is spent in the crack initiation stage, with crack propagation taking up a proportionally smaller fraction of the total fatigue life. Therefore, fatigue resistance in HCF is primarily determined by resistance to crack initiation, which correlates with tensile strength. Surface defects and other features that facilitate crack initiation severely affect fatigue life in HCF, while having a smaller influence in LCF as a fatigue crack is initiated quickly regardless. The transition from LCF to HCF varies with material but usually occurs between 10^2 to 10^4 cycles [22].

At a low enough stress level, a material can potentially withstand any number of loading cycles without crack initiation [22]. This maximum stress level allowing for infinite life is referred to as the fatigue limit or endurance limit. The S-N curve usually approaches this level at around $2 \cdot 10^6$ cycles. Some metals, such as steels, have a clearly defined endurance limit where the S-N curve flattens to a horizontal line [22]. Some other metals, such as aluminum, do not have a true endurance limit [22]. However, the slope of the S-N curve usually becomes substantially less steep past around $2 \cdot 10^6$. Therefore, the fatigue limit term is also commonly used for aluminum, but with the knowledge that an applied stress under this limit will not truly result in infinite life.

Within the finite life area in HCF regime, the S-N behavior of a material follows a power law relation [22, 23]. This power law can be expressed with Basquin law, Equation 1. The coefficients in the Basquin law are determined experimentally. The Basquin law is applicable from the transition from LCF to HCF and up to where the S-N curve approaches endurance limit. σ_a is applied alternating stress in MPa, N_f is fatigue life in cycles, and σ'_f in MPa and the unitless b are the experimentally determined coefficients.

$$\sigma_a = \sigma'_f \left(2N_f\right)^b \quad (1)$$

The alternating component of the stress is responsible for driving crack initiation and growth leading to fatigue failure. However, the mean stress component also has a considerable influence on fatigue life [22]. Stresses in the tensile direction are primarily responsible for crack initiation and propagation. Therefore, the higher the tensile stresses involved in the loading condition are, the lower the fatigue life. This is accounted for with mean stress corrections, correcting the alternating stress to an equivalent fully reversed alternating stress level. Several mean stress corrections are used depending on the application and material. Some common methods are the Goodman equation, Gerber equation, and Smith, Watson, and Topper (SWT) equation [22, 23].

2.3.3. Crack Growth Approach

As the fundamental mechanism in fatigue is the initiation and growth of a crack, concepts from fracture mechanics can be applied to describe fatigue from a crack growth perspective [23, 24]. The crack growth approach is based on relationship between the crack growth per cycle, *da/dN* and the stress intensity factor range, *ΔK*. The stress intensity factor quantifies the magnitude of the stress field at the tip of a sharp crack. The stress intensity factor *K* is a function of both the applied stress and the length of the crack by Equation 2. The equation is adjusted to fit the geometry of each case with a geometric factor *F*. *F* is usually close to 1. *K* in the stress intensity factor in MPa·m$^{0.5}$, *F* is the unitless geometric factor, *σ* is applies stress in MPa, and *a* is the crack length in m.

$$K = F\sigma\sqrt{\pi a} \quad (2)$$

In fatigue crack growth the crack growth rate can be expressed as a function of the stress intensity factor range with the Paris law [23, 24], Equation 3. *C* and *m* are material coefficients which are obtained experimentally. *m* is unitless, and with *da/dN* in mm/cycle and *ΔK* in MPa·m$^{0.5}$, *C* has unit (mm/cycle)/(MPa·m$^{0.5}$)^m.

$$\frac{da}{dN} = C(\Delta K)^m \quad (3)$$

The Paris law is valid within the stable crack propagation phase of fatigue. In the crack initiation and early crack propagation phase this law does not apply. The Paris law also does not apply for the unstable crack growth seen in the last cycles before final failure. Figure 3 shows the shape of curve relating *da/dN* to *ΔK*, where the Paris law is applicable for stable growth area in the middle of the curve. The curve starts from ΔK_{th}, which is the threshold stress intensity factor required for a crack to propagate. The curve ends at ΔK_{cr}, which represents the critical stress intensity factor required for fracture of the remaining cross section.

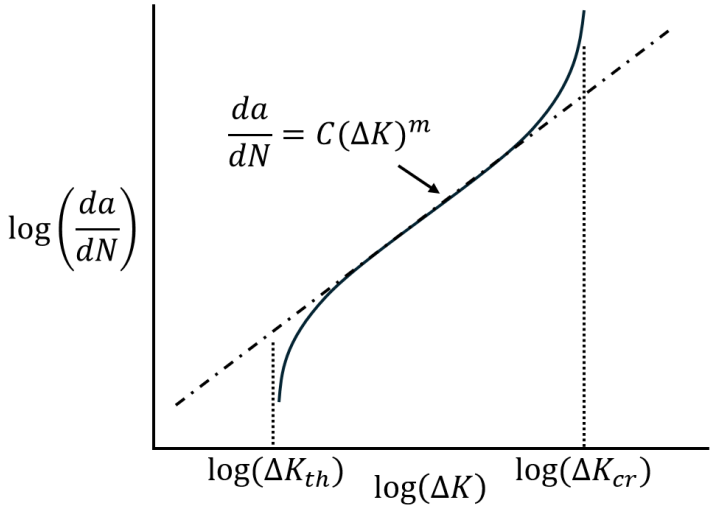

Figure 3: Crack growth rate curve. Made by author.

The number of cycles required for crack growth from one crack length to another within the stable crack growth area can be predicted from the Paris law [23, 24]. Assuming *F* to be constant within the crack growth interval considered, the Paris law can be rewritten and integrated to solve for *N*, as shown in Equations 4 and 5.

$$\int_0^{N_f} dN = \int_{a_i}^{a_f} \frac{da}{C(\Delta K)^m} \tag{4}$$

$$N_f = \int_{a_i}^{a_f} \frac{da}{C(F\Delta\sigma\sqrt{\pi a})^m} \tag{5}$$

The Paris law coefficients usually represent the crack growth for zero-to-tension loading, $R = 0$. To apply the Paris law to other stress ratios, *C* and *m* must be determined for these stress ratios [24]. The Walker equation, Equation 6, is a commonly used approach for correcting for stress ratio [24]. The Walker equation introduces a new material coefficient, γ, to represent the stress ratio sensitivity of the material and is determined experimentally, this value is usually around 0.5 [24]. With this, *C* can be determined for any stress ratio. The coefficient *m* is considered to not be affected by the stress ratio with the Walker equation [24].

$$C = \frac{C_0}{(1-R)^{m(1-\gamma)}} \tag{6}$$

To describe the fatigue behavior of materials with known defects, the root area method can be applied [25]. This approach is based on relating the fatigue life to the initial stress intensity factor at the start of the fatigue life [26]. In this way the applied stress, defect size, and specimen geometry are all included as part of the stress intensity factor. As a result, the relation is independent of the defect size in the material. As the defects may not be shaped as fatigue cracks, the crack length is replaced with the square root of the defect area in calculating the

stress intensity factor, as shown in Equation 7. For surface defects, the geometric factor for a small defect areas is $F = 0.65$ [25].

$$K_{max} = 0.65\sigma_{max}\sqrt{\pi\sqrt{area}} \tag{7}$$

As mentioned, if the alternating stress is sufficiently low, a crack will not initiate. However, with a crack or defect already present, the threshold stress level for this crack to propagate will be affected. A Kitagawa-Takahasi (KT) diagram shows the threshold stress range as a function of defect area [27]. Figure 4 shows a KT-diagram. Up to certain defect size, a_0, the threshold stress for crack propagation is independent of defect area and remains at the endurance limit. Over this defect size, the threshold stress is controlled by the defect area.

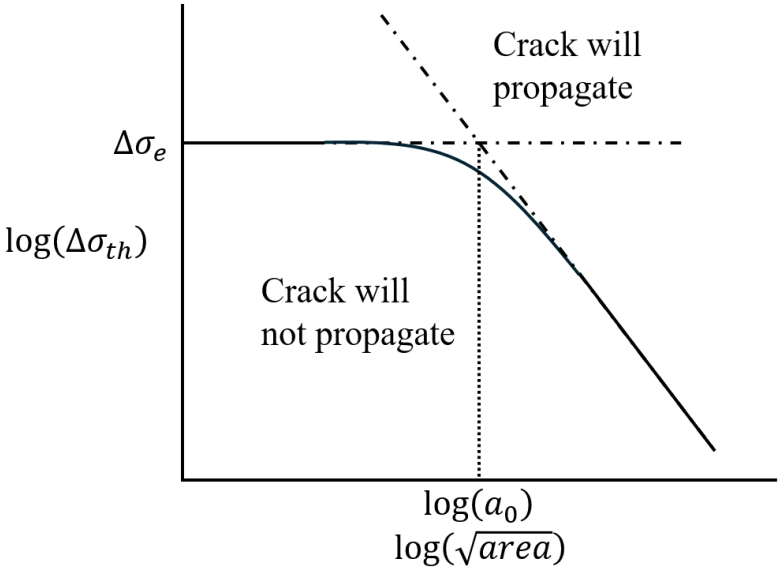

Figure 4: Kitagawa-Takahasi (KT) diagram. Made by author.

2.3.4. Factors Influencing Fatigue

Many factors influence the fatigue behavior of a material and may cause the behavior to deviate from the S-N curve for an ideal polished specimen. The following paragraphs introduce some influencing factors that are relevant in assessing the influence of pre-corrosion and glass bead blasting on the fatigue behavior of an extruded aluminum alloy.

Microstructure

Microstructure has a considerable effect on the fatigue resistance of a material. Like tensile strength, fatigue strength is generally improved by a finer grain structure, higher dislocation density, and uniformly distributed strengthening phases [22]. In fatigue, foreign particles can also contribute the initiation of cracks. However, this is minimized with uniformly distributed particles of small size [28]. A fine grain structure improves crack initiation life from grain boundaries stopping or slowing development of microcracks [28]. On the other hand, larger grains can result in roughness and plasticity induced crack closure resulting in reduced crack growth rate [29]. An elongated grain structure resulting from forming processes, such as rolling or extrusion, generally improves fatigue resistance in the elongated direction [22]. Work

hardening from cold working also generally improves fatigue behavior. As discussed, overall fatigue resistance is a function of both strength and ductility, where strength primarily controlling crack initiation and ductility controlling crack propagation. Therefore, changes to microstructure reducing the ductility of the material can negatively affect fatigue resistance, especially when crack propagation represents a substantial part of the fatigue life.

Notches

Geometric discontinuities such as corners, holes, and grooves lead to increased local stresses, and are referred to as notches in relation to fatigue [30]. Notches facilitate crack initiation and therefore reduce fatigue resistance. To account for notch effects in design against fatigue, the nominal stress is corrected with a stress concentration factor. However, the theoretical stress concentration factor overestimates the impact of notches compared with experimental results, particularly with small radius notches [30]. Therefore, the fatigue stress concentration factor is calculated based on the theoretical stress concentration factor and a notch sensitivity factor, accounting for the notch radius and the notch sensitivity of the material, which is generally lower with lower tensile strength and higher ductility [23]. The influence of notches is most significant on the fatigue limit and in high cycles fatigue. For shorter fatigue lives, the effective stress concentration effect is reduced to below what the fatigue stress concentration factor represents [30].

Surface Finish

Surface finish has a major influence on fatigue life [23, 30]. Surface roughness acts as many small notches in the specimen surface. This results in stress concentration increasing the effective stress contributing to crack initiation in valleys and pits of the surface topography [23]. In addition, different surface finishes are typically associated with other surface effects influencing fatigue from processing, such as cold working or residual stresses [23, 30]. In fatigue design, surface finish is accounted for by reducing the fatigue limit by a modifying factor [23]. Empirical data is used for determining the modifying factor for normal surface finishes, such as ground, machined, and hot rolled surfaces. The sensitivity to surface roughness varies with strength and ductility of the material, like the notch sensitivity [23]. High surface roughness can reduce the fatigue limit to under half of that of a polished specimen for high strength alloys with poor surface finishes. Both size and shape of the surface topography plays into the influence of surface roughness on fatigue [31]. Therefore, characterizing surface finish in terms of surface roughness values such as *Ra* does not necessarily reflect the impact the surface finish has on fatigue. In addition, as a fatigue crack initiates from the most favorable site, meaning local features of the surface topography are more important than the average over the entire surface.

For extruded aluminum profiles, the extrusion die leaves grooves along the length of the profile. This affects fatigue life when loading is applied transversely to the extrusion lines [32]. When loading is applied along the direction of extrusion lines, the fatigue life is similar to polished specimens [32]. An elongated grain structure from extrusion generally leads to improved mechanical properties in the extrusion direction [22]. However, if a recrystallized layer with large equiaxed grains is present, the direction of loading with respect to extrusion direction is

insignificant for polished specimens, as crack initiation resistance is controlled by the microstructure of the surface layer [32].

Corrosion

Corrosion influences fatigue in two main ways. Firstly, corrosion damage can act as notches in the surface, facilitating crack initiation [22]. A material in service in a corrosive environment can over time accumulate corrosion damage severe enough that the applied loading causes crack initiation. For a loading level that would normally result in infinite life, corrosion damage may lead to substantial reduction in fatigue limit. For a loading level giving finite life this causes a reduction in fatigue life compared with an uncorroded surface. Different corrosion forms may differ in their influence on fatigue. Intergranular corrosion is generally worse than corrosion pitting due to the damage being sharper [16].

In more aggressive environments corrosion can also act together with fatigue crack growth to increase the crack propagation rate [22]. The crack growth per cycle will in this case be the combination of fatigue crack growth from the applied loading and crack growth from corrosion. This phenomenon is called corrosion-fatigue. Corrosion-fatigue only occurs when the environment and loading conditions, particularly the loading frequency, allows for a significant amount of corrosion between each loading cycle. Note that this project does not investigate corrosion-fatigue but focuses exclusively on the influence of corrosion damage on crack initiation.

Compressive Residual Stresses

Introduction compressive residual stresses close to the surface of a material is an effective way of improving fatigue behavior. Compressive residual stresses aid in counteracting applied tensile stresses working to open cracks, effectively leading to a state of compressive mean stress locally [22]. Compressive residual stresses both increases resistance to crack initiation and reduces crack growth rate through areas of the material where compressive residual stresses are present. Compressive residual stresses in the surface are introduced by stretching the surface layer so that the underlying material counteracts this by compressing the surface layer [22]. Various processes can introduce compressive residual stresses. Some surface treatments that are used for this are shot peening, ball burnishing, and laser peening [33, 34]. Residual stresses can also be created in forming processes. There will typically be a correlation between and increased hardness and compressive residual stresses.

2.4. Literature Review

The aim of the work described in this thesis was to investigate the influence of prior corrosion on the fatigue behavior of a recycled 6082 aluminum alloy. To understand how pre-corrosion likely impacts the fatigue behavior of this alloy, the most relevant literature to the research question was studied and compared in detail. The criteria for selecting literature were that the studies had to investigate fatigue behavior in terms of fatigue life for pre-corroded 6000-series aluminum alloys. Special cases, such as welds, wires, and surface treatments, coating, and similar, were excluded due to not being directly comparable with base material results. The four studies which met the criteria are presented in Table 6. This section provides an overview of

scope and approaches in these studies, compares their main results and findings, and finally summarizes the findings established in the literature and the main knowledge gaps.

Table 6: Literature on fatigue of pre-corroded 6000-series aluminum alloys.

Year	Authors	Alloy	Reference
2012	Almaraz, Ambriz & Calderón	6063-T5	[35]
2013	Abdulstaar, Mhaede & Wagner	6082-T6	[36]
2017	Weber, Eason, Özdes & Tiryakioglu	6061-T6	[37]
2020	Muñoz, Buenhombre, García-Diez, Fabal & Dìaz	6082-T6	[38]

2.4.1. Approach

This section describes the approaches used by each study. All studies conducted fatigue testing of specimens with several levels of corrosion, comparing the results to those for uncorroded specimens. The studies all used accelerated corrosion processes to introduce corrosion damage. However, the studies varied considerably in the choice of pre-corrosion procedure. In addition, they varied in their approach for characterization and quantification of the corrosion damage and in how corrosion damage was correlated to resulting fatigue performance. All studies conducted fatigue testing at several stress levels and at several levels of corrosion damage, although the stress levels and number of corrosion levels varied between the studies.

Corrosion Procedure and Characterization

Weber *et al.* subjected 6061-T6 to immersion in a solution of 3.5% NaCl and HCl in water, giving pH 2 for the resulting solution. One set of specimens were immersed for 2 days and another for 24 days. The condition of the material when subjected to the pre-corrosion procedure was the machined rotating beam specimens with polished surfaces. Characterization of corrosion was done by examining surfaces and cross sections of the corroded specimens with SEM. Corrosion pitting along the grain boundaries was identified as the main form of corrosion. The quantification of the corrosion damage presented in the paper was only the dimension of one representative pit for 2 days of corrosion and 24 days respectively.

Almaraz *et al.* subjected 6035-T5 to an HCl solution with pH 0.8. Three immersion durations were used, 2, 4, and 6 minutes. The surface condition before corrosion was machined with no grinding or polishing. Corrosion pitting was observed as the corrosion form. The corrosion was characterized with optical microscopy in terms of the resulting corrosion pit surface diameters, and the crack initiating pits were quantified by their surface diameter and depth.

Munõz *et al.* pre-corroded specimens of 6082-T6 in a salt spray chamber with a corrosive solution containing 5% NaCl and with a pH of 6.5. The salt spray pressure was 0.9 to 1 bar and the temperature in the chamber was 35°C. Specimens were corroded for 1, 2, and 3 months, and compared in fatigue to uncorroded reference specimens. The surface condition of the specimens prior to corrosion was from rolling on the sheet surface and machined on the edges. The severity of corrosion damage was characterized in terms of pit density, diameters, and depths within a sample area of the specimen surfaces. This was done with confocal microscopy.

Abdulstaar *et al.* subjected specimens of 6082-T6 to immersion in 3.5% NaCl solution. In this study the influence of different surface treatments was also within the scope, so specimens were tested with electropolished, ball-burnished, and shot peening surfaces. Electropolished specimens were tested at many corrosion durations, ranging from 0 to 100 hours, at one loading condition. In addition, all surface treatment conditions were tested at different load levels uncorroded and with 100 h of pre-corrosion. This study did not provide any quantification of the severity of the corrosion damage at all. As a result, the resulting fatigue performance was related directly back to the corrosion condition and duration, rather than through a quantification of the damage that could be used for comparison other corrosion conditions.

Fatigue Testing

Weber *et al.* and Almaraz *et al.* both did fatigue testing by rotating bending at a wide range of stress levels, from close to the materials yield stress down to a level that gave fatigue lives over 10^6. From this S-N curves were made for each of the corrosion conditions tested. Munõz *et al.* similarly conducted fatigue testing at a range of stress levels. However, the loading type was axial loading with a stress ratio $R = 0.1$. Munõz *et al.* tested each corrosion level with different stress levels, adjusted for the expected fatigue behavior.

Abdulstaar *et al.* conducted fatigue testing with rotating bending. Fatigue testing was done at one fixed stress level for a wide range of corrosion conditions to study the relation between fatigue life to corrosion level. In addition, testing was done with a range of stress levels for uncorroded and maximum corrosion for the different surface treatments. From this, S-N curves for each condition were made. The stress level for varying corrosion levels was an alternating stress of 165 MPa, 47% of the yield strength, giving fatigue lives in the 10^5 to 10^6 range.

2.4.2. Results and Findings

This section summarizes the main results and findings from the studies in terms of corrosion damage, fatigue behavior, and additional work or analysis.

Corrosion

Weber *et al.* presented representative corrosion pit dimensions for the two corrosion conditions tested. After 2 days a pit had a diameter of 7.8 µm and a depth of 2.0 µm. A pit after 24 days had a diameter of 7.6 µm and a depth of 7.7 µm.

Almaraz *et al.* stated that the crack initiation pitting holes for 2 minutes of corrosion ranges from 115 to 180 µm in diameter and 40 to 80 µm in depth. For 4 minutes of corrosion the values were 145 to 240 µm in diameter and 55 to 110 µm in depth. The paper did not provide values for corrosion pit dimensions for the last corrosion duration, 6 minutes.

Abdulstaar *et al.* did not do any extensive characterization of the corrosion. No quantification of the level of corrosion after any duration of corrosion testing was provided in the paper. The characterization of corrosion that was available from this paper is only SEM images of the surface for some corrosion times. In these images, corrosion pits were observed. Higher number of and larger pits were observed with increasing corrosion duration.

As mentioned, Munoz *et al.* used several values for quantifying the degree of corrosion based on the quantity and dimensions of corrosion pits. The main finding was that the average and maximum pit depth increased considerably with corrosion time. The increase in maximum depth from 2 to 3 months of pre-corrosion was more pronounced than the increase from 1 to 2 months. The average pit diameters remained similar for all conditions. However, the maximum pit diameter showed a considerable increase with corrosion time. The maximum pit depths were 39, 57, and 130 μm for 1, 2, and 3 months respectively.

Fatigue

From the S-N data Weber *et al.* found that fatigue life was reduced substantially from no corrosion to 2 days of corrosion, with very little further change to 24 days of corrosion. The reduction was higher for lower stress levels and longer fatigue lives. The variation in fatigue lives within each corrosion condition was small up to fatigue lives around 10^6. At longer fatigue lives than this the results were much more scattered.

The fatigue testing results found by Almaraz *et al.* also showed a substantial reduction in fatigue life for all pre-corroded specimens tested. The reduction was larger at lower stress levels and longer fatigue lives. At high stress levels the three pre-corrosion conditions all behaved similarly. For lower stress levels there was a considerable difference in fatigue life between the different corrosion conditions. However, the uncorroded specimen still performed much better. From an uncorroded fatigue life of around $5 \cdot 10^6$, the reduction in fatigue life was around 80%, 85%, and 90% for 2, 4, and 6 minutes for pre-corrosion respectively.

The fatigue results obtained by Abdulstaar *et al.* had two parts. Firstly, fatigue life was determined as a function of pre-corrosion time at one loading condition. These results showed a rapid reduction in fatigue life between 0 and 5 hours of pre-corrosion. The reduction in fatigue life was from around $2 \cdot 10^6$ to around $5 \cdot 10^5$ cycles. After 5 hours, the fatigue life decreased at a much slower rate. At 100 hours of pre-corrosion the fatigue life only decreased to around $4 \cdot 10^5$ cycles. The other part of the fatigue results was S-N data for different surface treatment conditions uncorroded and with 100 h of pre-corrosion. The ball burnished and shot peened specimens had substantially better fatigue performance that the electropolished specimens, and no considerable reduction in fatigue life in any part of the S-N curve was found after corrosion for these specimens. The electropolished specimens performed similarly with and without corrosion for the shortest fatigue lives tested, around 10^5 cycles. The difference in fatigue life between uncorroded and corroded specimens grew with lower stress levels and longer fatigue lives.

The S-N data found by Munoz *et al.* showed a substantial decrease in fatigue strength from uncorroded specimens to corroded specimens. The difference in fatigue life was not as large between each of the pre-corrosion levels. However, for the 3 months corroded specimen the S-N curve continued to a lower endurance limit than 1 and 2 months of pre-corrosion. For an uncorroded fatigue life of $3.5 \cdot 10^5$, pre-corrosion reduced the fatigue life by about 80% for 1 and 2 months, and about 85% for 3 months. The scatter in fatigue life results was lower for pre-corroded specimens compared with uncorroded specimens.

Further Analysis and Investigations

Weber *et al.* used the experimental S-N data to determine the Basquin law coefficients for the three conditions tested. Since the S-N curves obtained for the two corrosion levels were very similar, the study preceded to determine whether the difference was statistically significant. From statistical analysis the difference was deemed not to be statistically significant.

In addition to fatigue testing to obtain S-N data for each corrosion level, Almaraz *et al.* investigated the initiation and growth of fatigue cracks from corrosion pits in detail with numerical simulation and dedicated testing. Numerical simulation with finite element analysis (FEA) was done on the specimen geometry with a corrosion pit to find the theoretical stress intensity factor (SIF) with increasing crack depths. Experimental crack growth testing was done to find the threshold SIF range for crack propagation. The testing was done by interrupting fatigue loading to observe the crack length. The threshold SIF was determined by identifying the vertical asymptote in the crack growth rate diagram generated experimentally. The study found that the threshold SIF range was reduced with increasing corrosion. Finally, a K-T diagram was created from the experimental results.

Munoz *et al.* used the experimental S-N data to determine the Basquin law coefficient for each corrosion condition. Results of tests around run-out, at $2 \cdot 10^6$ cycles, were used to determine the endurance limit for each condition. A relation was established between the endurance limit as a fraction of yield strength and corrosion pit aspect ratio, meaning pit depth to diameter ratio.

Abdustaar *et al.* did not conduct any additional work or analysis related to fatigue behavior.

2.4.3. Comparison of Literature Results

The studies described vary greatly in alloys studied, procedure used for pre-corrosion, and method used for characterization of corrosion. As a result, direct comparison of corrosion damage does not provide much insight. The alloys, corrosion procedure, number of corrosion levels, corrosion characterization, and resulting corrosion damage according to the chosen characterization method are presented in Table 7. For the studies with multiple levels of corrosion, the corrosion damage included in the table represents the most severe condition. For the three studies presenting a quantification of corrosion damage, the damage varied between 7.7 µm to 130 µm. Since both alloy and corrosion conditions was different for these three studies, it is not possible to identify what caused this large difference.

Table 7: Comparison of pre-corrosion procedure and characterization in literature.

Study	Alloy	Corrosion procedure	Corrosion durations	Main corrosion characterization	Corrosion damage
Almaraz *et al.* [35]	6063-T5	Immersion in acid (pH 0.8)	2, 4, and 6 mins	Diameter and depth of crack initiating pit	Pit depths up to 110 µm
Abdulstaar *et al.* [36]	6082-T6	Immersion solution w/ NaCl	0 to 100 h	None	Not available
Weber *et al.* [37]	6061-T6	Immersion in solution w/ NaCl + acid (pH 2)	2 and 24 days	Depth of one pit for each corrosion level	Pit depths up to 7.7 µm
Muñoz *et al.* [38]	6082-T6	Salt spray chamber	1, 2, and 3 months	Density, depth, and diameter of pits in a sample area	Pit depths up to 130 µm

Table 8 summarizes the main tensile properties provided in the papers for their respective alloys. Only Abdulstaar *et al.* provides the precise chemical composition of the alloy tested. The others only provide the chemical composition range specified for 6082 in standards. As discussed in the theory section on intergranular corrosion in 6000-series aluminum, small differences in chemical composition can have a major influence on corrosion. The corrosion damage can therefore vary considerably even within the allowable range for each alloy designation.

Table 8: Comparison of mechanical properties of alloys studied in literature.

Study	Alloy	Yield strength, σ_y [MPa]	Ultimate tensile strength, σ_{UTS} [MPa]	Elongation at fracture, ε_f [%]
Almaraz *et al.* [35]	6063-T5	145	187	12
Abdulstaar *et al.* [36]	6082-T6	349	365	13.2
Weber *et al.* [37]	6061-T6	255	275	15
Muñoz *et al.* [38]	6082-T6	275	311	17

Table 9 compares the influence of pre-corrosion on fatigue behavior from literature in terms of reduction of fatigue limit. The reduction in fatigue limit at $2{\cdot}10^6$ found in literature ranged from 10.5% to 52.6%. The lowest reduction was found be Weber *et al.*, which had a low level of corrosion damage compared with the other studies at a maximum pit depth of 7.7 µm. The highest reduction was found by Munõz *et al.* which had the most severe corrosion damage of the studies, with a maximum pit depth of 130 µm.

Table 9: Comparison of reduction in fatigue limit with pre-corrosion in literature. The most severe level of pre-corrosion tested is presented.

Study	**Alloy**	**Fatigue limit[1], σ_e [MPa]**	**Normalized fatigue limit, σ_e/σ_y [%]**	**Corrosion depth[2] [µm]**	**Corroded fatigue limit[1], $\sigma_{e,corr}$ [MPa]**	**Fatigue limit reduction [%]**
Almaraz *et al.*[3] [35]	6063-T5	114	78.6	110	Not available	Not available
Abdulstaar *et al.* [36]	6082-T6	163	46.7	Not available	123	24.5
Weber *et al.* [37]	6061-T6	153	60.0	7.7	137	10.5
Muñoz *et al.*[4] [38]	6082-T6	108	39.3	130	46	57.4

[1]Fatigue limit here is a rough approximation taken as the alternating stress for a fatigue life of $2 \cdot 10^6$ cycles, based on the data available. The fatigue strengths provided in this table only serve to compare fatigue behavior between the four studies discussed.

[2]Taken as the maximum corrosion pit depth measured by whatever means the study used to measure pit depth.

[3]Did not test at stress levels low enough to find corroded fatigue limit at $2 \cdot 10^6$ cycles.

[4]Testing was conducted at $R = 0.1$, SWT correction was applied to find equivalent alternating stress at $R = -1$.

A comparison of fatigue life for the same normalized alternating stress to yield strength was considered. However, due to the large differences in alloys tested in each study, their fatigue behavior as a function of normalized alternating stress varied greatly. As noted in Table 9 the fatigue limit as a fraction of yield strength varied greatly. Almaraz *et al.* found the highest normalized fatigue limit at 78.6% of yield strength, while Munõz *et al.* found the lowest normalized fatigue limit of only 39.3% of yield strength. As a result, a comparison at the same normalized stress would mean fatigue lives in completely different areas of the S-N curve, meaning the reduction in fatigue life would not be comparable.

To ensure that the reduction in fatigue life was comparable between studies, the comparison was done in terms of fatigue life reduction at a loading giving the uncorroded specimens had a fatigue life of $5 \cdot 10^5$ cycles. This ensured that fatigue lives compared are in the same area of the S-N curves for the respective alloys. Therefore, the reductions in life with corrosion are as directly comparable as they could be. A fatigue life of $5 \cdot 10^5$ cycles was chosen for comparison as all studies covered tested stress levels giving this fatigue life. Table 10 shows the reduction in life with pre-corrosion from an uncorroded life of $5 \cdot 10^5$ cycles. The reduction in fatigue life was smallest, at 46.0%, in Weber *et al.*, which had the least severe corrosion damage. Alamarz *et al.* and Munõz *et al.* had comparable corrosion damage, with maximum pit depths of 110 µm and 130 µm, and similar reductions in fatigue lives, of 83.8% and 87.2% respectively. Abdulstaar *et al.* found a reduction in fatigue life of 62.0%.

Table 10: Comparison of reduction in fatigue life with pre-corrosion at stress level giving uncorroded fatigue life of $5 \cdot 10^5$ cycles. The most severe level of pre-corrosion tested is presented.

Study	Alloy	Alternating stress, σ_a [MPa]	Corrosion depth[1] [µm]	Corroded fatigue life, $N_{f,corr}$ [Cycles]	Fatigue life reduction [%]
Almaraz *et al.* [35]	6063-T5	129	110	81 000	83.8
Abdulstaar *et al.* [36]	6082-T6	179	Not available	190 000	62.0
Weber *et al.* [37]	6061-T6	176	7.7	270 000	46.0
Muñoz *et al.*[2] [38]	6082-T6	122	130	64 000	87.2

[1]Taken as the maximum corrosion pit depth measured by whatever means the study used to measure pit depth.
[2]Testing was conducted at $R = 0.1$, SWT correction was applied to find equivalent alternating stress at $R = -1$.

2.4.4. Discussion of Literature

Due to the large variation in alloys and corrosion damage, direct comparison between the existing literature on pre-corroded fatigue of 6000-series aluminum alloys is difficult. However, some important points on the relationship between corrosion damage and fatigue behavior can still be drawn from them:

- All studies found that the introduction of pre-corrosion had a substantial impact on fatigue behavior. This is likely due to corrosion damage acting as notches, facilitating crack initiation.
- All studies found a rapid reduction in fatigue resistance with initial corrosion and less additional reduction with further corrosion. In other words, the difference in fatigue behavior is generally more substantial between uncorroded and corroded specimens, than between different levels of corrosion. This is likely due to corrosion drastically reducing the crack initiation life so that most of the corroded fatigue life is crack propagation, which is not as influenced by different levels of corrosion damage.
- All studies found that the influence of pre-corrosion increases with lower applied stresses and longer fatigue lives. This is likely due to crack initiation, which is what corrosion damage mainly affects, being larger proportion of the fatigue life at lower stress levels and longer fatigue lives.
- Studies with combinations of alloy and corrosion procedures resulting in more severe corrosion damage found larger reductions in fatigue limit and in fatigue life than those with less corrosion damage.

Weaknesses in the existing literature are lack of information about the precise chemical composition of the alloys tested and poor characterization and quantification of corrosion damage. Chemical composition, even within the specification for an alloy designation, can have a major effect on corrosion. Not providing this data makes it difficult to compare the effects of the different pre-corrosion procedures used. Only Abdulstaar *et al.* provided the precise

chemical composition of the tested alloy. Even more significant is the limited characterization of corrosion damage. Munõz *et al.* was the only paper providing detailed data on the amount of and dimension of corrosion pits. Weber *et al.*, and Almaraz *et al.* provided very limited data, and Abdulstaar provided no data on corrosion damage.

The existing literature on fatigue behavior in pre-corroded 6000-series aluminum is limited to looking at alloys experiencing pitting corrosion. However, due to the impurity content of the simulated recycled alloy, intergranular corrosion is the main corrosion form with this alloy. The nature of intergranular corrosion's influence on fatigue could differ from that of pitting corrosion. There is currently no existing literature on the influence of intergranular corrosion on the fatigue behavior of 6000-series aluminum alloys.

2.5. Corrosion Testing in AluGreen

Testing of corrosion resistance and tensile properties with pre-corrosion was conducted for simulated recycled 6082 as part earlier investigations in AluGreen. The investigations were done by SINTEF Raufoss, and the results are currently unpublished. Testing was done on three variants of 6082 with different levels of impurities, referred to as GA1, GA2, and GA3. The impurities varied between each alloy variant are Fe, Cu, and Zn. The chemical composition of each alloy variant is presented in Table 11.

Table 11: Chemical composition of AluGreen 6082 alloy variants compared with 6082 specification [8, 9]. Data for AluGreen alloy variations was supplied by SINTEF from AluGreen.

Alloying element	**6082 [wt.%]**	**GA1 [wt.%]**	**GA2 [wt.%]**	**GA3 [wt.%]**
Cr	<0.25	-	-	-
Cu	<0.1	0.02	0.05	0.10
Fe	<0.5	0.22	0.28	0.32
Mg	0.6 - 1.2	0.65	0.65	0.65
Mn	0.4 -1.0	0.55	0.55	0.55
Si	0.7 - 1.3	0.90	0.90	0.90
Ti	<0.1	0.01	0.01	0.01
Zn	<0.2	0.02	0.10	0.20
Al	Balance	Balance	Balance	Balance

Corrosion testing was performed according to ISO11846 [39]. The corrosion procedure used was method B in the standard, where corrosion is done by immersion of specimens in a solution of 30g/l of sodium chloride (NaCl) and 10 ml/l of hydrochloric acid (HCl) in distilled water for 24 h. This standard is aimed at determining the resistance to intergranular corrosion for heat-treatable aluminum alloys. This method was used as intergranular corrosion was expected to be the corrosion form, due to the impurity content. Examination of the cross sections after corrosion confirmed that the corrosion form was intergranular corrosion. The corrosion damage was quantified by measuring the depth of intergranular corrosion on cross sections of the

specimens. The corrosion damage for each alloy variant is shown in Figure 5, and the average and maximum depth is presented in Table 12.

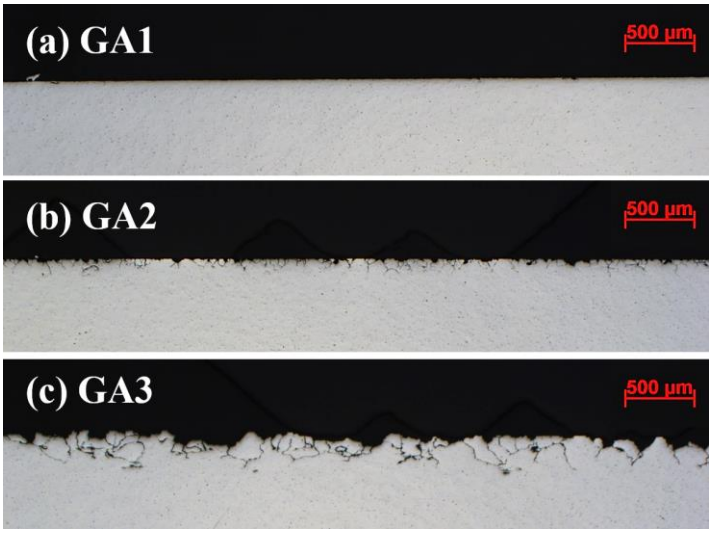

Figure 5: Corrosion damage on AluGreen alloy variants. Supplied by SINTEF Raufoss from AluGreen.

Table 12: Average and maximum corrosion depth for AluGreen alloy variants. Supplied by SINTEF Raufoss from AluGreen.

Alloy variant	**Average corrosion depth [µm]**	**Maximum corrosion depth [µm]**
GA1	45.9±12.0	52.7
GA2	64.9±15.3	176.5
GA3	197.0±46.4	435.3

Tensile testing was done for each alloy variant with and without pre-corrosion. Tensile testing results are presented in Table 13. For uncorroded specimens, the yield and ultimate tensile strength increased slightly with increased impurity content. With corrosion, the ultimate tensile strength is reduced with increasing levels of impurities. This reflects the increasing severity of the corrosion damage with increasing impurity levels. To account for the reduction in cross section area resulting from corrosion, an adjusted cross section area was calculated based on the average corrosion depth. The ultimate tensile strength calculated with this cross section area was similar for all three alloy variants, at approximately the same level as the uncorroded specimens.

Table 13: Tensile strength with and without corrosion for each alloy variant. Supplied by SINTEF Raufoss from AluGreen.

Alloy variant	**Yield strength, σ_y [MPa]**	**Uncorroded tensile strength, σ_{UTS} [MPa]**	**Corroded tensile strength, $\sigma_{UTS,corr}$ [MPa]**	**Corrected corroded tensile strength [MPa]**
GA1	299	322	322	328
GA2	304	326	302	316
GA3	311	334	270	328

3. Method

To assess the influence of pre-corrosion on the fatigue behavior of recycled aluminum, fatigue testing was done for specimens with different levels of pre-corrosion and compared with uncorroded specimens. The alloy tested was a 6082 aluminum alloy with high levels of impurities, representing the chemical composition of a recycled alloy. Specimens were tested with the surface condition resulting from extrusion, referred to as “as extruded”, and surface treated with glass bead blasted, referred to as “glass bead blasted” and abbreviated GBB. The glass bead blasted surface condition was tested to investigate this as a method for improving pre-corroded fatigue behavior by influencing fatigue and/or corrosion behavior. Fatigue testing was done with at the same loading conditions for all specimens. Fatigue behavior was therefore quantified as fatigue life at the prescribed loading condition.

In addition to fatigue testing, various other tests and measurements were done to characterize the effects of pre-corrosion and glass bead blasting on the specimens and explain the influence on fatigue behavior. The tests and measurements done are presented in Table 14. Microstructure, hardness, corrosion characterization, and surface topography were assessed on dedicated specimens that were not subjected to fatigue testing. The complete test matrix showing all specimens and which tests and measurements they were used for is provided in Appendix A.

Table 14: Tests and measurements.

Test/Measurement	**Objective**	**Conditions tested**
Microstructure examination	Observe grain structure, and possible changes with GBB or corrosion.	As extruded, as extruded + 24 h corr., and GBB
Hardness measurement	Determine if GBB has caused compressive residual stresses.	As extruded and GBB
Corrosion depth measurement	Determine form, distribution, and depth of corrosion for each corrosion duration.	All conditions (1 per)
Surface topography	Determine roughness values and shape of surface profile.	All conditions (1 per)
Surface topography, post-fatigue	Determine if fatigue loading causes changes in surface topography.	As extruded, as extruded + 24 h corr., GBB, and GBB + 24 h corr.
Fatigue testing	Determine fatigue lives at set loading conditions.	All conditions (3 per)
Fracture surface examination (SEM)	Characterize failure mechanisms and crack initiation.	All conditions (1 per, all 3 for defect area)
Surface features (SEM)	Examine microscopic surface features.	As extruded + 24 h corr., GBB, and GBB + 24 h corr.
Striation measurement (SEM)	Determine crack growth at different crack lengths for Paris law coefficients.	As extruded and GBB
Defect area measurement (SEM)	Determine size of defect area responsible for crack initiation.	All conditions (3 per)

The following sections provide details on the material and preparation with glass bead blasting and pre-corrosion, and the objective, procedure, and process parameters involved in each form of testing.

3.1. Material and Preparation

This section provides details on the recycled 6082 aluminum alloy studied, along with the procedures used for preparation of the specimens by glass bead blasting and pre-corrosion. Section 3.1.1. on the material is a reworked version of the equivalent section written for the specialization project report.

3.1.1. Material

Several aluminum alloys and variants are used as part of the AluGreen project. The alloys being examined in fatigue testing are three variants of 6082, referred to as GA1, GA2 and GA3. The differences between these variants are the concentration of the undesirable impurity elements Fe, Cu and Zn. The investigation on the influence of prior corrosion on fatigue behavior was done on the GA3 variant of 6082. Previous testing in the AluGreen project found that GA3 variant was the most susceptible to corrosion damage of the three variants. Therefore, GA3 was likely to see the largest reduction in fatigue life due to corrosion. The chemical composition of GA3 is shown together with the specification for 6082 in Table 15. Note that the GA3 composition meets the specification for chemical composition for 6082 and is therefore an acceptable composition for use according to the standard.

Table 15: Chemical composition of 6082-GA3 compared with 6082 specification [8, 9]. Data for GA3 alloy was supplied by SINTEF from AluGreen.

Alloying element	**Content GA3 [wt.%]**	**Content 6082 [wt.%]**
Cr	-	<0.25
Cu	0.10	<0.10
Fe	0.32	<0.50
Mg	0.65	0.60 - 1.20
Mn	0.55	0.40 -1.00
Si	0.90	0.70 - 1.30
Ti	0.01	<0.10
Zn	0.02	<0.20
Al	Balance	Balance

The test specimens were made from a solid shaped extruded profile with a thickness of 6 mm. The manufacturing process of the profile consisted of casting, homogenizing, extrusion, stretching, and aging. Billets of 203 mm diameter were cast with gas cushioning casting. These were then homogenized at 580°C for 2 hours and 15 minutes. The extrusion was done in 14 passes with the material preheated to 480°C, at a speed of 11.8 m/min. Water spray cooling was used during the extrusion process. After extrusion the material was stretched to 1% elongation. After this it was stored for between 2 and 5 hours before artificial aging done by holding the temperature at 175°C for 5.5 hours after a 1 h heating time. This manufacturing process gave

the material T6 temper. For the investigation of pre-corroded fatigue, specimens were cut with their length direction transverse to the extrusion direction of the profile.

The profile had a grain structure characterized by two regions. Figure 6 shows an image of the grain structure of the cross section of the profile from AluGreen. The bulk material had a fine elongated grain structure, which is a result of the extrusion process. At the surface of the extruded profile there was a layer of large, recrystallized grains. This is not typical for most extruded aluminum alloy profiles but can occur with certain 6000-series alloys. The formation of a recrystallized layer occurs during homogenization for grains that have experiences high plastic deformation during extrusion. The formation of a recrystallized layer depends on factors such as alloy composition and extrusion process parameters [40]. The average grain size in the middle of the cross section was 25.8 μm^2, while the average grain size in the recrystallized layer was 250.1 μm^2. As the microstructure close to the surface is an important factor in determining both corrosion and fatigue behavior, the presence of a recrystallized layer could greatly influence the materials behavior in pre-corroded fatigue.

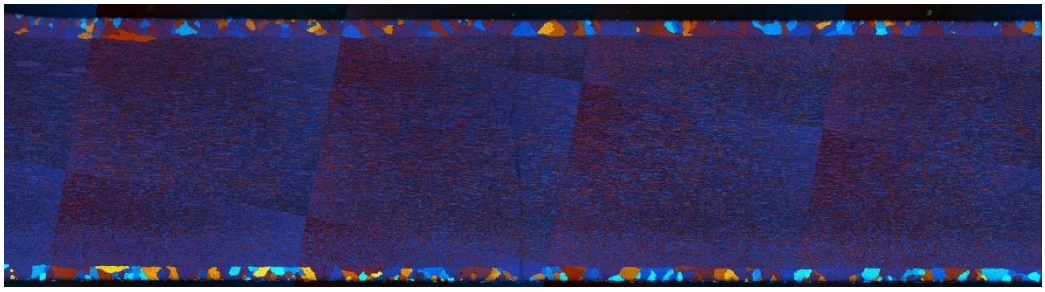

Figure 6: Grain structure of extruded profile. Supplied by SINTEF Raufoss from work done as part of AluGreen.

Tensile properties of the alloy were found as part of the basic characterization of the alloy variants done previously in AluGreen. Results of tensile testing done on the GA3 variant of 6082-T6 perpendicular to the extrusion direction are presented in Table 16.

Table 16: Tensile properties of 6082-GA3. Supplied by SINTEF from AluGreen.

Property	**Value**
Yield strength, σ_y [MPa]	327
Ultimate tensile strength, σ_{UTS} [MPa]	350
Elongation at fracture, ε_f [%]	11.0

3.1.2. Glass Bead Blasting

Some specimens were subjected to glass bead blasting before being tested with and without pre-corrosion. This was done to investigate how changes in the surface of the material would affect corrosion and/or fatigue behavior. Glass bead blasting has the potential to change the surface of the material in several ways. It can change the surface topography, introduce compressive residual stresses, and affect the microstructure. Changes to one or more of these factors could affect corrosion and/or fatigue behavior. Due to various ways glass bead blasting could impact the material, it is not possible to predict which of the potential changes would be

dominant in influencing the corrosion and fatigue behavior. Both positive and negative impact on corrosion and/or fatigue behavior were therefore possible outcomes.

Glass bead blasting was done by hand in a sand blasting cabinet. Figure 7 shows the sand blasting cabinet used. The glass beads used had a size of 150-200 µm. The air pressure was approximately 300 kPa. Glass bead blasting of aluminum with these conditions should not remove any material from the surface. This was confirmed by weighing one specimen before and after glass bead blasting. Weighing showed a negligible weight loss of under 5 µg for a sample initially weighing 19.480 g. The glass bead blasting step was done before pre-corrosion and machining to fatigue specimen dimensions. The material at this stage was blocks of dimensions 77×16×6 mm.

Figure 7: Sand blasting cabinet.

3.1.3. Pre-Corrosion

To conduct fatigue testing of the alloy with different levels of pre-corrosion, an accelerated method of introducing corrosion damage was used. Pre-corrosion in a natural environment would provide the most accurate representation of corrosion damage seen in likely applications of the material. However, as it is impractical to wait months or years for pre-corrosion, a procedure for accelerated corrosion was used. The procedure chosen for pre-corrosion of the specimens was immersion in a solution of sodium chloride (NaCl) and hydrochloric acid (HCl) in distilled water according to method B in ISO11846 [39]. The purpose of the procedure described in this standard is to determine the resistance to intergranular corrosion in heat treatable aluminum alloys. Intergranular corrosion due to impurity content was known from prior corrosion testing in AluGreen, described in section 2.5., to be the corrosion form experienced by the recycled alloy.

Several corrosion durations were selected to study the influence of different levels of corrosion damage on fatigue behavior. The corrosion test duration in method B of ISO11846 is 24 h. Prior corrosion testing in AluGreen found that this resulted in severe intergranular corrosion. Pre-corrosion durations of 12 and 24 h were selected for as extruded and glass bead blasted to assess

the influence of two levels of severe corrosion damage. In addition, pre-corrosion durations of 1 and 4 h were tested for the as extruded surface condition to identify the influence of less severe corrosion damage, and possibly find the transition where the corrosion damage becomes severe enough to impact fatigue.

The material was pre-corroded as individual blocks cut from the extruded profile. The specimens were cut from the profile using with a saw, creating a rough surface on the cut faces. These faces were therefore machined with face milling to provide a finer surface finish. The surfaces of the original extruded surface were kept for as extruded specimens. For glass bead blasted specimens glass bead blasting was done on the blocks before pre-corrosion. The surface conditions of the blocks prior to corrosion are shown in Figure 8. The blocks had dimensions 77×16×6 mm.

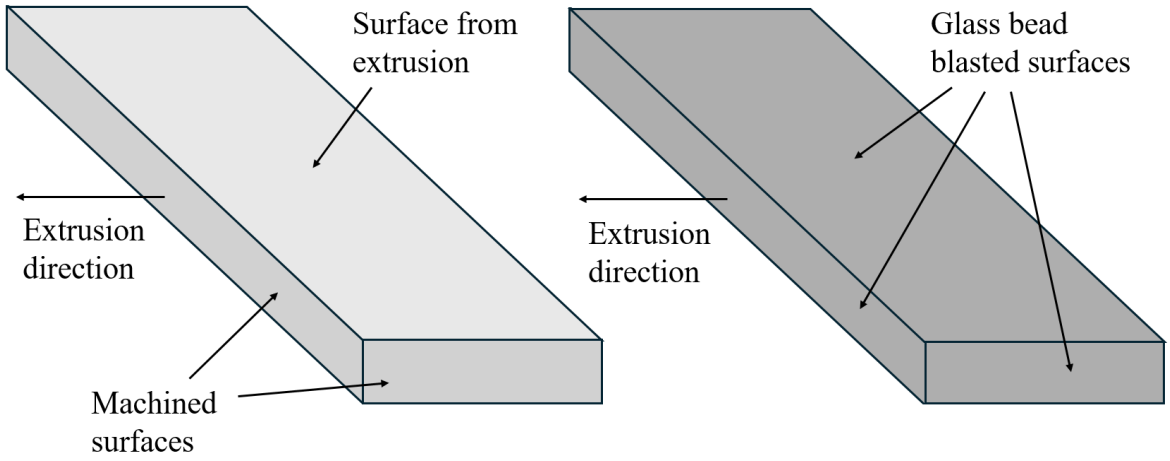

Figure 8: Condition of as extruded (left) and glass bead blasted (right) blocks before pre-corrosion.

The corrosion procedure in ISO11846 starts with specimen surface preparation. The surface preparation was meant to remove any contamination that could impact the corrosion behavior. The first step was degreasing in acetone in an ultrasonic cleaner. This removes any oils or cutting fluids that might be present on the surface from storage or machining. The next step was etching in a sodium hydroxide (NaOH) solution heated to 55°C for 3 minutes, as shown in Figure 9. This removes particle contamination not removed by the acetone. The specimens were individually immersed in a beaker containing the solution on a heating element. The temperature was regulated by a power switch controlled by a temperature probe in the solution. A magnetic stirrer stirred the solution continuously throughout the etching. After etching, the specimens were rinsed in running water before being immersed in concentrated nitric acid (HNO_3) for 2 minutes. This removes corrosion products left by the etching. Finally, each specimen was rinsed in running water then distilled water and dried.

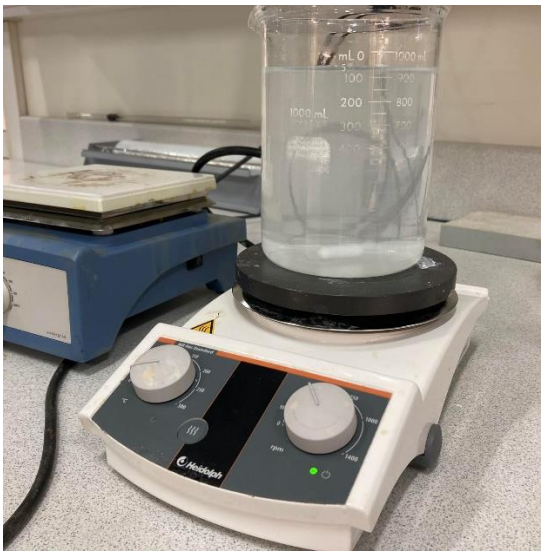

Figure 9: NaOH on heating element as part of preparation of specimens.

The pre-corrosion process was conducted with each individual specimen immersed in the electrolyte solution in individual beakers for the prescribed durations of time. The corrosion solution was prepared in volumetric flasks to get a precise mixture. First, some distilled water was added for the other contents to dissolve into. 30 g/l of sodium chloride (NaCl) was weighed on a precision scale and added to the flask, then 10 ml/l of hydrochloric acid (HCl) was added. Finally, the volumetric flask was filled with the remaining distilled water and turned several times to mix all the contents. The pH was measured for every batch of electrolyte mixed. The pH was measured to be between 0.92 and 0.98 for all the flasks mixed.

The corrosion solution was added to individual beakers, 650 to 700 ml per beaker. The prepared specimens were then immersed in the solution. The specimens were placed diagonally, resting on the bottom and on the side of the beaker, ensuring all surfaces were exposed to the solution and no enclosed areas of electrolyte were formed between the specimen and beaker. The specimens were placed such that the level of solution in the beaker was more than 20 mm above the top of the specimen, as specified in ISO11846. This is shown in Figure 10. Once the exposure duration was done, the specimens were removed from their beakers, rinsed in running water, then distilled water, before being dried and placed in individual plastic bags.

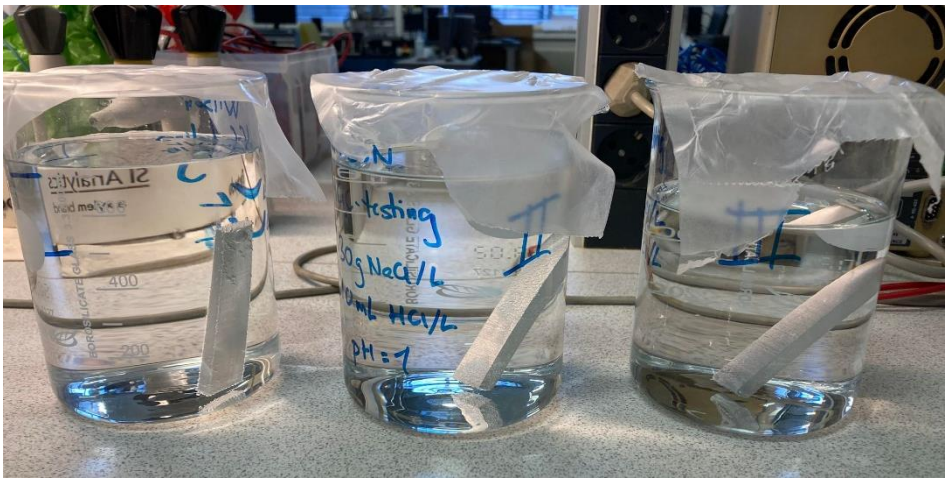

Figure 10: Specimens immersed in corrosion solution.

3.2. Testing

This section describes the objective and explanation of each test method applied. Details are also provided on the equipment, procedure, and relevant testing parameters. The main testing form was fatigue testing. However, various supplementary tests were done to be able to explain the influence of pre-corrosion and glass bead blasting on the fatigue behavior.

3.2.1. Microstructure

Microstructure plays an important role in determining mechanical properties. As mentioned, the extruded profile studied in this thesis had a recrystallized layer close to the surface with large equiaxed grains compared to the small, elongated grains found in the center of the profile. The recrystallized layer has a considerable influence on corrosion and fatigue behavior, which are both greatly affected by the microstructure close to the surface. As the grain structure of the baseline condition already has been studied as part of the AluGreen project, the examination done in this thesis had two primary objectives, to determine whether the glass bead blasting had any effect on the grain structure close to the surface and to identify correlations between the features of the grain structure and corrosion morphology. Based on these objectives, the conditions examined were the as extruded condition with no corrosion, the glass bead blasted specimen with no corrosion, and as extruded with 24 h pre-corrosion.

Several methods can be used for examining the grain structure of aluminum alloys. In this case, the grain structure was observed with polarized light microscopy of a polished cross section surface anodized with Barker's reagent. Polarized light microscopy uses a polarization filter after the light source that only allows light waves with a single wave orientation to pass through [41]. After the light is reflected from the sample surface, the light passes through another polarization filter, referred to as the analyzer filter [41]. This analyzer filter only allows light with a wave orientation perpendicular to the wave orientation of the polarization filter to pass through. In anodization of aluminum, electrolysis is used to form a thick oxide layer on the surface. When aluminum is anodized with Barker's reagent, an anisotropic oxide layer is formed on the surface. This layer reflects light differently depending on the orientation of the atomic structure of the grain underneath [41]. This results in different light intensity for each

grain after the analyzer filter, corresponding to the grain's crystal orientation. A color filter is then used to give different colors to the different light intensities from the analyzer filter [41]. The resulting image shows the grains with different colors, allowing the grain structure to be examined.

Samples were prepared for anodization and grain structure examination by grinding and polishing cross section surfaces of small samples molded in epoxy. Samples of the material were cut with a Struers Labotom-5 precision cutting machine, shown in Figure 11 (a). To see the grains on the anodized surface, the surface must be polished smooth before anodizing. To hold the cross section flat on the grinding machine and avoid grinding the specimen at an angle, the samples were mounted into larger blocks that could more easily be ground flat.

In metallographic examination different methods are used for mounting of samples. Mounting is usually done in polymer resins [42]. The two main categories of procedures are hot mounting and cold mounting. In hot mounting a hot mounting press is used to heat and compress polymer powder around the specimen [42]. This causes the polymer powder to bind together and form a cohesive material around the specimen. This process usually quick, only taking few minutes. In cold mounting, a polymer resin, usually in the form of two components liquid mixture, is poured into a mold with the specimen [42]. The polymerization process is responsible for curing the resin. This can take from a few minutes to many hours depending on the polymer. For the aluminum alloy investigated in this thesis, the age hardening temperature of the alloy was close to the hot mounting temperature. There was a possibility that the temperature could affect the microstructure of the material. Therefore, cold mounting was selected. The cold mounting was done by molding the specimens in a two-component epoxy resin in paper molds. Once the epoxy cured, after 24 to 48 h, the epoxy block with the sample was removed from the paper mold for grinding and polishing.

Grinding and polishing was done with a Stuers grinding/polishing machine, shown in Figure 11 (b). Due to the concave shape of the bottom of the molded blocks, the first step used coarse grinding paper to grind the block flat so that the aluminum sample aligned with the bottom surface of the block. After this several steps of grinding with increasingly fine grinding paper were used. The final steps were polishing with 3 µm and 1 µm diamond polishing spray and blue lubricant, and finally polishing with OP-U. OP-U polishing uses a suspension with fine silicon dioxide (SiO_2) particles with a grain size of 0.04 µm [43]. All grinding and polishing steps are summarized in Table 17. After polishing the samples were cleaned in an ultrasonic cleaner with ethanol.

Table 17: Grinding and polishing steps for anodization.

Step	Grinding/Polishing
1	P120 or P220
2	P500
3	P1000
4	P2000
5	P4000
6	3 µm diamond polishing spray
7	1 µm diamond polishing spray
8	OP-U polishing

Figure 11: Struers Labotom-5 precision cutting machine (a) and Struers LaboPol-30 grinding/polishing machine (b).

The anodization process requires an electric connection to the sample. This was made possible by drilling a hole through the epoxy into the back side of the aluminum sample. Anodizing was done with a Struers LectroPol-5 electrolytic polishing machine, shown in Figure 12 (a) and (b). The electrolyte used was Barker's reagent (2% HBF4) and the applied voltage was 20 V. Barker's reagent is a commonly used electrolyte for anodization of aluminum to reveal the grain structure. After anodizing the samples, images of the surfaces were captured with an optical microscope with polarized light. The microscope used was a Leica DMI5000 M inverted microscope.

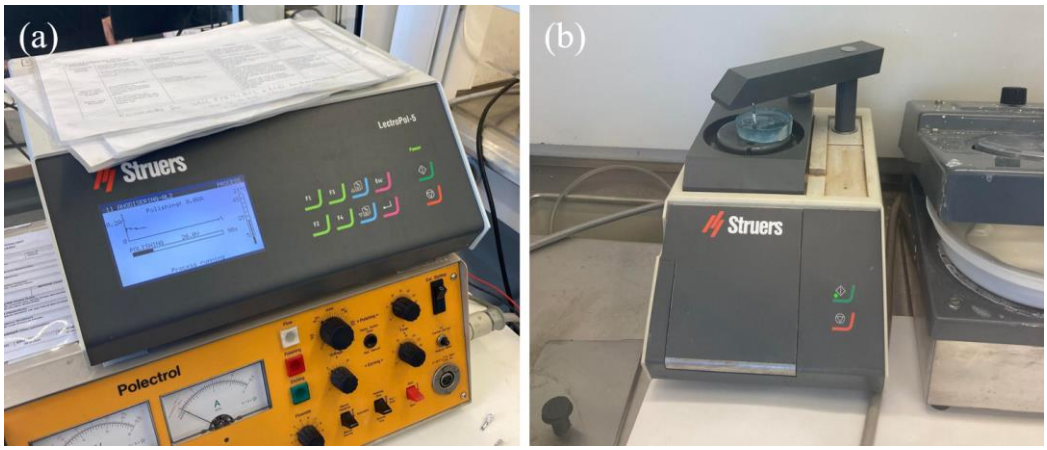

Figure 12: Struers LecroPol-5 electrolytic polishing machine control unit (a) and polishing unit (b).

3.2.2. Hardness

Microhardness was measured for the uncorroded material and the uncorroded glass bead blasted material. This was done to investigate whether glass bead blasting had the desired effect of introducing compressive residual stresses in the surface of the material. The hardness measurements could also provide an indication as to how deep the effect was for the glass bead blasting conditions used.

Hardness is a measure of a material's resistance to indentation [44]. It often correlates with tensile strength. However, hardness only provides an indication of local material properties close to the surface and does not necessarily reflect the bulk material mechanical properties. The hardness measurement method used was Vickers microhardness. The principle of Vickers hardness measurement is that the surface in indented by a pyramid shaped diamond tip with a prescribed force [44]. The dimensions of the indentation mark are then measured through an optical microscope. The resulting Vickers hardness, HV, is determined from the indentation force and area of the indentation mark. Equation 8 shows Vickers hardness (HV) as a function of F, the applied force in kgf, and d, the mean value of diagonals of indentation mark in mm [44].

$$\mathrm{HV} = 1.8544\frac{F}{d^2} \tag{8}$$

To find the microhardness as a function of depth from the surface for the as extruded and glass bead blasted material, specimens were cut to expose their cross section and then ground to a smooth surface finish. Microhardness measurements were done at several depths along three paths going from the surface towards the center of the material. As glass bead blasting was expected to have a considerable impact only close to the surface, measurements were closely spaced at small depths and wider spaced at higher depths. The microhardness testing machine used was a Mitutoyo HM-221, as shown in Figure 13.

Figure 13: Mitutoyo HM-221 Microhardness testing machine.

Hardness was measured with an indentation force of 0.1 kgf (0.9807 N). The depths selected were 0.1, 0.2, 0.3, 0.4, 0.5, 1, and 1.5 mm. Measurements were made along three lines from the surface into the material, as shown in Figure 14. The average of the three values was taken as the hardness at each depth.

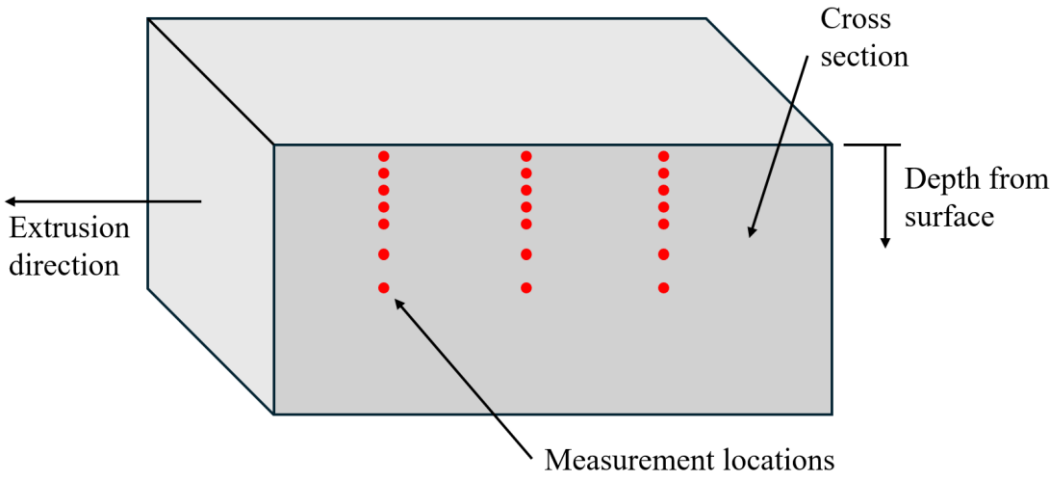

Figure 14: Hardness measurement locations.

3.2.3. Corrosion Depth

To assess the influence of different levels of corrosion damage on fatigue behavior, the extent of corrosion damage was characterized in terms of corrosion depth. From corrosion testing previously conducted as part of the AluGreen project, intergranular corrosion was known to be the dominant form of corrosion with the recycled alloy. Therefore, it was assumed that the main mechanism through which the corrosion damage influenced the fatigue life was through crack initiation from the preexisting intergranular cracks created by intergranular corrosion. For corrosion pitting, the influence on crack initiation can be related to several factors such as depth, diameter, and shape [38, 45]. However, as intergranular corrosion causes sharp cracks following

the grain boundaries into the material, the defects can be assumed to be sharp, without any shape or radius. The intergranular corrosion depth from the surface was therefore selected as the primary quantification of corrosion damage. Due to the nature of fatigue crack initiation, a fatigue specimens fatigue life will generally be determined by the most severe defect. Therefore, quantifying the corrosion based on the most severely corroded locations was of primary interest with regards to fatigue. The maximum observed intergranular corrosion depth was taken as the characteristic value for each condition.

The depth of intergranular corrosion was determined from observation of the cross section under optical microscope. Finding the true maximum depth would require observation of every possible cross section of all specimens. As this is not practically possible, a limited selection of cross sections was made for examination. Cutting the specimens to examine their cross section was also not possible for the specimens for use in fatigue testing. Therefore, one dedicated specimen was prepared for each condition for corrosion characterization. As the extent of corrosion damage varied across the surfaces, the two areas of most severe corrosion for each specimen were selected for cross section examination as shown in Figure 15. This is the corrosion depth measurement procedure described in ISO11846 [39].

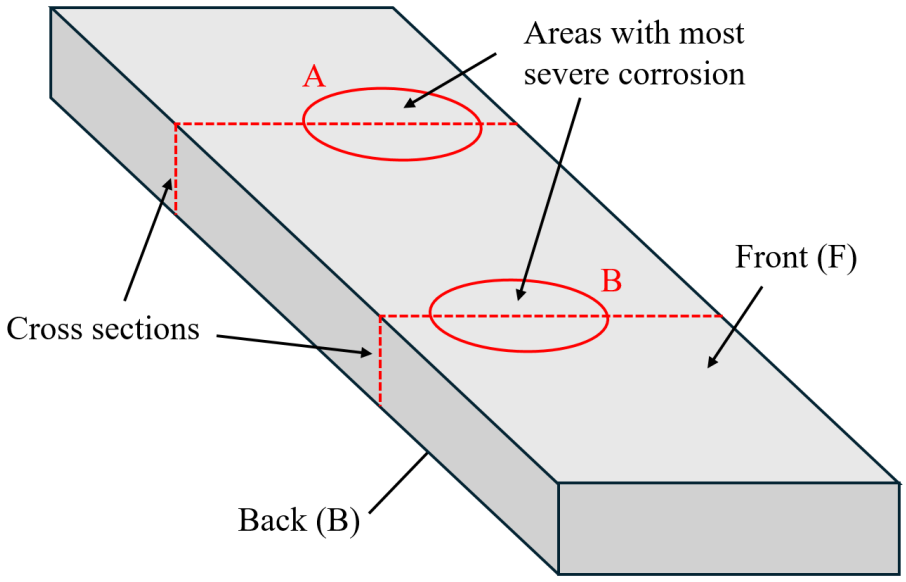

Figure 15: Measurement areas for corrosion depth.

The first step in measuring intergranular corrosion depth was selecting the areas of most severe corrosion damage. This was done by visually examining the entire surfaces front and back of the specimen under optical microscope at 5x magnification. The two areas which appeared to have suffered the most severe corrosion attacks were circled with a marker. The specimens were then cut in these areas with a Stuers precision cutting machine, Figure 11 (a), to reveal the cross sections. To be able to see the intergranular corrosion cracks under optical microscope the cross section surface was ground and polished. To be able to hold the cross section flat on the grinding machine the samples were molded into bigger blocks. The molding procedure was identical to the procedure described in section 3.2.1.

The grinding and polishing were done with a Stuers grinding/polishing machine, as shown in Figure 11 (b). The grinding and polishing procedure was identical to what was used for microstructure examination, the only difference being that OP-U polishing was not done in preparation for corrosion depth measurement. All grinding and polishing steps are summarized in Table 18.

Table 18: Steps in grinding and polishing for corrosion depth measurement.

Step	Grinding/Polishing
1	P120 or P220
2	P500
3	P1000
4	P2000
5	P4000
6	3 µm diamond polishing spray
7	1 µm diamond polishing spray

After polishing, the cross sections were observed under optical microscope. The microscope used was an Olympus BX53M, as shown in Figure 16. The front and back sides of the cross sections were carefully examined for corrosion attacks. This means a total of four areas of the surfaces were examined per condition, two cross sections with two sides each. Areas of deep intergranular corrosion were imaged and measured. The measurements were taken from the surface perpendicularly into the material to the deepest point of visible corrosion damage. The three largest depths of intergranular corrosion were recorded for each of the four areas examined.

Figure 16: Olympus BX53M optical microscope.

3.2.4. Surface Topography

Surface topography can be a determining factor in fatigue behavior through its role in crack initiation. Fatigue life in the high cycle regime is primarily determined by the crack initiation phase, with cracks usually initiating from defects or irregularities in the surface. As explained in section 2.3.4., both the shape and size of the features of surface topography can greatly influence the fatigue life. Examining the influence of corrosion and glass bead blasting on the surface topography can therefore provide useful insight into the influence on fatigue behavior. The surface topography was examined for as extruded and glass bead blasted surfaces uncorroded and with all levels of corrosions. In addition, the surface topography was examined for the machined side surface of one fatigue specimen. Details on the fatigue specimens are provided in section 3.2.5.

The most used values for quantifying surface roughness are *Ra*, *Rq*, *Rt*, and *Rz* [46]. These values are calculated from the surface height values along a surface profile. *Ra* is the average height difference from the mean height of the profile [46]. *Rq* is the root mean squared height difference from the mean height [46]. While *Ra* and *Rq* represent the average deviation from the mean height, *Rt* and *Rz* are representations of the maximum variations. *Rt* is the average of five maximum peak-to-valley heights in adjoining sample lengths [46]. *Rz* is the average deviation from the mean height of the five tallest peaks and five lowest valleys within the sampling length [46]. In addition to the profile roughness values, equivalent values can be calculated over an area. These are then referred to as *Sa*, *Sq*, and *Sz*, respectively. In calculating surface roughness values, long waves and curvature of the surface profile is not considered part of surface roughness and are removed. The cutoff wavelength, λ_C, is applied in calculation to separate what is considered waves and roughness.

To examine the surface topography of each condition tested, sample areas were 3D-mapped with a confocal microscope. The confocal microscope was a Alicona InfiniteFocus G4, shown in Figure 17. One specimen per condition was mapped. The form removal function in the microscope analysis software was used to remove the influence of any potential misalignment between the surface and lens. A profile length on the form removed surfaces was used for calculating the profile surface roughness values. The area surface roughness values were calculated from the entire mapped area. All specimens were mapped with identical microscope settings for consistency. The settings chosen were based on the recommendations in the manual for the confocal microscope. The 20x magnification lens was used for mapping with a vertical resolution of 100 nm. The profile length for calculating surface roughness values was 3 mm. The mapping and profile direction was in the loading direction, perpendicular to the extrusion direction.

Figure 17: Alicona InfiniteFocus G4 confocal microscope.

The influence of surface topography on fatigue behavior cannot be correlated directly to the surface roughness values. This is because the roughness only captured the size of surface roughness without representing shape and local variation. Therefore, other approaches were also used to characterize the surface topography in addition to measuring the surface roughness. The 3D surface maps were examined to identify regular patterns and local irregularities of the surface topography and determine the shape and sharpness of these features. Surface profiles representing characteristic features were compared directly for some selected conditions.

The surface topography was also examined for selected conditions after fatigue testing. The conditions looked at were as extruded and glass bead blasted with and without 24 h corrosion. The area directly next to crack initiation was 3D-mapped in the same direction as before fatigue loading. The surface roughness values were calculated and compared with the values before fatigue. The area mapped is shown in Figure 18.

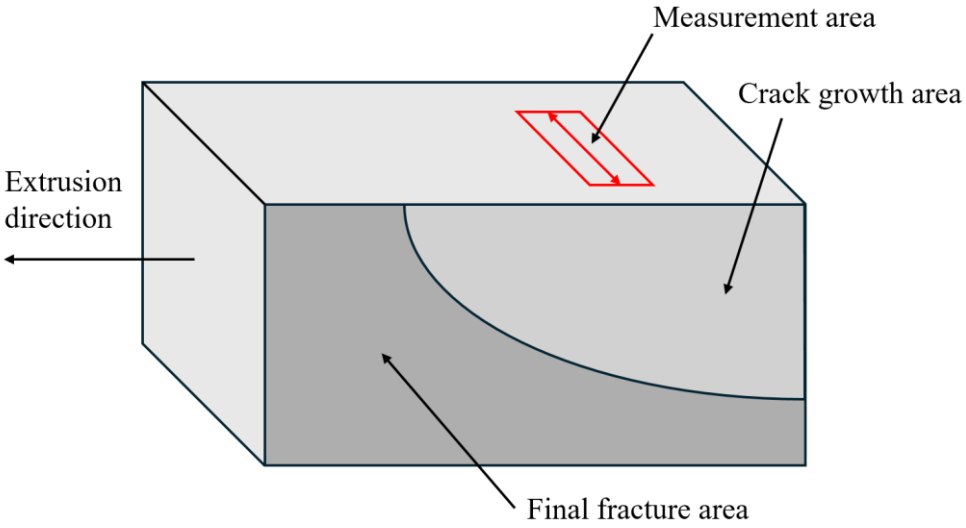

Figure 18: Measurement area for post-fatigue surface topography.

3.2.5. Fatigue Testing

To determine the influence of pre-corrosion and glass bead blasting on fatigue behavior, three specimens of each condition were fatigue tested. Fatigue testing was done with axial loading with the same loading conditions for all specimens. As the objective of this study was to investigate fatigue behavior in terms of fatigue life in high cycle fatigue, a loading level giving all conditions fatigue lives in the finite life HCF regime was selected. The stress level used was a maximum cyclic stress σ_{max} = 180 MPa. The stress ratio was R = 0.1. With the specimen cross section being 6×10 mm, the maximum load was $F_{\max}$ = 10.8 kN and a minimum load was $F_{\min}$ = 1.08 kN. Due to availability, two different fatigue testing machines were used in fatigue testing. Testing of uncorroded as extruded specimens was done with the StepLab – Multiaxial 20 kN machine shown in Figure 19 (a). Results for uncorroded as extruded specimens were obtained as part of the specialization project. Testing of all other conditions was done with the MTS 809 Axial/Torsional Test System shown in Figure 19 (b). Due to the characteristics of the machines, the loading frequences used were 25 Hz for the StepLab machine and 10 Hz for the MTS machine. Changes in loading frequency at this magnitude does not influence the fatigue behavior of aluminum in air.

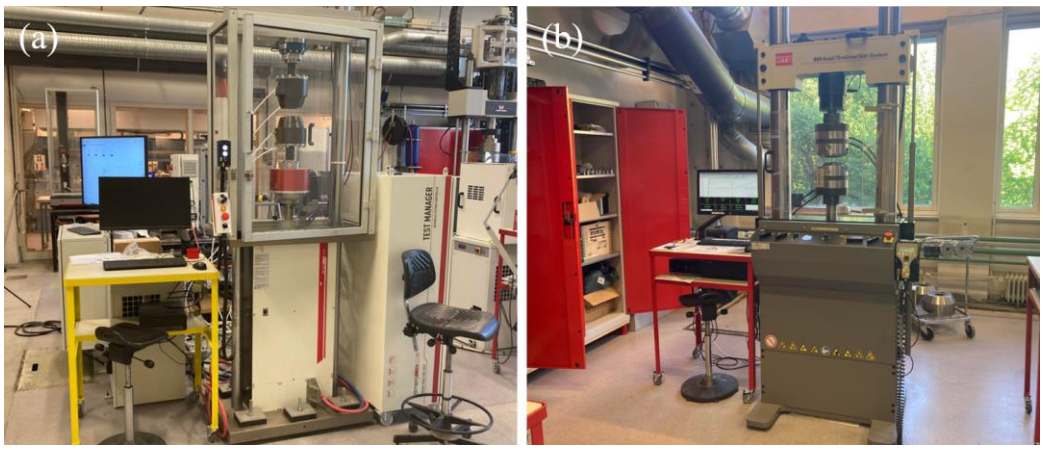

Figure 19: StepLab – Multiaxial 20 kN (a) and MTS 809 Axial/Torsional Test System (b) fatigue testing machines.

The specimens tested were flat dog bone shaped with a gauge length of 37 mm and a cross section in the gauge area of 6×10 mm. The specimen geometry is shown in Figure 20. Due to length of the grips of the fatigue testing machines, blocks were added to each end of the specimens to ensure the grips closed properly and held the specimen securely. These blocks were held to the ends of the specimen with tape. These blocks did not transfer load, so their attachment to the specimens had no influence on the fatigue results. The fatigue specimens were machined from blocks after glass bead blasting and pre-corrosion. As a result, only the front and back face had the surface condition to be tested. The side surfaces were not ground or polished, retaining the machined finish from the milling process.

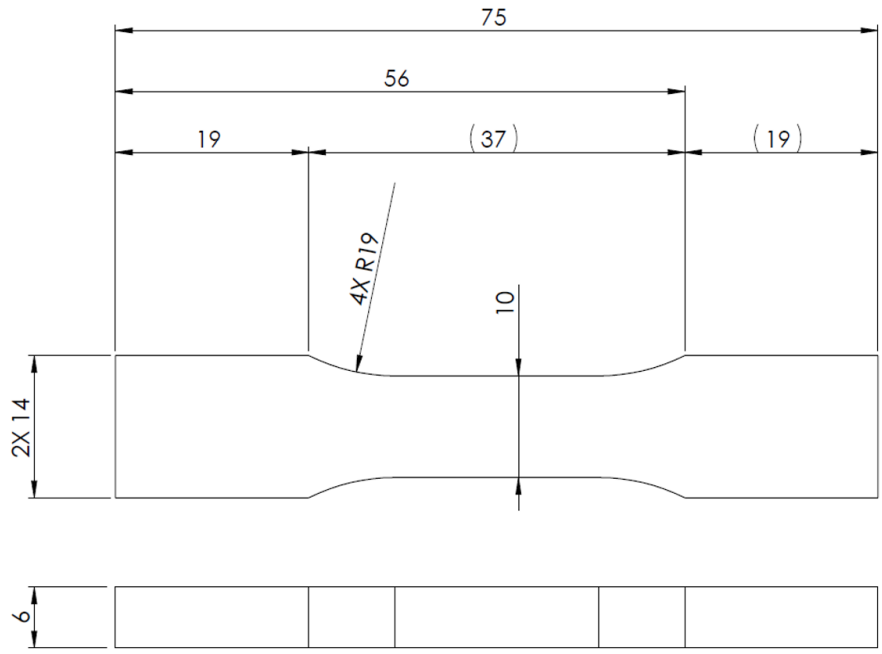

Figure 20: Fatigue specimen geometry. Dimensions in mm. Made by author.

Each condition was tested with three specimens. This number of repetitions was selected as it provided a tradeoff between providing enough data points for the results to be representative, without testing more specimens than necessary, which would in turn restrict the number of different conditions that could be assessed as part of the scope of this project. In addition to providing adequate certainty in the average fatigue life result for each condition, testing several specimens also provided insight into the distribution of fatigue lives for each condition. Due to the statistical nature of crack initiation in fatigue, the size of the scatter can itself be an important indicator of the nature of the fatigue failure.

3.2.6. Fractography

Fracture surfaces of fatigue tested specimens were examined with a scanning electron microscope (SEM) with four main objectives. Firstly, fracture surfaces were examined to understand the influence of pre-corrosion and glass bead blasting on crack initiation. This was done through detailed examination on the fracture surface of one fatigue specimen for each condition. The second objective was to observe the effects of pre-corrosion and glass bead blasting on the surface. This was done by examining the side surfaces of four fatigue specimens,

as extruded and glass bead blasted specimen with and without corrosion. The third objective was to measure the size of the defect caused by pre-corrosion responsible from crack initiation, to relate its size to the fatigue life. This was done for all fatigue specimens tested with pre-corrosion. As described in section 2.3.3., the root area method can be applied to relate the fatigue life to the initial stress intensity factor to describe the fatigue behavior as a function of load and defect size for specimens with known defects. The fourth objective was measuring the striation spacing at different crack lengths for one uncorroded as extruded specimen. These measurements were used in determining the Paris law coefficients as described in section 2.3.3.

A scanning electron microscope (SEM) captures images of a sample by scanning the surface with a focused electron beam [47]. A highly focused electron beam scans the surface point for point, while a detector registers the electrons from that point on the surface. The contrast in the produced image comes from differences in intensity of the stream of electrons detected, which amongst other things is determined by the topography of the surface [47]. Advantages of SEM compared to optical microscopy is that SEM can capture high-resolution images at higher magnification and has a much higher depth of field, allowing for sharp images to be captured of non-flat surfaces at high magnification [47].

Different detectors are used in SEM depending on what purpose of examination. The most important detection methods are secondary electron detection (SE) and back scattered electron detection (BSE) [48]. Secondary electrons are electrons that originate from inelastic interactions between the electron beam and the atoms close to the surface of the sample [48]. This form of electron detection is good at capturing the topography of the sample surface in high resolution [48]. SE is the main form of electron detection in SEM. BSE detection detects electrons that are reflected by elastic scattering when the electron beam hits the sample [48]. These electrons have much higher energy than secondary electrons, which allows them to escape the sample form deeper under the surface. This form of detection is good at capturing features of microstructure, such as different phases and particles in the surface [48].

Samples containing one side of the fracture were prepared for SEM by cutting the fatigue specimen next to the fracture and cleaning the sample. The cutting was done with the Struers precision cutting machine shown in Figure 11 (a). The sample were cleaned in ethanol in an ultrasonic cleaner for 5 minutes, before being dried with hot air. Cleaned samples were placed in individual plastic bags and only handled with gloves to prevent contamination.

The SEM used was a FEI Quanta 650 FEG. For failure mechanism examination in SEM, the samples were placed on the stage with the fracture surface facing up towards the electron beam and detectors. Images were captured of the crack initiation and crack propagation areas of the fracture surface with SE detection at different magnifications from 20x up to 1000x. Special attention was given to the crack initiation area and corrosion damage. For SEM observation of specimen side surfaces for selected conditions, BSE detection was used as it allows microstructural features to be identified.

Measurement of the size of the defect area was done in two ways. First a smooth area containing the entire defect was measured. This is the method originally proposed by Murakami [25]. In addition, an area following the exact shape of the defect was measured. This method has been

shown to be more accurate in some cases [26]. Determining the defect responsible for crack initiation was done by following the crack propagation lines in the crack growth area back to the initiation point. If several defects were possible candidates, the largest one was used. Determining the area constituting the defect was done by limiting it to where clear signs of corrosion could be identified. These signs were intergranular corrosion cracks and tiny pits in subsurface grains exposed to corrosion. Observation of these tiny pits is described and explained in sections 4.6. and 5.1.3. For heavily corroded conditions where corrosion damage was connected along the entire surface, the measured defect area was limited to areas where corrosion damage was clearly connected had contributed the same crack initiation. Images demonstrating the defect area measurement criteria are shown in section 4.6.

For measurement of striation spacing, the crack propagation path was identified, and four points were selected along this path at approximately 2, 3, 4, and 5 mm from the crack initiation point as shown in Figure 21. At each of the selected points four images were captured at a magnification high enough to identify the striation lines. The precise location of the images was determined by where the striation lines were most clearly visible and the apparent flatness of the fracture surface at the relevant location. Selecting areas which are perpendicular to the fracture surface is necessary to give accurate striation spacing measurement. The precise coordinates of the locations for striation measurement were also recorded to allow for precise calculation of the crack lengths.

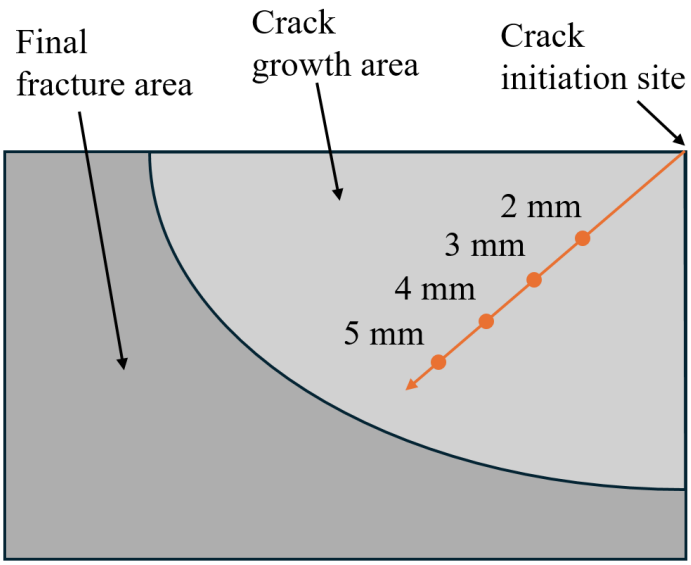

Figure 21: Striation spacing measurement locations.

4. Results

This chapter presents the results of the each of the testing and measurement forms separately.

4.1. Microstructure

The grain structure was examined for the cross section of an uncorroded as extruded specimen, an uncorroded glass bead blasted specimen, and an as extruded specimen with 24 hours of pre-corrosion. Figure 22 (a) shows the grain structure of the as extruded specimen. The small dark spots are pores in the oxide layer which is a result of the anodization process. The larger dark areas are larger damage also caused by the anodization process.

The center of the specimen had consistent small grains with an elongated shape from the extrusion process. Close to the surface there was a recrystallized layer with large equiaxed grains. Figure 22 (b) and (c) shows the grain structure in the recrystallized layer in more detail. In this area, the grains were less consistent in size. Smaller grains were generally found at the surface, while the rest of the recrystallized layer comprised of very large grains, but still with varying size.

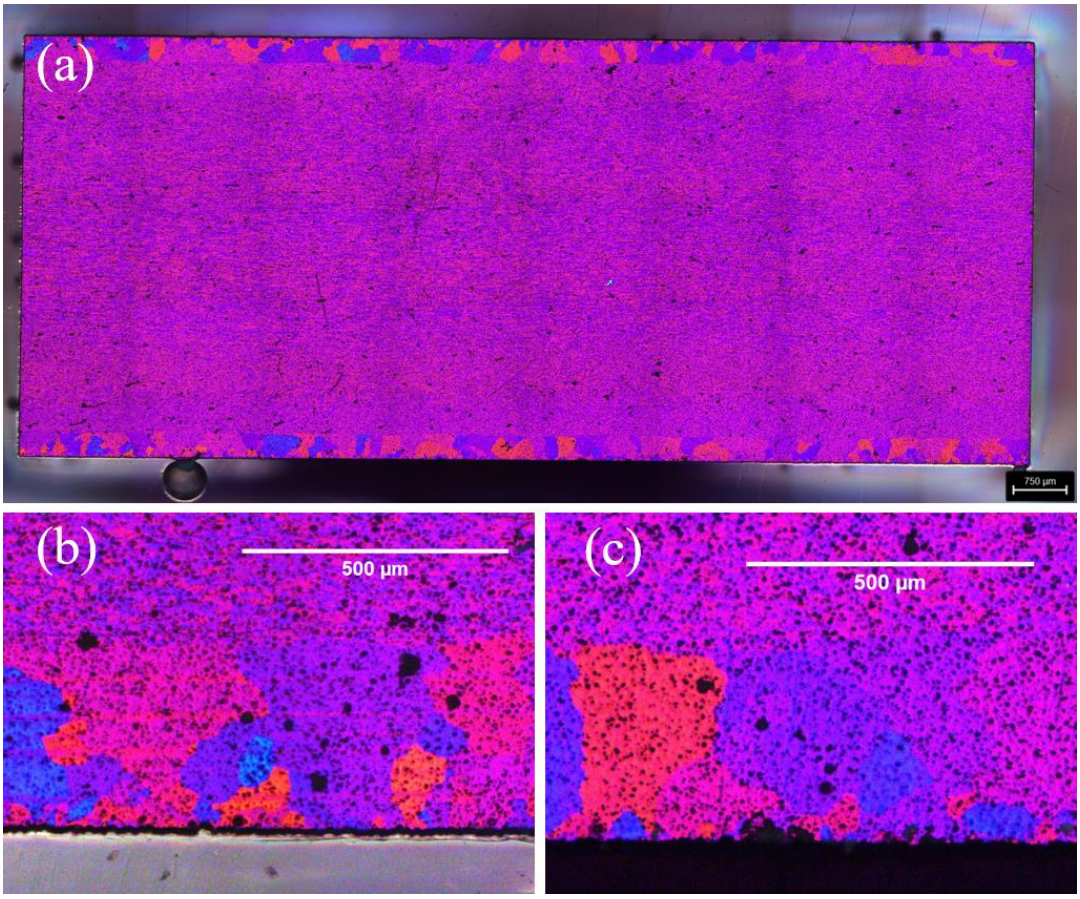

Figure 22: Grain structure of the as extruded sample. Image (a) shows the cross section of sample. Image (b) and (c) shows the recrystallized layer at higher magnification.

The depth of the recrystallized layer also varied along the surface. For the cross section examined here, the depth varied from around 319 to 383 µm. This is shown in Figure 23 (a) and (b).

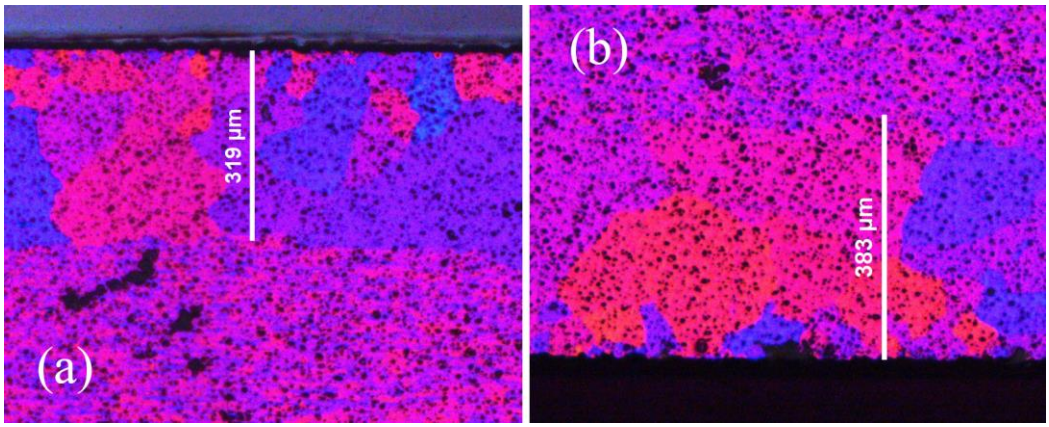

Figure 23: Minimum (a) and maximum (b) depth of the recrystallized layer for the examined sample.

Figure 24 (a) shows the grain structure of the glass bead blasted specimen. No noticeble change in grain structure was observed from the as extruded specimens. Figure 24 (b) and (c) shows the grain structure of the recrystallized layer in the glass bead blasted specimen next to the as extruded specimen.

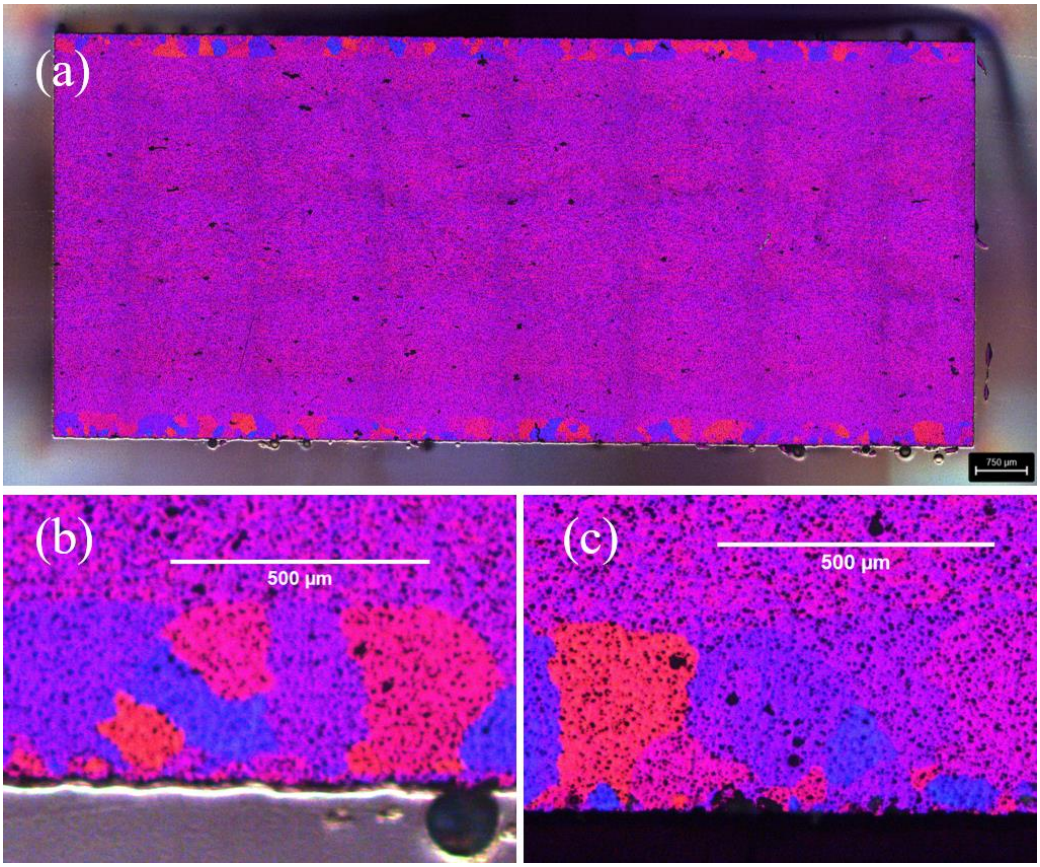

Figure 24: Grain structure of glass bead blasted specimen. Image (a) shows the cross section of sample. Image (b) shows the recrystallized layer of the glass bead blasted sample compared with the as extruded surface (c).

Figure 25 (a) shows the grain structure of a specimen after 24 hours of pre-corrosion. This image clearly shows the corrosion form to be intergranular corrosion, where corrosion followed the grain boundaries. A change in the appearance of the corrosion can be observed when the corrosion reached through the recrystallized layer into the center of the profile. Figure 25 (b)

shows the corrosion of the recrystallized layer in more detail. The intergranular corrosion appeared to reach deepest in areas where the grain structure allowed it to follow a relatively straight path from the surface through the recrystallized layer.

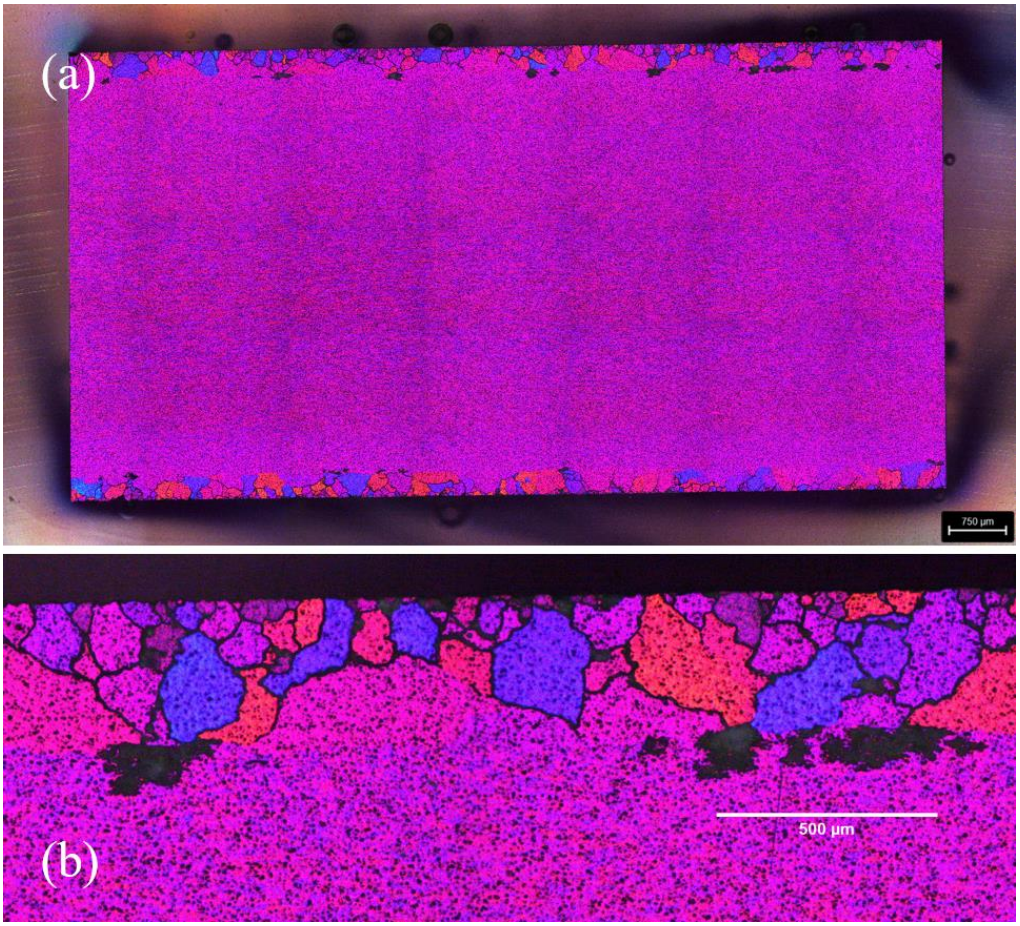

Figure 25: Grain structure of the as extruded specimen with 24 h pre-corrosion. Image (a) shows the entire sample cross section. Image (b) shows the intergranular corrosion at higher magnification.

4.2. Hardness

Hardness was measured along three lines from the surface towards the center of the profile for as extruded and glass bead blasted surface conditions. All hardness measurements are presented in Table 19 and Table 20. Figure 26 shows the hardness for each condition as a function of depth from the surface. The points represent the average hardness of the three measurements at each depth. The whiskers represent sample standard deviation from the three recorded values. The hardness profile for both conditions had a slight peak around 0.2 to 0.3 mm under the surface. The glass bead blasted specimen had slightly higher hardness overall, but considerably higher around the 0.2 to 0.3 mm peak.

Table 19: Vickers microhardness (HV) measurements for as extruded sample.

Depth [mm]	Line 1	Line 2	Line 3	Average	Standard deviation
0.1	105.3	107.9	103.4	105.5	2.259
0.2	112.7	114.0	108.1	111.6	3.100
0.3	114.1	110.9	111.1	112.0	1.793
0.4	109.7	112.2	108.0	110.0	2.113
0.5	107.8	113.8	107.2	109.6	3.650
1	106.6	108.1	113.9	109.5	3.855
1.5	109.4	105.4	103.8	106.2	2.884

Table 20: Vickers microhardness (HV) measurements for glass bead blasted sample.

Depth [mm]	Line 1	Line 2	Line 3	Average	Standard deviation
0.1	102.3	115.5	116.2	111.3	7.831
0.2	113.9	122.5	113.8	116.7	4.994
0.3	120.9	117.2	119.1	119.1	1.850
0.4	111.7	112.5	113.2	112.5	0.751
0.5	114.4	115.0	110.3	113.2	2.558
1	113.8	112.8	108.0	111.5	3.101
1.5	113.0	108.8	108.0	109.9	2.686

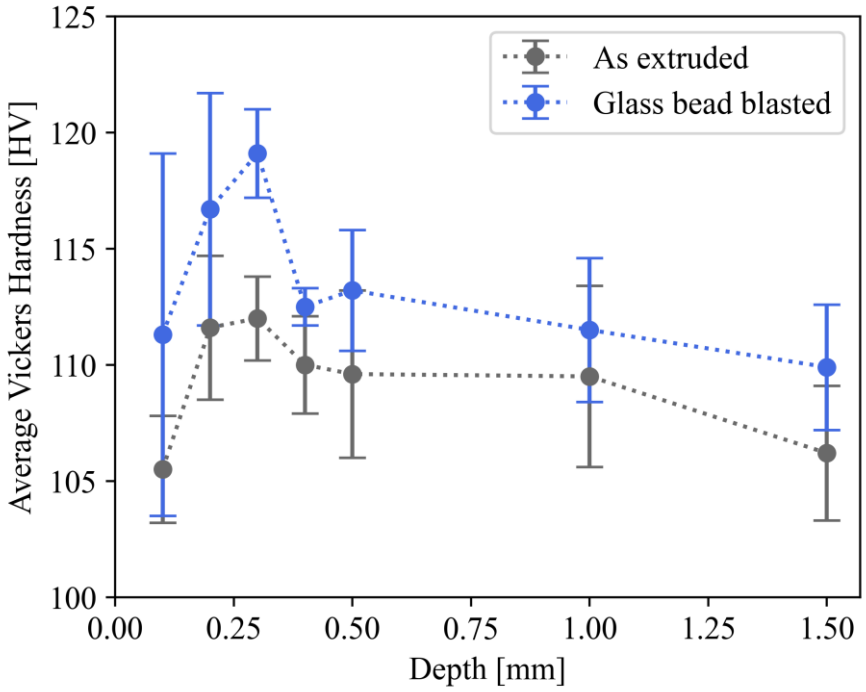

Figure 26: Hardness as a function of depth for as extruded and glass bead blasted surface conditions.

4.3. Corrosion Depth

The intergranular corrosion depth was measured with an optical microscope for two cross sections, referred to as A and B, of the dedicated corrosion characterization specimens for each condition. This means the corrosion depths were examined in a total of four areas per condition, two cross sections with two sides each. The designations for areas and sides are illustrated in Figure 15. The side designations front (F) and back (B) but were selected arbitrarily, and do not reflect the sides on the original extruded profile or which side experienced most severe corrosion. For each side of each cross section, the three largest intergranular corrosion depths were recorded. Table 21 shows all the recorded corrosion depth values for all corrosion levels for both as extruded and glass bead blasted surfaces.

Table 21: Measured corrosion depths.

Surface condition	Corrosion duration [h]	Cross section	Side	Depth 1 [µm]	Depth 2 [µm]	Depth 3 [µm]
As extruded	1	A	F	112	76	70
As extruded	1	A	B	69	61	49
As extruded	1	B	F	110	48	46
As extruded	1	B	B	75	75	74
As extruded	4	A	F	130	49	30
As extruded	4	A	B	234	89	79
As extruded	4	B	F	241	216	204
As extruded	4	B	B	158	66	62
As extruded	12	A	F	209	174	157
As extruded	12	A	B	85	75	61
As extruded	12	B	F	155	85	74
As extruded	12	B	B	246	227	191
As extruded	24	A	F	414	413	402
As extruded	24	A	B	393	373	335
As extruded	24	B	F	333	277	268
As extruded	24	B	B	424	398	394
GBB	12	A	F	368	335	331
GBB	12	A	B	368	278	272
GBB	12	B	F	259	261	200
GBB	12	B	B	357	355	347
GBB	24	A	F	396	388	347
GBB	24	A	B	425	412	402
GBB	24	B	F	384	332	286
GBB	24	B	B	423	389	383

Figure 27 compares the average of the three deepest points of intergranular corrosion between each side for each condition. The maximum corrosion depth for each condition is shown in

orange. The corrosion depth is higher for longer corrosion durations. The corrosion depth is higher for glass bead blasted surfaces than for as extruded surfaces with the same corrosion time. The average of three highest depths in the most severely corroded area was close to the maximum for each condition. The corrosion depth varied considerably between each area examined within the same corrosion condition. This indicates that corrosion damage has substantial local variation. The variation between each area is smallest for 1 h pre-corrosion, largest for the middle conditions of 4 and 12 h, and smaller again for the highest corrosion conditions. This indicates that corrosion depth first increases locally in some areas before becoming more widespread after longer exposure.

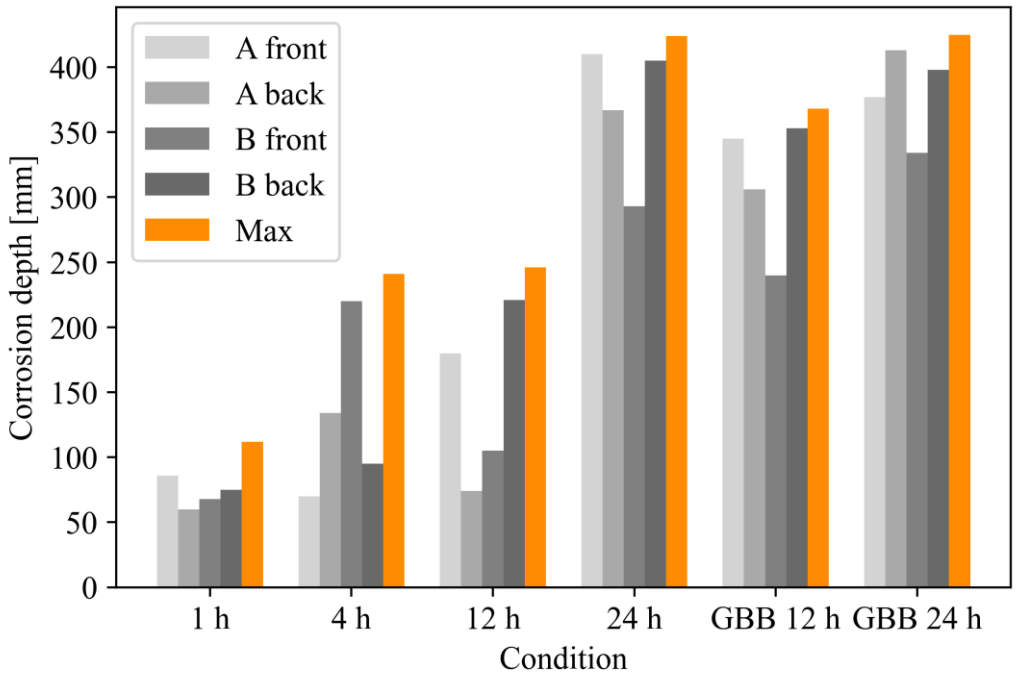

Figure 27: Average of three highest corrosion depths for each area examined compared to maximum depth per condition.

Table 22 shows the maximum recorded depth of intergranular corrosion, the average of all recorded depths, and the difference between the highest and lowest corrosion depths recorded. The difference between average depth for each side is referred to as the depth variation. Note that average refers to the average of the recorded depths, meaning the three deepest points per examined area.

Table 22: Maximum corrosion depth per condition. Average corrosion depth refers to the average of the three deepest points per examined area. Corrosion depth variation refers to the difference between the highest and lowest corrosion depth recorded.

Surface condition	Corrosion duration [h]	Maximum corrosion depth [µm]	Average corrosion depth [µm]	Corrosion depth variation [µm]
As extruded	1	112	72.1	66
As extruded	4	241	129.8	211
As extruded	12	246	144.9	185
As extruded	24	424	368.7	156
GBB	12	368	310.9	168
GBB	24	425	380.6	139

Figure 28 shows the maximum recorded depth of intergranular corrosion, the average of the recorded depths, and the variation in corrosion depth for each condition. The corrosion depth did not increase steadily with corrosion time, but increased rapidly up to 4 h pre-corrosion before slowing down up to 12 h pre-corrosion and then speeding up again until 24 h pre-corrosion. With 12 h pre-corrosion, the glass bead blasted surface had considerably more severe corrosion damage than the as extruded surface. With 24 h pre-corrosion, the difference was negligible.

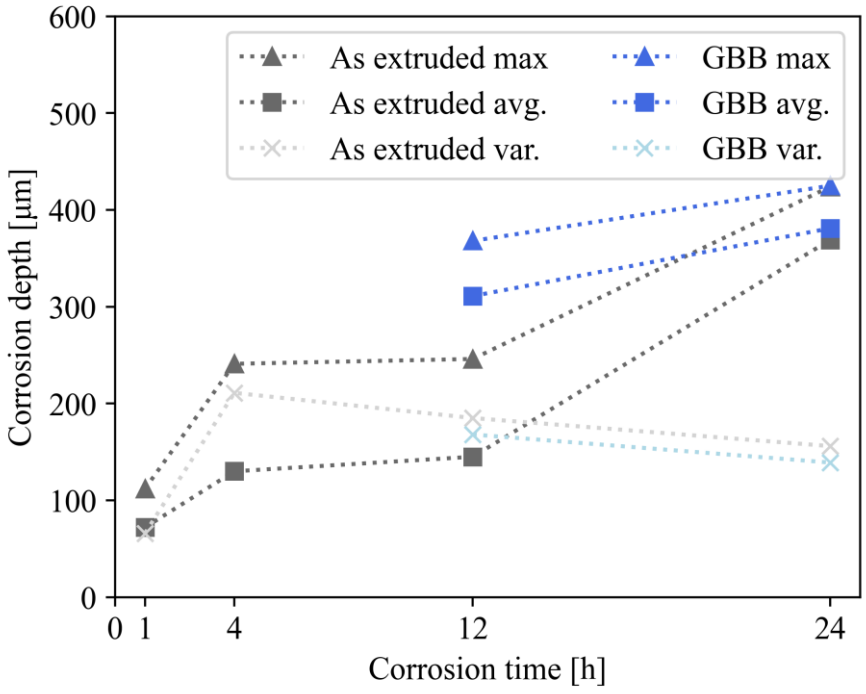

Figure 28: Maximum corrosion depth as function of corrosion time.

Figure 29 and Figure 30 shows the area of deepest intergranular corrosion for each condition.

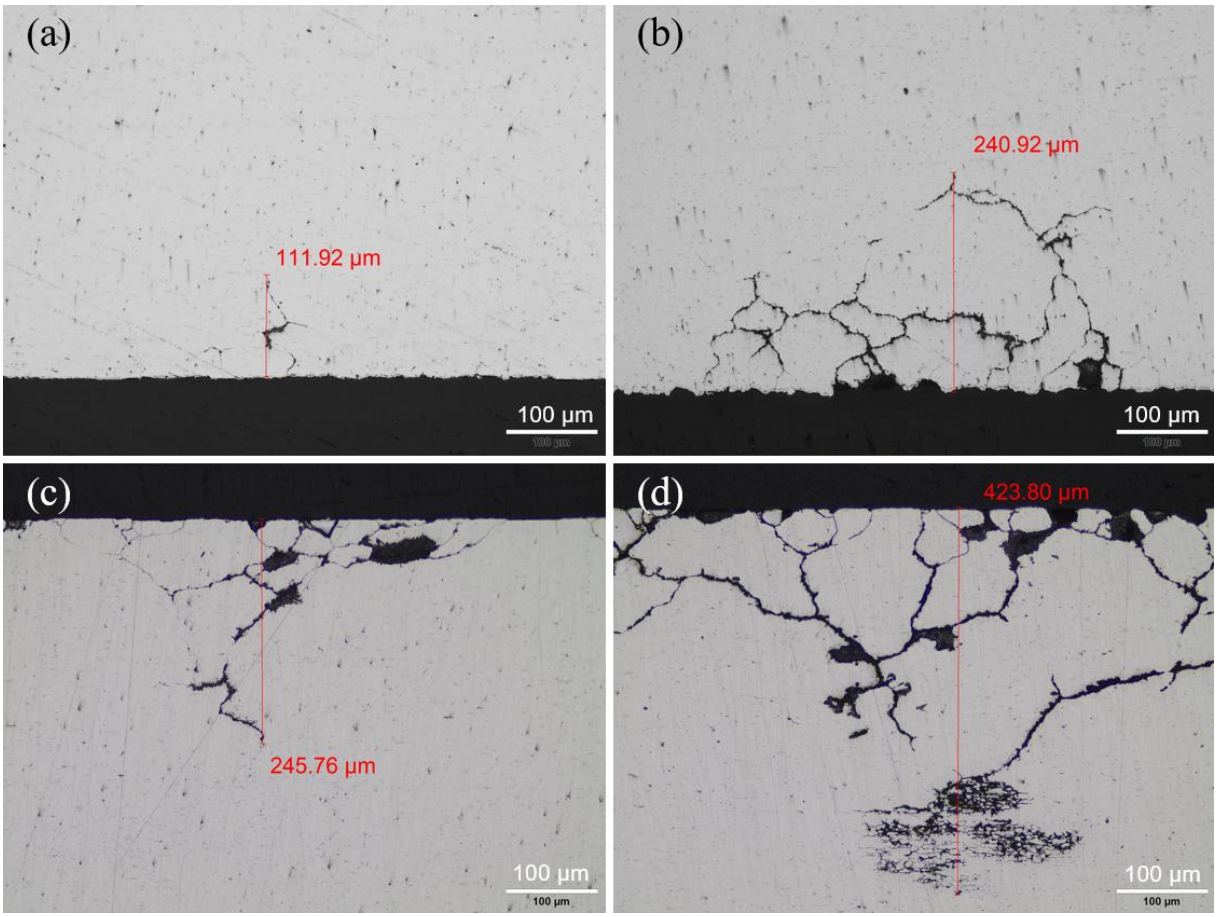

Figure 29: Corrosion damage for as extruded specimens with 1 h (a), 4 h (b), 12 h (c), and 24 h (d) of pre-corrosion.

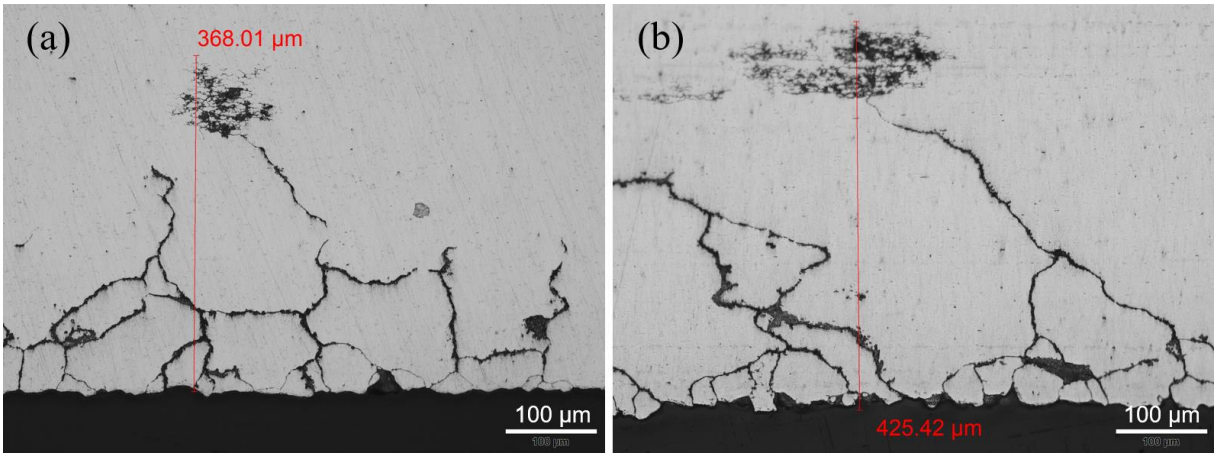

Figure 30: Corrosion damage for glass bead blasted conditions with 12 h (a) and 24 (b) of pre-corrosion.

4.4. Surface Topography

Surface Roughness Values

The surface topography was examined for all corrosion levels of as extruded and glass bead blasted surfaces. This was done by 3D-mapping of a sample area with a confocal microscope. Table 23 shows selected profile and area surface roughness values. For as extruded specimens the surface roughness increased considerably from uncorroded to the 1 h corroded condition. It

was similar for 1, 4, and 12 h corrosion. An increase is surface roughness was found between 12 and 24 h. For glass bead blasted surfaces, the surface roughness was reduced from uncorroded to 12 h corrosion. It then increased slightly from 12 to 24 h corrosion. Figure 31 shows *Ra*, *Rq*, and *Rz* for each surface condition as a bar chart.

Table 23: Surface roughness values.

Surface condition	**Corrosion duration [h]**	***Ra* [µm]**	***Rq* [µm]**	***Rt* [µm]**	***Rz* [µm]**	***Sa* [µm]**
As extruded	0	0.456	0.614	5.754	3.664	0.458
As extruded	1	1.442	1.964	13.576	10.669	1.505
As extruded	4	1.634	2.123	12.272	10.111	1.599
As extruded	12	1.472	1.811	8.595	8.000	1.508
As extruded	24	2.148	3.682	26.294	19.410	1.574
GBB	0	3.082	3.778	21.873	16.591	3.489
GBB	12	2.063	2.718	18.228	13.137	2.454
GBB	24	2.278	2.889	16.439	12.940	2.759

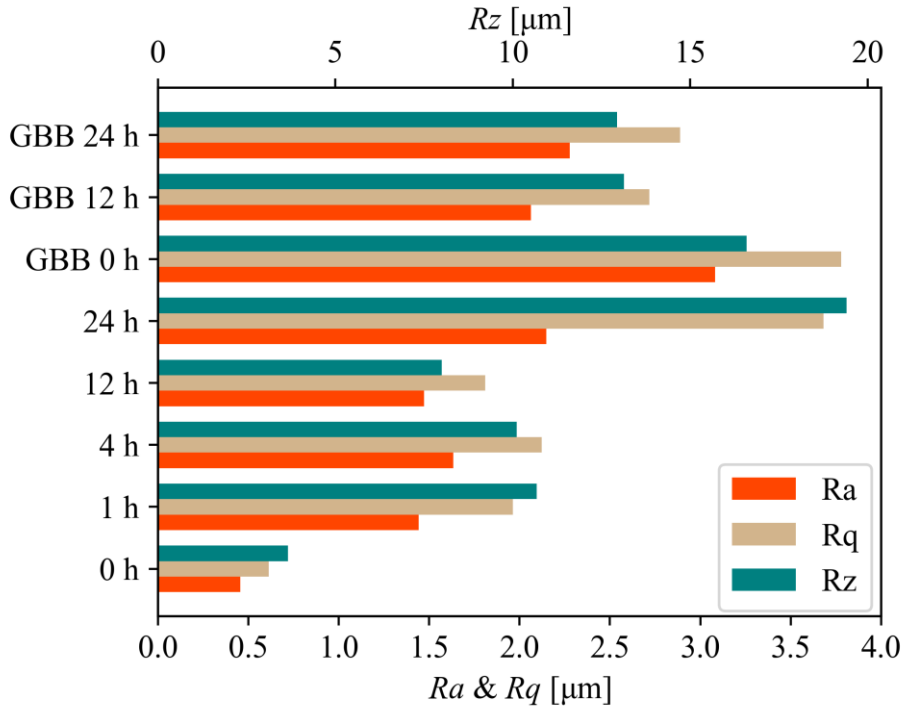

Figure 31: Bar chart of surface roughness values.

Surface Features and Profile

Figure 32 shows images of 3D maps of the sample areas for each condition. The colors represent deviation from mean height of each surface. The coloring is normalized to go from purple at 40 µm below to red at 20 µm above mean height. Figure 32 (a), (b), (c), (d), and (e) show the surface topography of the as extruded surfaces. These surfaces were characterized by long shallow grooves left by the extrusion die during extrusion. Figure 32 (e) shows localized pits

in the as extruded surface with 24 h pre-corrosion. These pits were likely left by grains freed from the surface rather than corrosion pits. Figure 32 (f), (g), and (h) show the surface topography of the glass bead blasted surfaces. The glass bead blasted surfaces were characterized by large shallow craters created by the impacts of glass beads.

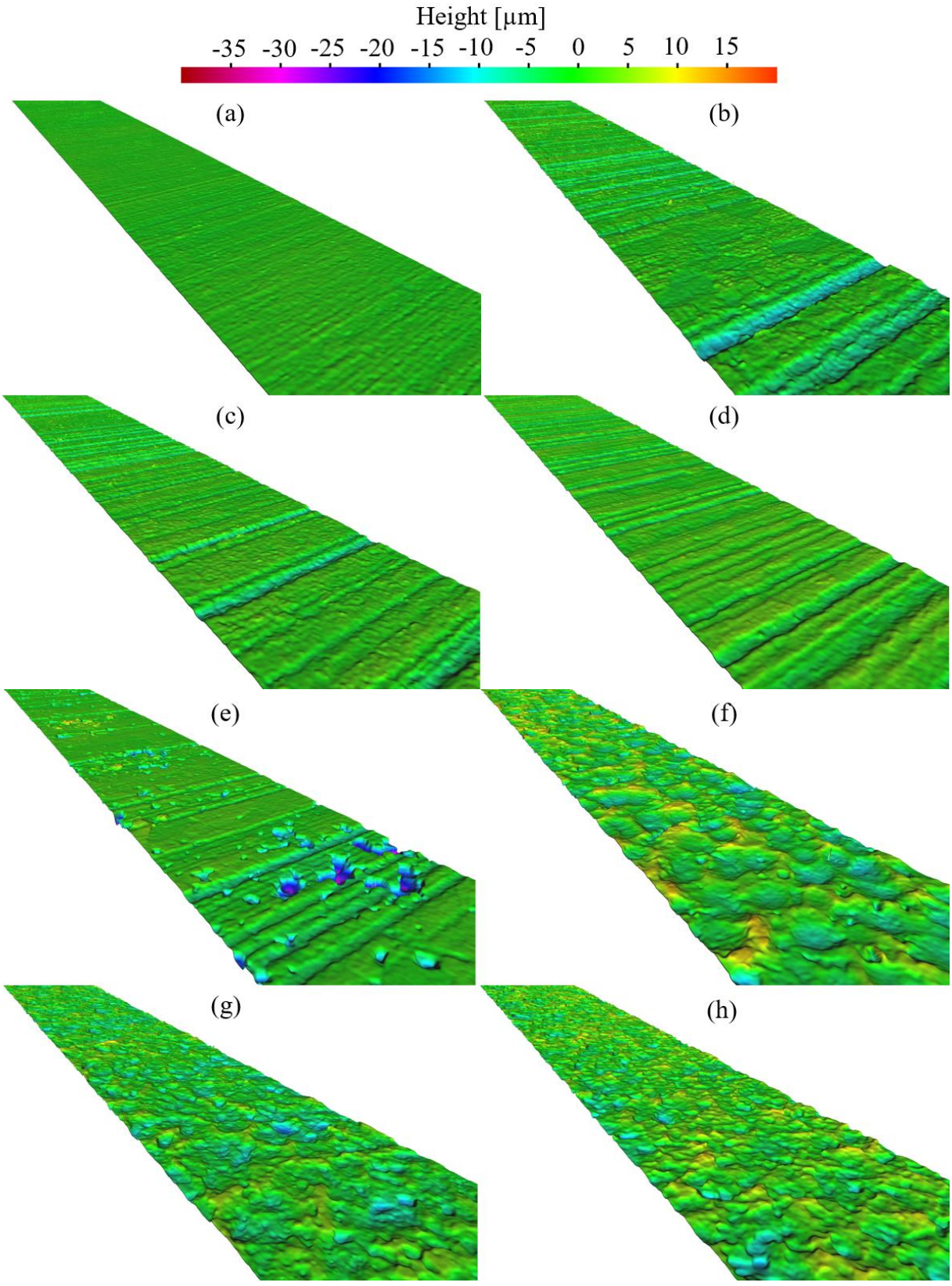

Figure 32: 3D-maps for as extruded surfaces uncorroded (a) and with 1 h (b), 4 h (c), 12 h (d), and 24 h (e) of pre-corrosion, and glass bead blasted surfaces uncorroded (f) and with 12 h (g) and 24 h (h) of pre-corrosion.

Figure 33, Figure 34, and Figure 35 compares surface profiles of as extruded and glass bead blasted surfaces with and without 24 h pre-corrosion. The height values are normalized so that

the maximum value in each presented profile length is 0. The length of the profiles compared were 1.2 mm. The areas presented were deliberately selected to contain local features characteristic for each condition, such as deep extrusion lines and corrosion damage. The comparison of the as extruded and glass bead blasted surface profiles, shown in Figure 33, shows that the glass bead blasted surface had wide and deep valleys from impact craters, compared to the much less rough extruded surface. The comparison of the as extruded surface with and without pre-corrosion in Figure 34 shows deep valleys left by freed surface grains. Figure 35 shows glass bead blasted surface profiles with and without corrosion. These are much more similar than the other comparisons. The only identifiable difference was some deeper valleys in the corroded surface, which could be a result of corrosion.

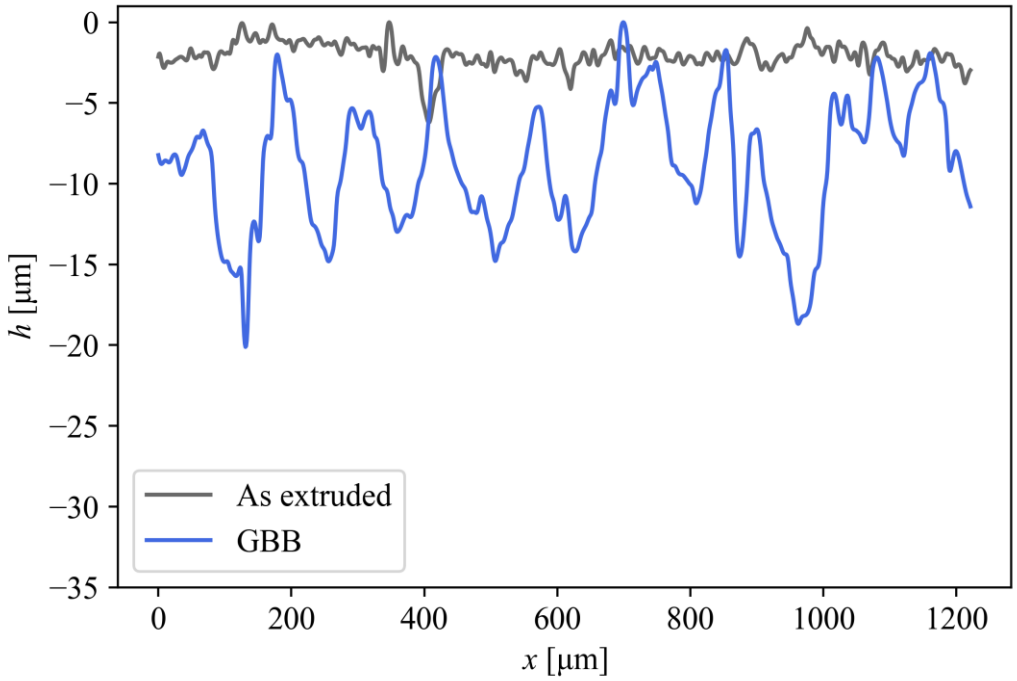

Figure 33: Comparison of surface profile of as extruded and GBB.

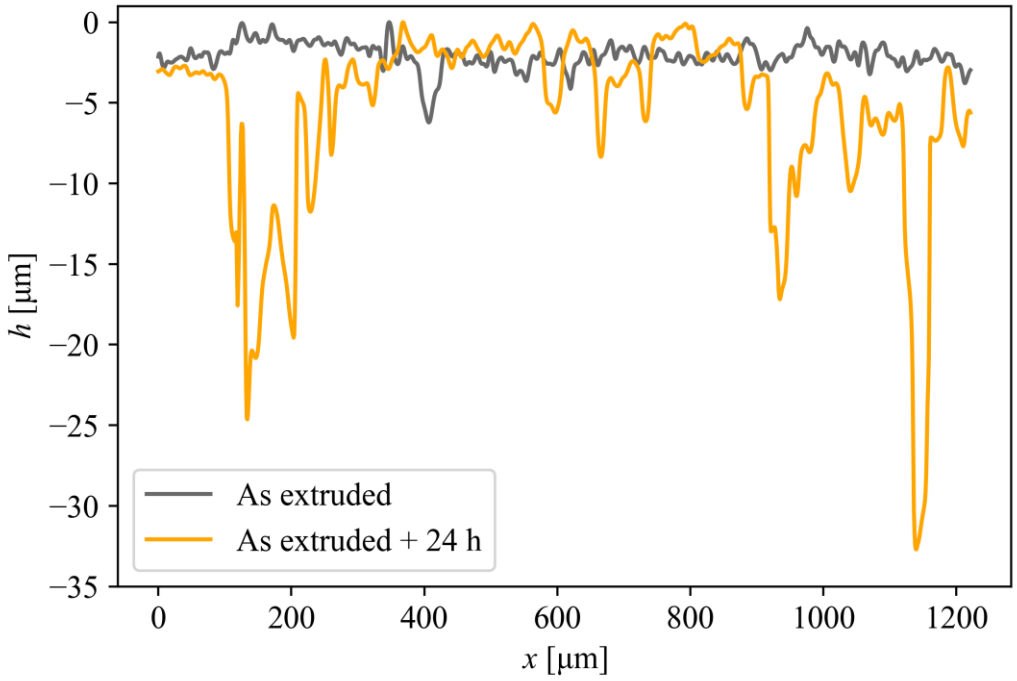

Figure 34: Comparison of surface profiles of as extruded with and without corrosion.

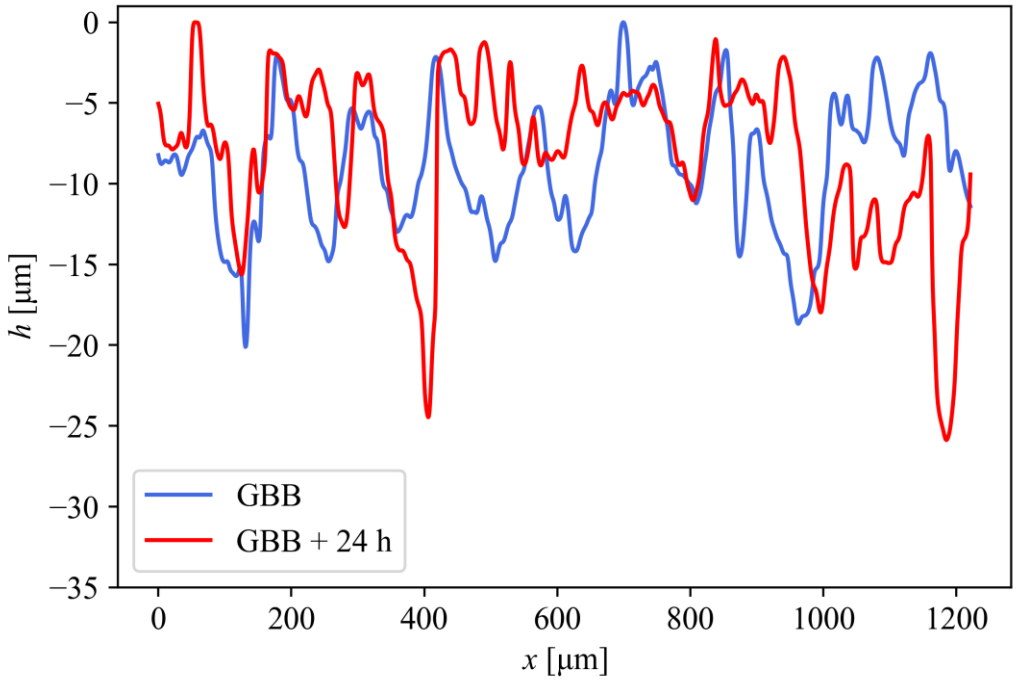

Figure 35: Comparison of surface profile of GBB with and without corrosion.

Figure 36 compares a surface roughness profile of the uncorroded as extruded surface with the machined finish of the fatigue specimen sides. Note the different scale on the y-axis compared with the other profile comparisons. The machined surface profile had a regular pattern corresponding with each cut made by the mill. The as extruded profile had a more irregular pattern with some deeper grooves, one of which was captured as part of the profile shown. The surface roughness values for the machined finish on the side of fatigue specimens was similar

to the as extruded surface with *Ra* = 0.447 µm and *Rz* = 2.661 µm compared to *Ra* = 0.456 µm and *Rz* = 3.664 µm for the as extruded surface.

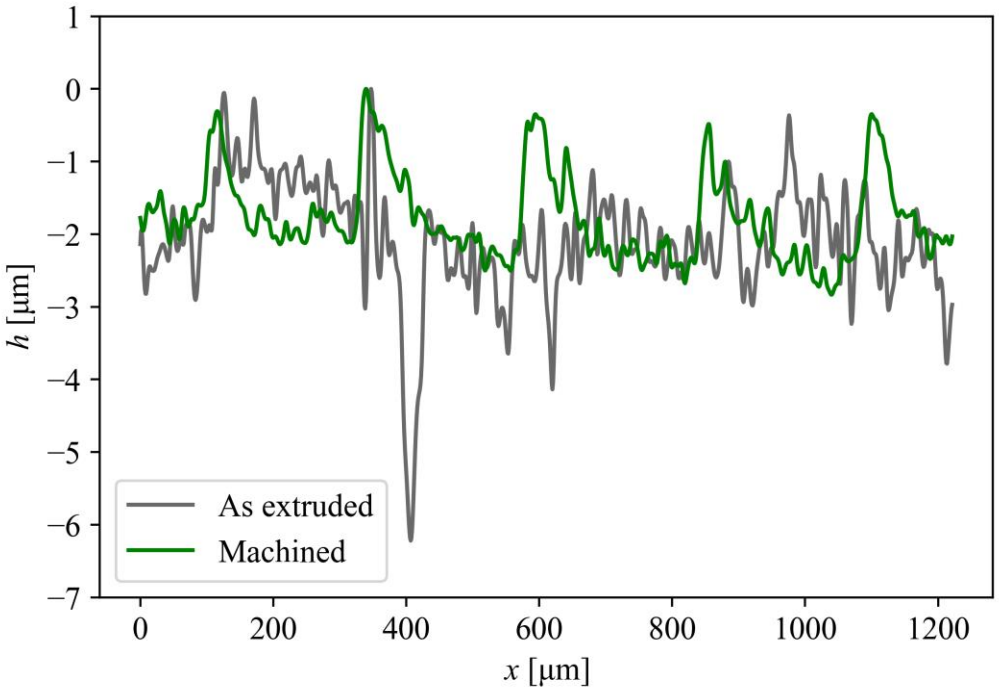

Figure 36: Comparison of surface profile of as extruded and machined sides of fatigue specimen. Note the different scale on the y-axis compared with the other profile comparisons.

Post-Fatigue Surface Topography

Table 24 shows the surface roughness values close the crack growth area after fatigue testing. These were obtained for as extruded and glass bead blasted surfaces with no corrosion and 24 hours of pre-corrosion.

Table 24: Surface roughness values, post-fatigue.

Surface condition	**Corrosion duration [h]**	***Ra* [µm]**	***Rq* [µm]**	***Rt* [µm]**	***Rz* [µm]**	***Sa* [µm]**
As extruded	0	0.405	0.529	3.845	2.881	0.423
As extruded	24	2.340	3.145	18.123	15.733	3.048
GBB	0	2.508	3.065	15.721	13.801	2.729
GBB	24	5.788	9.192	77.293	36.760	5.913

Figure 37 compares *Ra* before and after fatigue testing. The change is insignificant for all specimens except for the glass bead blasted specimen with 24 hours of pre-corrosion. For this condition, the surface roughness increased substantially after fatigue loading.

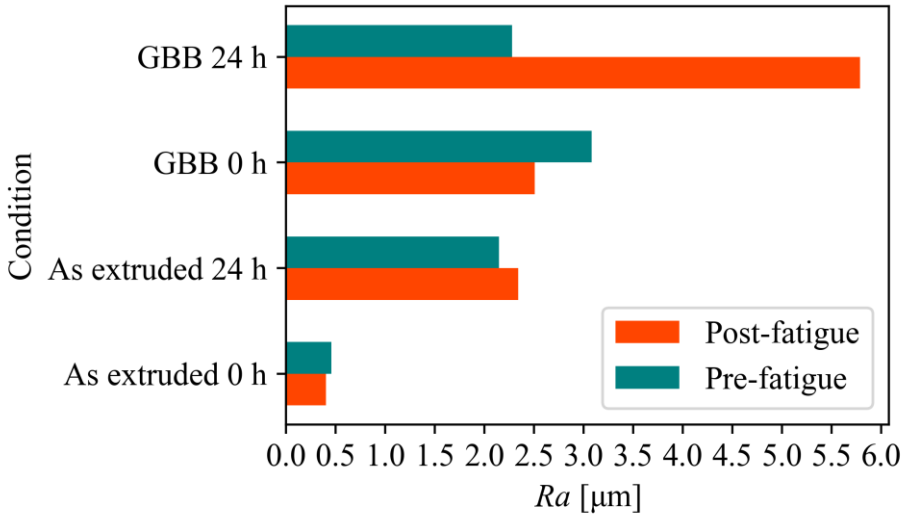

Figure 37: Comparison of surface roughness before and after fatigue loading.

Figure 38 shows a comparison of sample areas of the glass bead blasted condition with 24 h pre-corrosion before and after fatigue loading. The images show pits most likely left by surface grains that have been freed from the surface. For the as extruded surface with 24 h pre-corrosion this was seen also before fatigue loading and therefore did not result in a difference before and after fatigue.

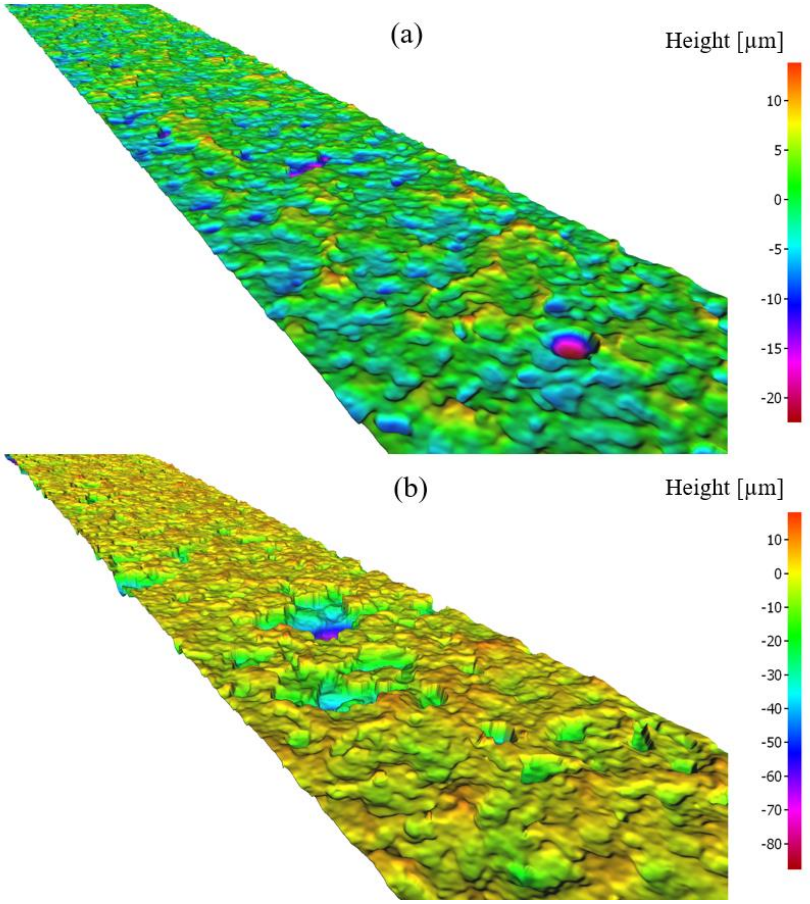

Figure 38: Comparison of 3D-maps of glass bead blasted surface with 24 h pre-corrosion before (a) and after (b) fatigue. Note that the color bars are not the same for both images.

4.5. Fatigue Testing

Fatigue testing was performed for three specimens per condition. Table 25 shows the fatigue life of each of the as extruded specimens. The table also shows the average life at each corrosion time and the sample standard deviation based on the three tests. A drastic reduction in fatigue life was found from the uncorroded to the corroded specimens. There was also a gradual further reduction in fatigue life with increasing corrosion duration. The fatigue lives of the uncorroded specimens were very scattered. However, for corroded specimens the scatter was much lower.

Table 25: Fatigue lives for as extruded specimens.

Corrosion duration [h]	**Fatigue life, N_f [cycles]**	**Average fatigue life [cycles]**	**Standard deviation [cycles]**	**Standard deviation [%]**
0	153 070 261 332 310 312	241 571	80 462	33.3
1	108 237 82 224 91 082	93 848	13 225	14.1
4	73 121 77 566 78 458	76 382	2 859	3.74
12	85 771 68 458 83 701	79 310	9 455	11.9
24	68 449 59 396 71 214	66 353	6 182	9.32

Table 26 shows the fatigue life for each of the glass bead blasted specimens. Similar behavior was seen as with the as extruded specimens in terms of relationship between corrosion and fatigue life. The fatigue life was drastically reduced from uncorroded to corroded specimens. There was also a slight reduction between 12 and 24 h corrosion. The fatigue lives are generally higher for glass bead blasted specimens than for as extruded specimens, especially in the uncorroded condition.

Table 26: Fatigue lives for glass bead blasted specimens.

Corrosion time [h]	Fatigue life, N_f [cycles]	Average fatigue life [cycles]	Standard deviation [cycles]	Standard deviation [%]
0	1 337 188 1 180 097 306 292	941 192	555 422	59.0
12	89 876 80 341 90 711	86 976	5 761	6.62
24	66 046 77 413 75 514	72 991	6 089	8.34

Figure 39 shows the fatigue lives for all fatigue tested specimens of both extruded and glass bead blasted conditions as a function of corrosion duration. As mentioned above, the uncorroded specimens show wide scatter in fatigue lives while the corroded specimens are more consistent.

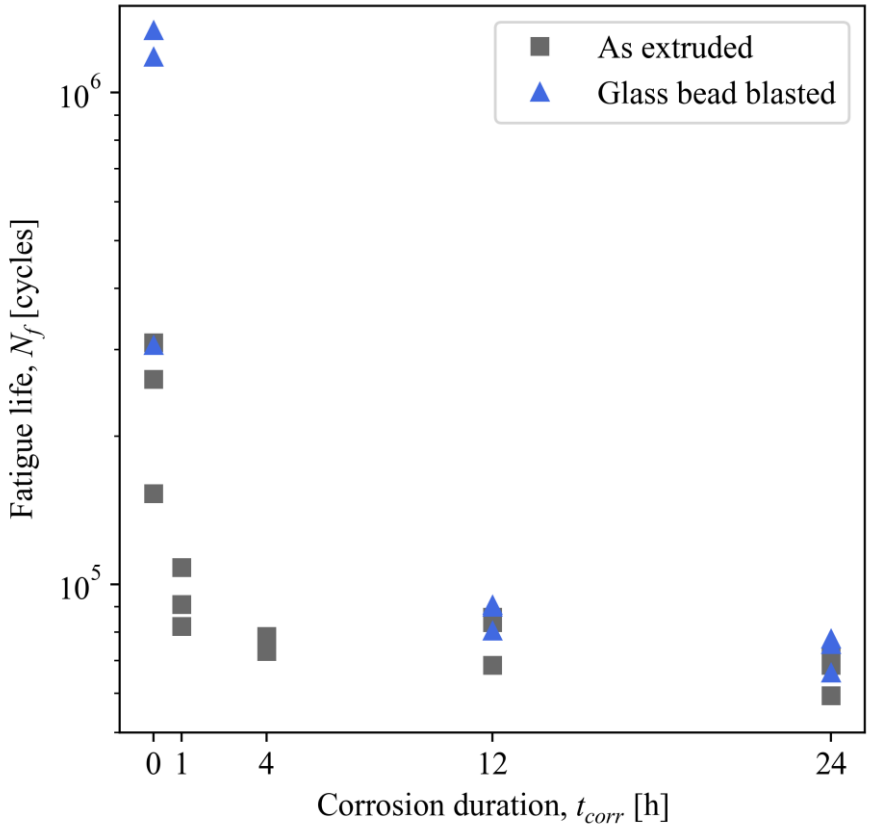

Figure 39: Fatigue life as function of corrosion time.

Figure 40 shows the fatigue lives of the pre-corroded specimens as a function of maximum corrosion depth measured for each condition on the dedicated corrosion characterization specimen. The different corrosion durations are represented with different markers for gray and blue for as extruded and glass bead blasted respectively. Presented like this, a clear trend between corrosion damage and fatigue life can be identified. The glass bead blasted specimens perform better than the as extruded, especially with 12 h pre-corrosion where glass bead blasted specimens had more severe corrosion damage and longer fatigue lives. The results showed that the relation between corrosion damage and fatigue life followed a different trend for glass bead blasted specimens compared to as extruded specimens.

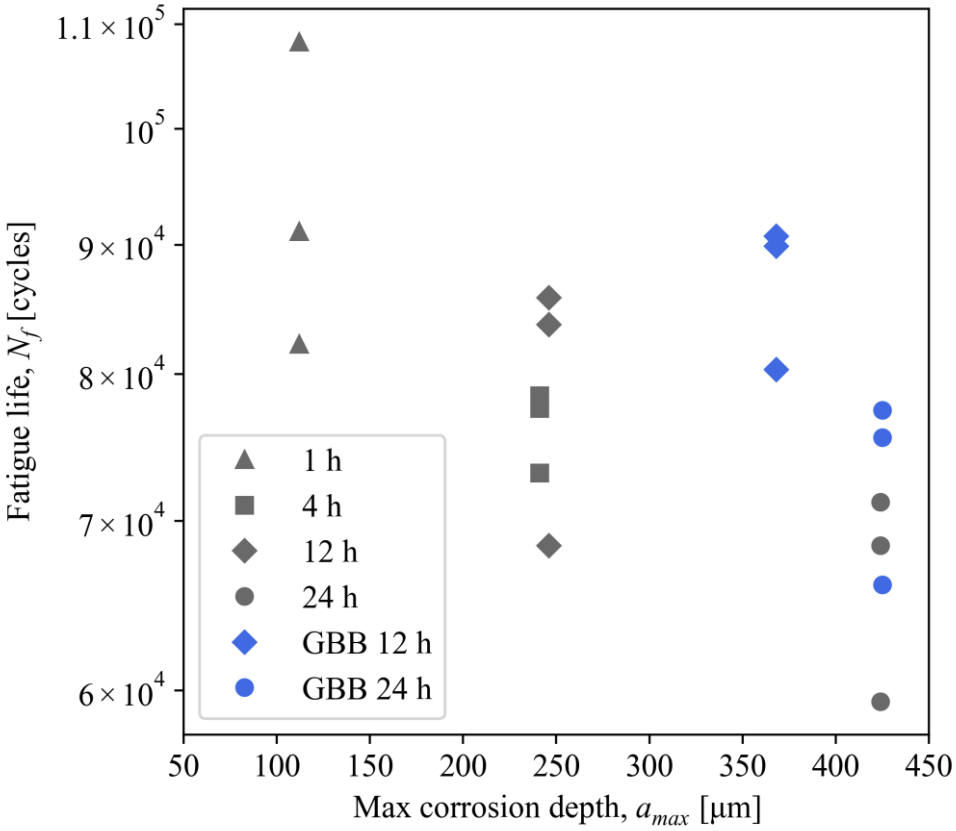

Figure 40: Fatigue life to max corrosion depth.

4.6. Fractography

Failure Mechanisms

The fracture surfaces were examined in SEM for one fatigue specimen for each condition to identify the failure mechanism. Figure 41 (a) shows the crack growth area for the uncorroded as extruded specimen with a fatigue life of 310 312 cycles. The fatigue crack initiated from the front face close to the corner of the specimen. Figure 41 (b) shows the crack initiation and early crack propagation area at higher magnification. The early crack propagation area is characterized by river markings running in the crack propagation direction. Around 200-300 µm from the initiation area the crack enters stable crack propagation.

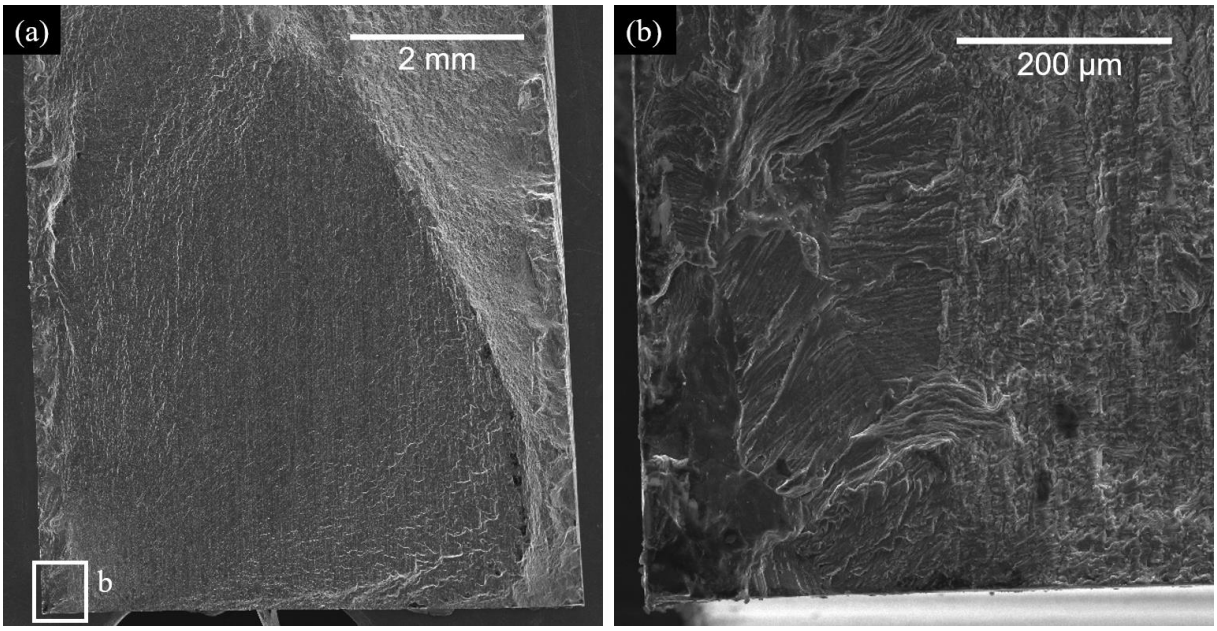

Figure 41: Fracture surface of uncorroded as extruded specimen.

Figure 42 (a) shows the crack growth area for the 24 h pre-corroded specimen with a fatigue life of 68 449 cycles. This specimen showed multiple crack initiations along the corroded face. The main crack initiation area was close the corner of the specimen. This area is shown in more detail in Figure 42 (b). This specimen did not show an area of early crack propagation as seen in the uncorroded specimen. Instead, stable crack propagation started almost directly from the corrosion damage depth. This specimen, and other pre-corroded specimens, also showed multiple crack initiation sites on the opposite edge from the crack growth area. For most specimens these crack initiation sites had not developed into stable crack growth. Although, a few pre-corroded specimens did have two or three crack growth areas originating from separate corners.

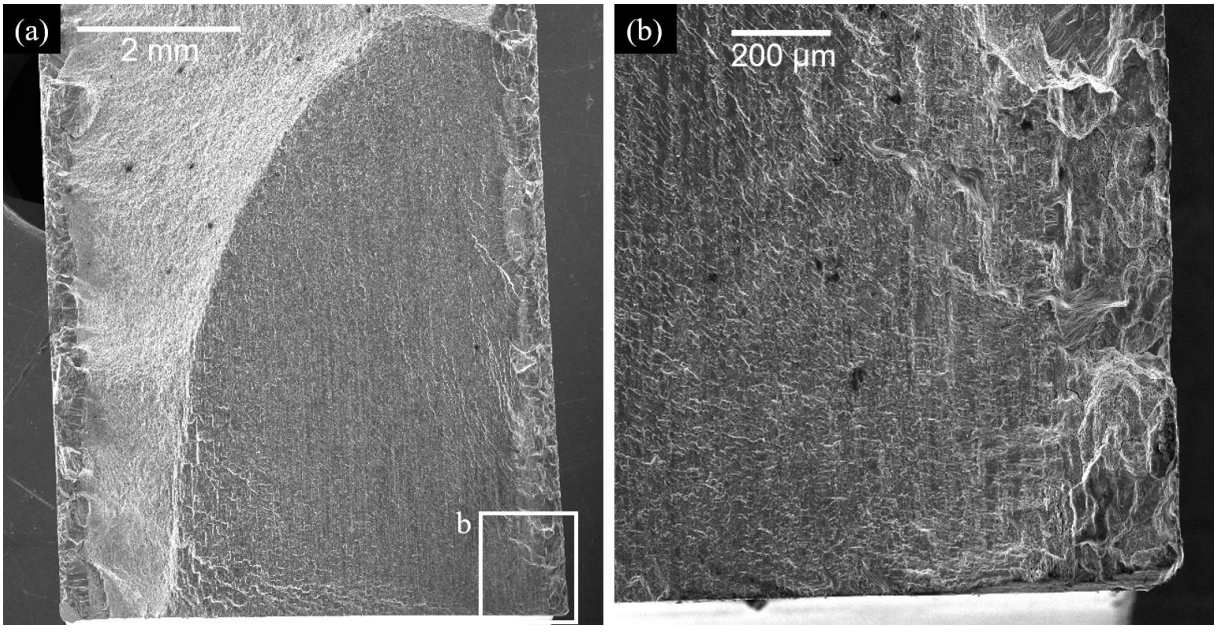

Figure 42: Fracture surface of as extruded specimen with 24 h pre-corrosion.

Figure 43 (a) shows the crack growth area of the uncorroded glass bead blasted specimen with a fatigue life of 1 337 188 cycles. Figure 43 (b) shows the crack initiation area at higher magnification. The crack initiation appeared to be close to the corner on the side face of the specimen, as opposed to on the front face for the as extruded specimen. From the crack initiation area, river markings indicating early crack propagation was seen through the recrystallized layer before stable crack growth started in the fine grained center.

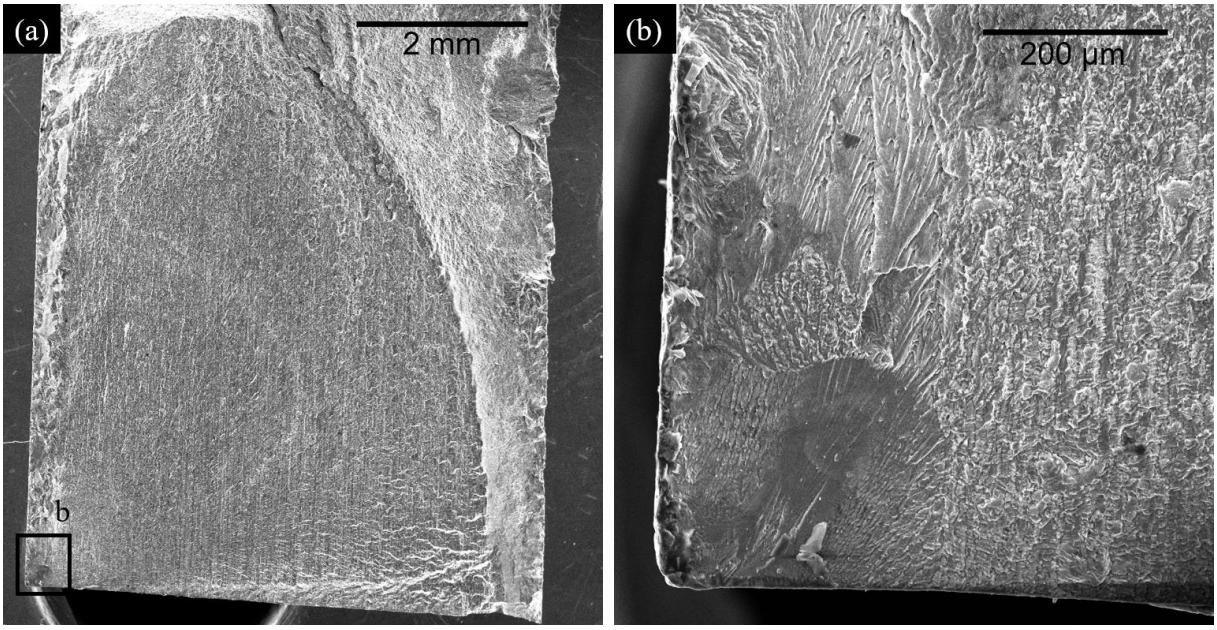

Figure 43: Fracture surface of uncorroded glass bead blasted specimen.

Figure 44, Figure 45, Figure 46, and Figure 47 shows the crack initiation and early crack propagation area of specimens with 1, 4, 12, and 24 h of pre-corrosion, with higher magnification images of the corrosion damage primarily responsible for initiation of the crack resulting in failure. All corroded specimens show crack initiation from multiple areas of corrosion damage along the edge of the fracture surface. The 1, 4, 12, and 24 hours pre-corroded specimens shown had fatigue lives of 82 224, 78 458, 85 771, and 68 449 cycles respectively.

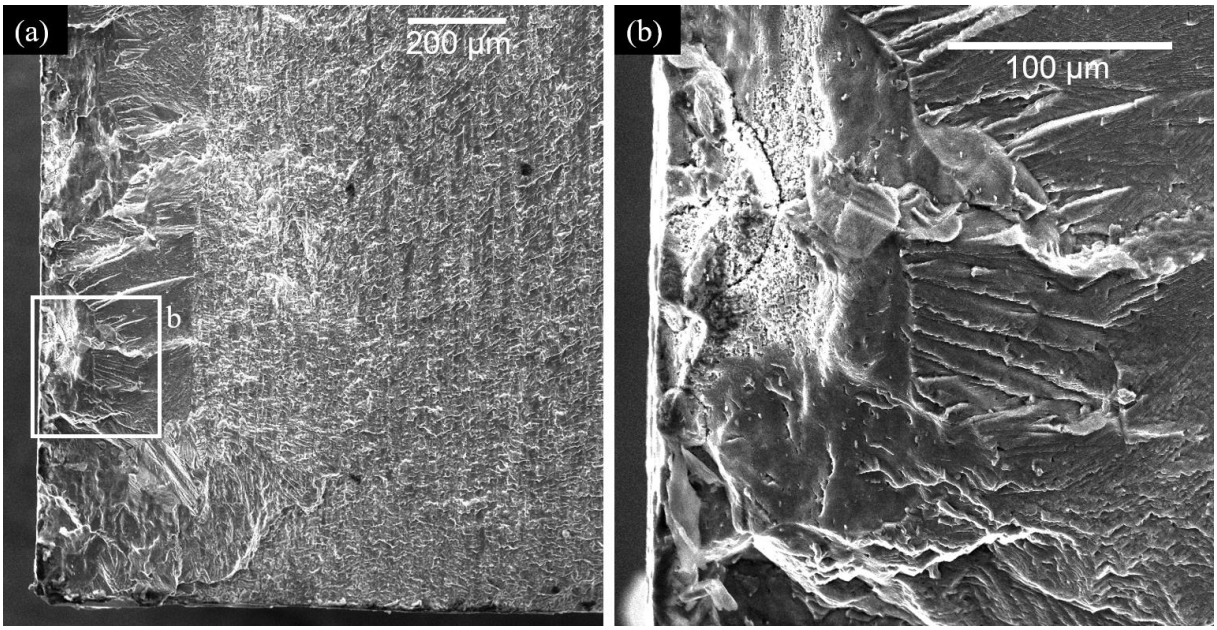

Figure 44: Fracture surface of as extruded specimen with 1 h pre-corrosion.

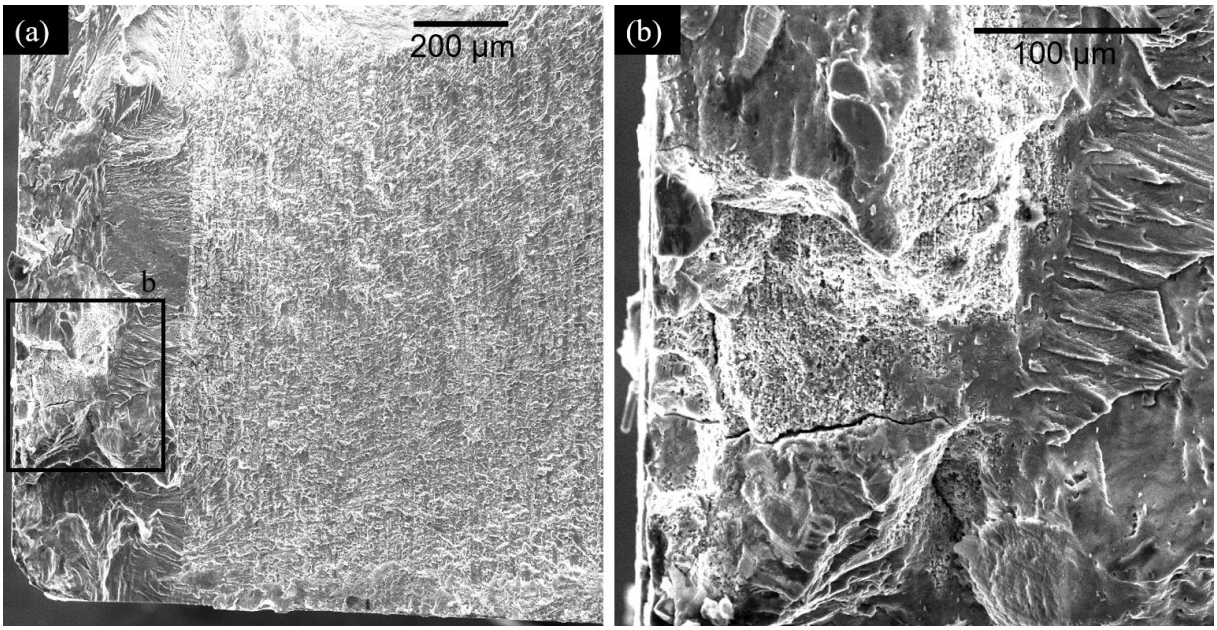

Figure 45: Fracture surface of as extruded specimen with 4 h pre-corrosion.

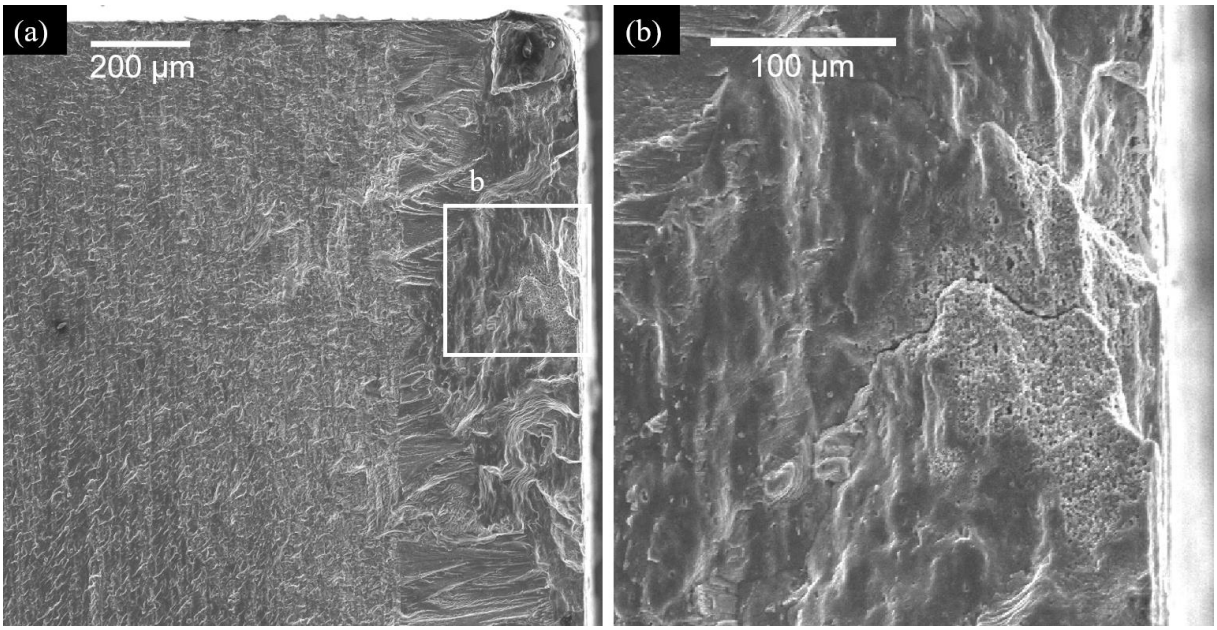

Figure 46: Fracture surface of as extruded specimen with 12 h pre-corrosion.

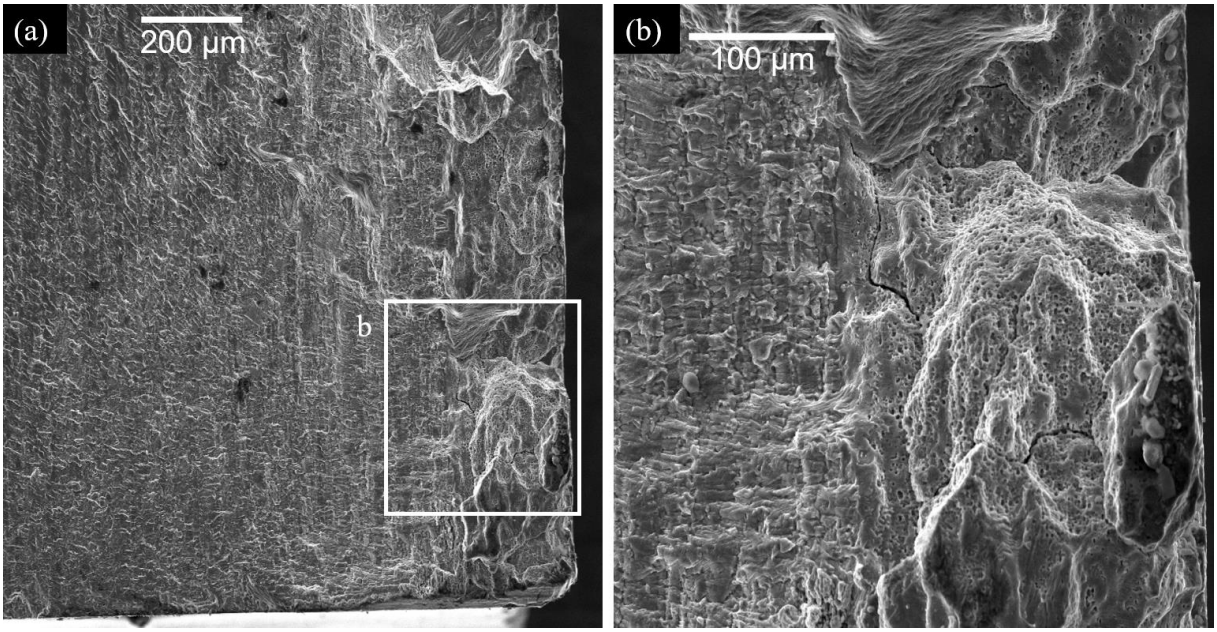

Figure 47: Fracture surface of as extruded specimen with 24 h pre-corrosion.

Figure 48 and Figure 49 shows the crack initiation and early crack propagation area of glass bead blasted specimens with 12 and 24 h pre-corrosion, with higher magnification images of the corrosion damage primarily responsible for initiation of the crack resulting in failure. The 12 and 24 h pre-corroded specimens had fatigue lives of 90 711 and 75 514 cycles respectively.

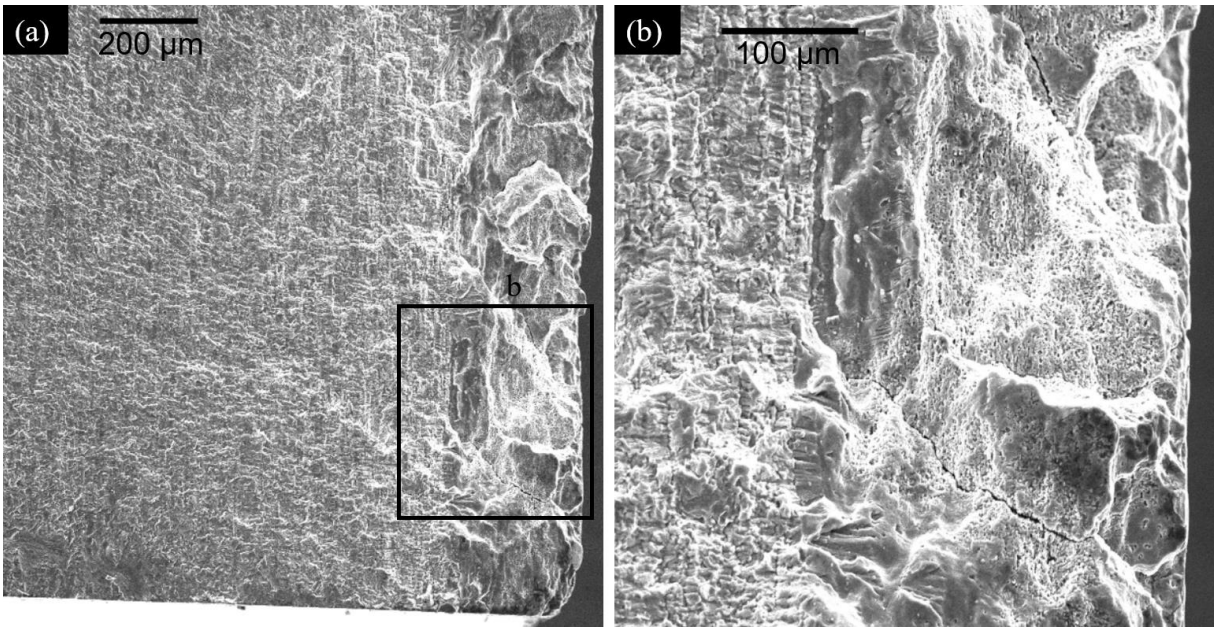

Figure 48: Fracture surface of glass bead blasted specimen with 12 h pre-corrosion.

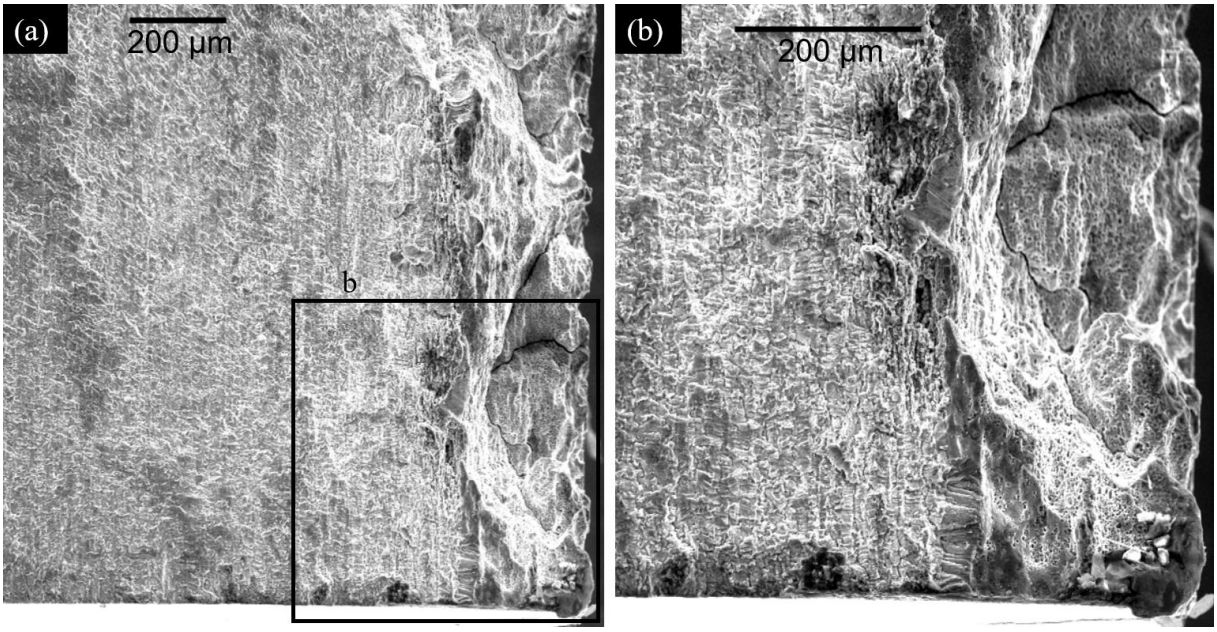

Figure 49: Fracture surface of glass bead blasted specimen with 24 h pre-corrosion.

Surface Features

SEM images using BSE detection of the surface of fatigue specimens were obtained for selected conditions. Figure 50 (a) shows the as extruded surface with 24 h pre-corrosion. Figure 50 (b) shows the uncorroded glass bead blasted surface. Figure 51 shows two areas of the glass bead blasted surface with 24 h pre-corrosion. The images show the cracks left by intergranular corrosion. They also show how the exposed subsurface grains were covered with tiny pits.

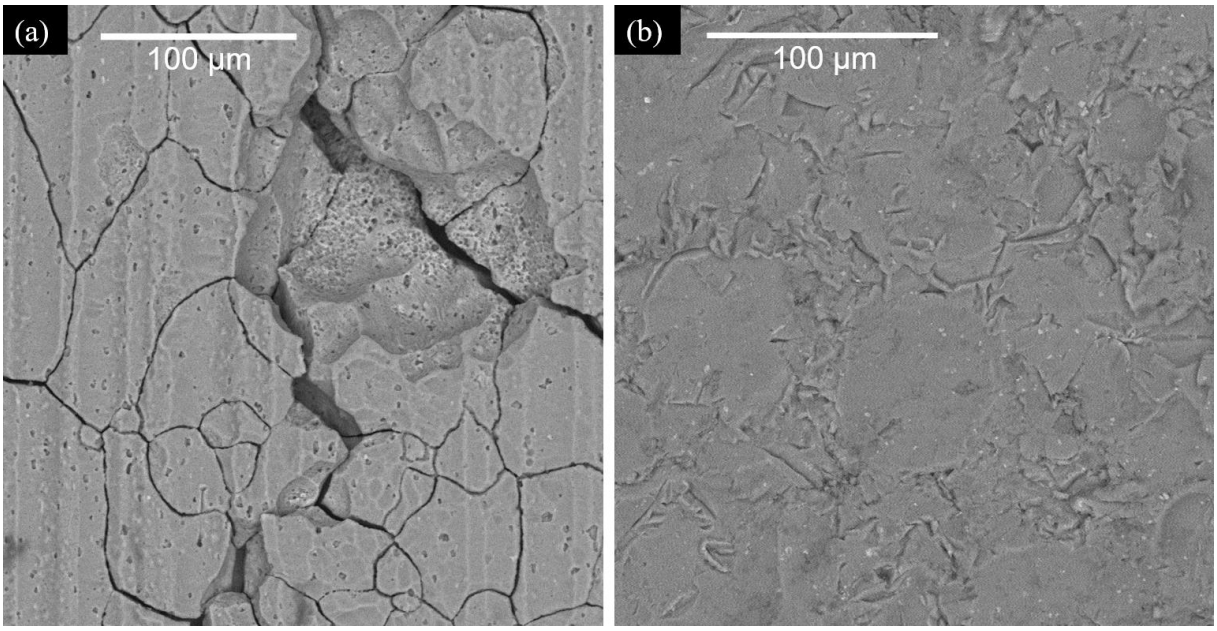

Figure 50: BSE images of fatigue specimen surfaces with 24 h pre-corrosion (a) and uncorroded glass bead blasted (b).

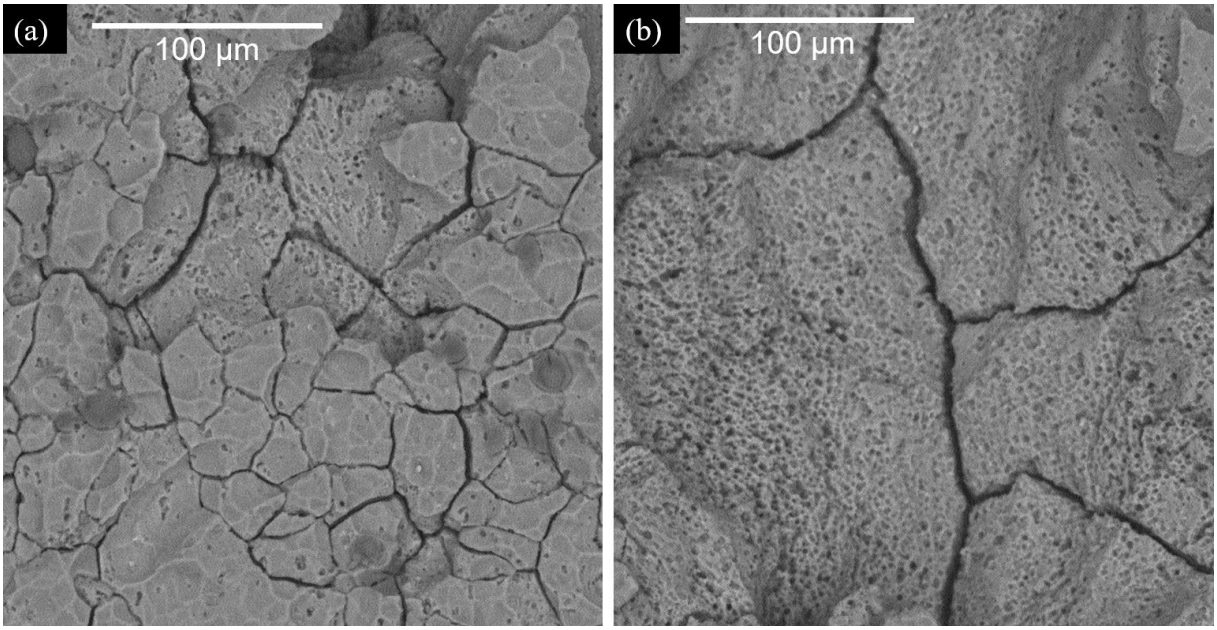

Figure 51: BSE images of fatigue specimen surface with glass bead blasting and 24 h pre-corrosion showing surface grains (a) and subsurface grains (b).

Defect Area Measurement

The defect areas were determined by measuring a smooth shape containing the defect and by measuring the exact area of the defect. Table 27 presents the smooth and exact defect areas for each pre-corroded fatigue specimen.

Table 27: Defect areas for each pre-corroded specimen.

Surface condition	Corrosion duration [h]	Fatigue life [cycles]	Smooth defect area [µm^2]	Exact defect area [µm^2]
As extruded	1	108 237	11 613	10 373
As extruded	1	82 224	20 917	14 066
As extruded	1	91 082	19 558	16 146
As extruded	4	73 121	84 231	62 007
As extruded	4	77 566	62 910	43 979
As extruded	4	78 458	103 614	49 311
As extruded	12	85 771	41 530	28 557
As extruded	12	68 458	114 957	90 300
As extruded	12	83 701	130 206	100 075
As extruded	24	68 449	170 488	142 778
As extruded	24	59 396	292 225	184 870
As extruded	24	71 214	270 292	202 156
GBB	12	89 876	294 381	177 601
GBB	12	80 341	159 821	104 987
GBB	12	90 711	211 670	116 801
GBB	24	66 046	158 165	125 504
GBB	24	77 413	153 044	87 473
GBB	24	75 514	283 078	203 269

Figure 52 shows the selection of defect area for a specimen with a low level of corrosion damage. Local corrosion damage like what is shown in Figure 52 was seen with as extruded specimens with 1, 4, and 12 h of pre-corrosion. For these conditions the area constituting the defect was clearly defined. However, with severely corroded conditions the corrosion damage was continuous along the entire surface. This made it less clear what area constituted the defect. The conditions causing this level of corrosion was as extruded with 24 h pre-corrosion and glass bead blasted with 12 and 24 h pre-corrosion. Figure 53 demonstrates the difficulty in selecting the correct defect area for specimens with severe corrosion damage. With this specimen, widespread corrosion damage was found along the entire surface. As explained in section 3.2.6., the defect area selected was limited to the area of connected corrosion damage contributing to the same crack initiation.

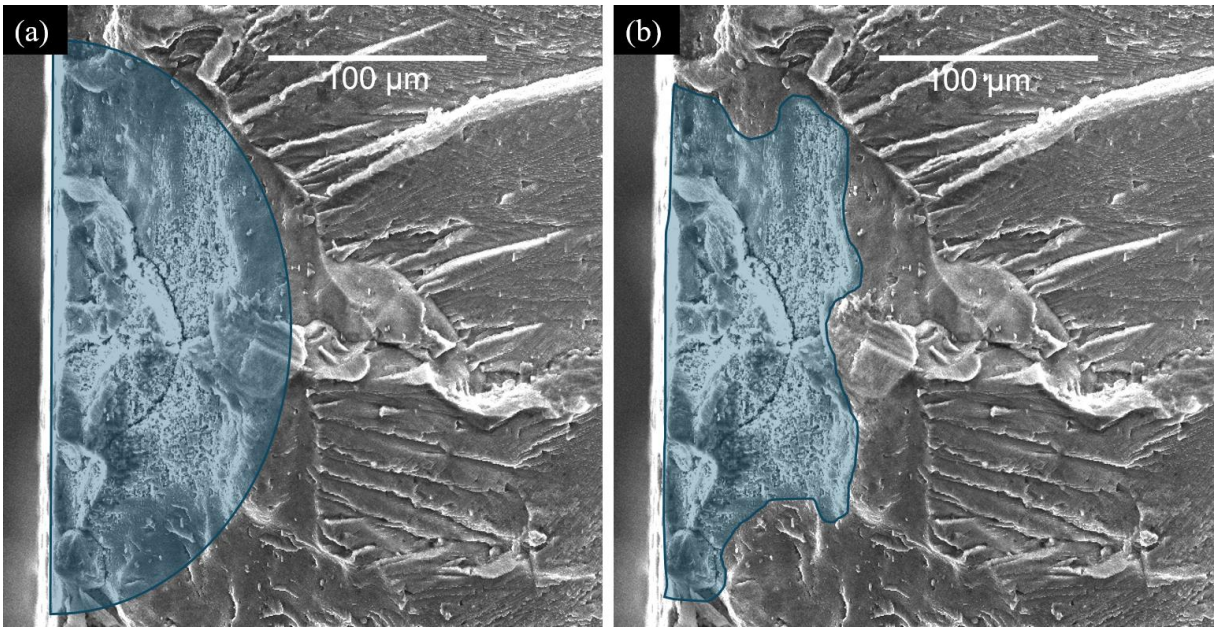

Figure 52: Smooth shape defect area (a) and exact defect area (b) for as extruded specimen with 1 h of pre-corrosion and a fatigue life of 82 224 cycles.

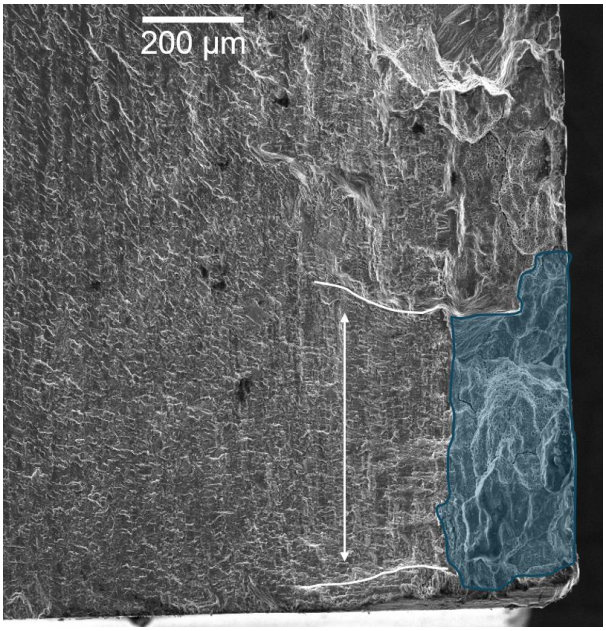

Figure 53: Exact defect area for severely corroded specimen demonstrating the selection of defect area based on connected corrosion damage contributing to the same crack initiation. The specimen shown is the as-extruded specimen with 24 h of pre-corrosion and a fatigue life of 68 449 cycles.

Striation Measurement

Measurement of striation spacing was done on one uncorroded as extruded specimen. Measurements were done at four locations at four distances from the crack initiation point. The results are presented in Table 28.

Table 28: Striation spacing.

Crack length [mm]	A [µm]	B [µm]	C [µm]	D [µm]	Average [µm]
1.864	0.1307	0.1263	0.1217	0.1206	0.1248
2.874	0.3750	0.2204	0.2433	0.3053	0.2860
3.847	0.3949	0.6012	0.5901	0.4393	0.5064
4.862	0.8152	0.8495	0.5843	0.6469	0.7240

Figure 54 shows two examples of how the striation measurements were done. The striations shown in Figure 54 is location D at a crack length of 2.874 mm and location C at a crack length of 3.847 mm.

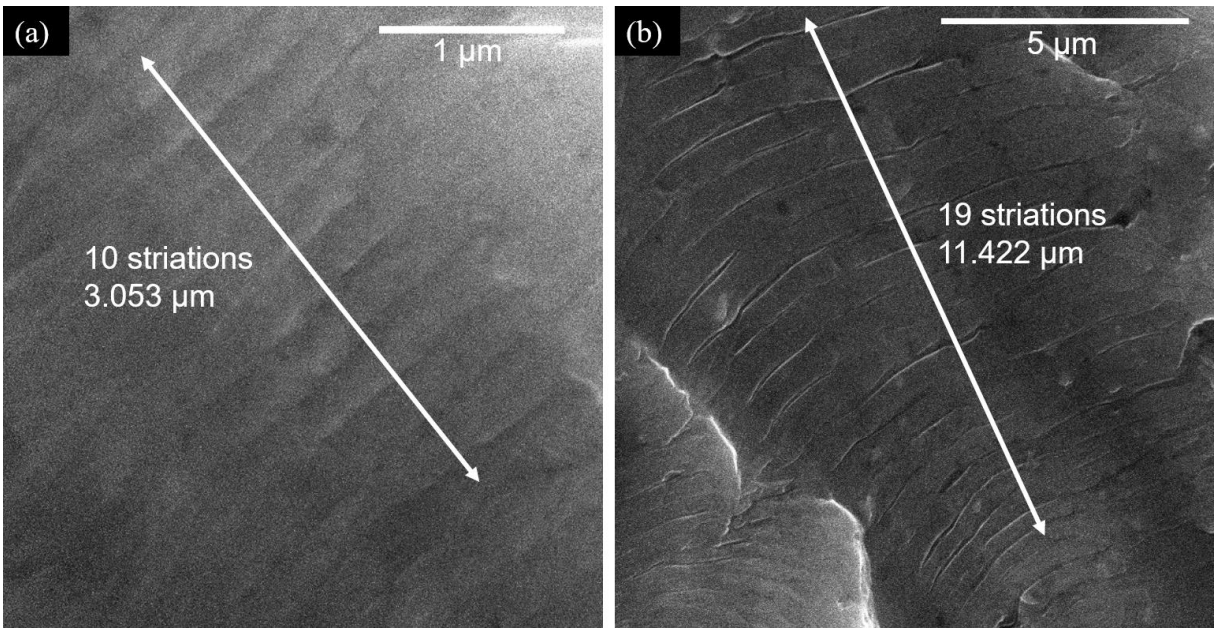

Figure 54: Example of striation measurement. Location D at crack length 2.874 mm (a) and location C at crack length 3.847 mm (b).

5. Discussion

This chapter provides a discussion of and possible explanations for the behavior shown by the results. The discussion of results has been divided into sections covering corrosion damage, fatigue behavior of uncorroded specimens, and fatigue behavior of corroded specimens. Further sections use the results to discuss the application of the root defect area method and to compare experimental results with theoretical crack propagation life estimation. Finally, the results are compared with comparable existing literature.

5.1. Corrosion Damage

5.1.1. Corrosion Form

For both as extruded and glass bead blasted surface conditions the corrosion form experienced by the recycled 6082 alloy was intergranular corrosion. This is clear from the microstructure examination of a pre-corroded cross section as shown in section 4.1. The corrosion form differs from primary 6082 alloys with negligible Cu content, which usually experience pitting corrosion, as explained in theory section 2.2.3. and seen in literature review section 2.4.2. In the recycled alloy the corrosion started at the intersection between the grain boundaries and the surface. Intergranular corrosion then continued to grow along the boundaries through the recrystallized layer into the fine-grained structure in the center of the profile. Past the transition between the recrystallized layer and the fine-grained center, the appearance of the corrosion damage changed substantially. However, in the fine-grained structure the corrosion form also intergranular, and the difference in appearance was a result of the large difference in grain size in the recrystallized and center areas.

The corrosion depth measurements presented in section 4.3. show that corrosion damage is not distributed evenly across the specimen surfaces. The results show that the variation in corrosion depth between the examined areas changed with different corrosion durations. For 1 h pre-corrosion the corrosion damage presented as scattered points of intergranular corrosion with shallow depth. The areas examined on the 1 h pre-corroded specimen were not substantially different from each other in terms of severity of the damage. With 4 h pre-corrosion the damage progressed to much greater depths in a few locations, with most of the surface remaining similar to 1 h pre-corrosion. With 12 h pre-corrosion the distribution was similar to 4 h. However, some more locations started catching up to the maximum corrosion depth. For 24 h pre-corrosion the corrosion depth all areas examined have widespread deep intergranular corrosion, and the variation between each area was small.

As mentioned in theory section 2.2.3. the susceptibility to intergranular corrosion depends on the temper of the alloy. Therefore, adjusting the age hardening process to produce a temper less susceptibility to corrosion could be a possible solution to corrosion problems with recycled alloys in some applications. Deliberate over-aging, also known as stabilization and designated T7, is used as a method for improving corrosion resistance for some high strength treat treatable aluminum alloys susceptible to corrosion, particularly in the 7000-series [49]. This sacrifices some strength for the benefit of considerably increased corrosion resistance.

5.1.2. Influence of Glass Bead Blasting on Corrosion

Corrosion in glass bead blasted specimens was similar in nature to that observed for as extruded specimens, with intergranular corrosion penetrating deep into the material. However, as seen in section 4.3., the corrosion appeared to progress at accelerated rate for glass bead blasted surfaces. With 12 h pre-corrosion the difference between the level of corrosion for as extruded and glass bead blasted was considerable, with the glass bead blasted surface having deeper and more widespread corrosion damage. With 24 h pre-corrosion, the damage is more similar for glass bead blasted and as extruded, although high corrosion depths are even more widespread with glass bead blasting.

5.1.3. Influence of Corrosion on Surface Topography

As seen in section 4.4., surface topography of the as extruded specimens changed considerably with the introduction of corrosion. For the 1, 4, and 12 h pre-corroded the surface became visibly rougher, with the extrusion lines becoming more pronounced as seen in Figure 32. This could be the result of intergranular corrosion causing the surface grains to become loosened from each other, with buildup of corrosion products between them causing them to be moved around slightly. These slight shifts of the grains could manifest at the surface as increased roughness. As the corrosion damage increased to a more advanced level, the surface topography showed large pits. This started in some scattered locations with 12 h pre-corrosion and became more widespread with 24 h pre-corrosion. These pits are most likely not pitting corrosion but the result of intergranular corrosion reaching around the surface grains allowing them to be freed entirely from the surface. Voids in the surface corresponding to missing grains can be also observed in cross section images of corrosion damage in section 4.3. and in the surface BSE images in section 4.6.

A feature observed in both SEM of fracture surfaces and of the corroded surfaces shown in section 4.6. were tiny pits uniformly distributed on the exposed subsurface grain surface after intergranular corrosion. This is likely the result of galvanic corrosion between particles at the surface of the grains and the surrounding aluminum grain. Which particles are responsible for this are not known. One alternative is that these pits are left by corrosion of the grains around cathodic Q-phase particles, which are known to form along the grain boundaries as explained in theory section 2.2.3. Another possibility is Al-Fe intermetallic particles, which are known from microstructure investigations in AluGreen to be prevalent in the microstructure. These small pits are unlikely to influence the fatigue behavior considerably compared with the much larger intergranular corrosion cracks.

For glass bead blasted specimens the surface roughness was reduced from uncorroded to 12 h pre-corrosion. The roughness increased slightly from 12 h to 24 h pre-corrosion. The reduction in surface roughness with initial corrosion could be the result of exposed peaks in the surface topography experiencing more severe corrosion attacks than the valleys, or intergranular corrosion reaching under the peaks and freeing them from the surface.

The surface topography did likely not have a major influence on crack initiation for pre-corroded specimens. With intergranular corrosion, severe corrosion damage is present far beneath the surface. As seen on the fracture surfaces for pre-corroded specimens in section 4.6.,

the fatigue cracks appear to initiate from intergranular corrosion damage far under the surface. The influence of surface topography is therefore likely minimal for pre-corroded conditions with intergranular corrosion.

5.1.4. Influence of Corrosion Duration on Corrosion Depth

Corrosion depth results presented in section 4.3. revealed that the depth of intergranular corrosion did not increase steadily with time exposed to the corrosive environment. Instead, corrosion depth increased rapidly from 0 to 1 and 1 to 4 hours, with very little increase in depth between 4 and 12 hours, before starting to increase substantially again between 12 and 24 hours. The corrosion depth as a function of corrosion duration is shown in Figure 28. There are several possible explanations for this behavior.

One possible explanation is that this is an error caused by a difference in corrosion environment or material between the tests. The material for all specimens was taken from the same profile, so variance in material is unlikely. The main factor in determining the corrosivity of the environment with the accelerated corrosion procedure used was the pH of the solution. Since the pre-corrosion was done in batches and the solutions were prepared separately, there is a possibility that the pH could be different between each batch. However, the pH was measured for all batched tested to be between 0.92 and 0.98. No correlation was found between the pH of each mix and the fatigue lives of the corresponding specimens. Other minor differences, which are unlikely to have such a large effect but cannot be ruled out, are different solution volume in each beaker and differences in specimen preparation procedure.

Another explanation is that the cross sections selected for measuring intergranular corrosion depth were not the most severely corroded areas. Since the intergranular corrosion depth can have large local variation, this could lead to the measured depth not reflecting the actual maximum depth for any given condition. However, the fatigue results presented in section 4.5. show no substantial difference in behavior between the 4 and 12 h corroded specimens. This indicates that these conditions do in fact have similar corrosion damage, making selection of depth measurement areas an unlikely explanation of the differences in observed corrosion rate.

Finally, differences in microstructure are a possible explanation. The grain structure examination shown in section 4.1. showed drastic differences in grain structure from the surface through the recrystallized layer into the center of the specimens. In addition, the hardness measurements presented in section 4.2. also indicate differences in properties as a function of depth from the surface. As discussed in the section 2.2.3. on intergranular corrosion in 6000-series aluminum, corrosion behavior is sensitive to minor changes in microstructure. Therefore, differences in corrosion rate as a function of depth is a reasonable explanation of the variation in corrosion rate observed.

5.2. Fatigue Behavior of Uncorroded Specimens

5.2.1. As Extruded Specimens

Fatigue testing of uncorroded as extruded specimens gave fatigue lives of 153 070, 261 332, and 310 312. The fatigue lives for as extruded specimens had considerable scatter. Since the

lives are well into the HCF regime, most of the fatigue lives consist of the crack initiation phase. Therefore, the fatigue lives will be highly sensitive to imperfections in the surface that can facilitate crack initiation. Large scatter in fatigue lives is therefore not surprising.

Crack initiation in uncorroded as extruded specimens occurred from the front or back face close to the corner, as shown in section 4.6. Due to the specimens being tested perpendicular to the direction of extrusion, the roughness from the extrusion lines will facilitate crack initiation as explained in section 2.3.4. These faces also have a large grained recrystallized layer as shown in section 4.1. The side surfaces of the fatigue specimens had a fine elongated grain structure from the center of the extruded profile. As explained in section 2.3.4. this generally leads to increased resistance to crack initiation. The surface roughness values of the machined side surface were comparable to the extrusion lines with Ra = 0.447 µm compared to Ra = 0.456 µm. However, as seen in Figure 36 in section 4.4. the roughness profile of the extruded surface appears to have some local sharp grooves deeper into the surface, compared with the regular pattern left by each cut of the mill during machining. Overall, it is likely that both the recrystallized layer and the surface topography contributed to reducing the fatigue resistance of the front and back faces compared with the sides.

5.2.2. Glass Bead Blasted Specimens

Glass bead blasting was found to increase the fatigue resistance for uncorroded specimens substantially. For as extruded specimens the fatigue lives of the tested specimens were between 153 070 to 310 312 cycles. Of the glass bead blasted specimens, two had fatigue lives of over $1.1 \cdot 10^6$ cycles, while the last had a substantially lower life of 306 292. This outlier could be the result of inadequate coverage of glass bead blasting. As a fatigue crack will initiate at the weakest location, missing only one small area of the specimen surface with glass bead blasting will reduce the fatigue life of the specimen to the behavior seen without glass bead blasting. This is not unlikely to have happened in this case, as the glass bead blasting was done by hand, as described in section 3.1.2.

Glass bead blasting has three main ways of changing the material that could lead to a change in fatigue behavior. Firstly, glass bead blasting changes the surface topography of the specimen. The confocal microscope examination shown in section 4.4. shows that the glass bead blasted surface is drastically different to the as extruded surface. The extrusion lines have been removed and the surface is instead covered with deep craters from the impacts of the glass beads. In terms of roughness values, they are substantially higher for the glass bead blasted specimens. Increased surface roughness will generally reduce the fatigue life. However, the shape of the roughness is also important to consider. Since the shape of the roughness is so different for glass bead blasted and as extruded surfaces it cannot be conclusively stated if the increased surface roughness will lead to an improvement in fatigue behavior. This means the surface topography of the as extruded specimens could potentially better facilitate initiation of cracks than the glass bead blasted specimens. As explained in section 2.3.4., extrusion lines are known to reduce the fatigue strength of extruded aluminum profiles considerably [32].

Another possible effect of glass bead blasting is that it could change the microstructure close to the surface. However, in this case no identifiable change was found in the grain structure

between the glass bead blasted and as extruded specimens, see section 4.1. Therefore, glass bead blasting influencing the fatigue behavior through a change in microstructure is unlikely to have happened.

Finally, the glass bead blasting could have introduced compressive residual stresses in the material close to the surface of the specimens. Hardness results shown in section 4.2. show an increase in hardness with glass bead blasting. This indicates that the desired effect of introducing compressive residual stresses is likely to have been accomplished. This may have resulted in increased resistance to crack initiation, and to reduced crack propagation rate at the depths where compressive residual stresses were present. Overall, the increase in fatigue resistance of glass bead blasting is likely a result of compressive residual stresses in the material close to the surface, potentially in combination with a surface topography that is less favorable to crack initiation.

As glass bead blasting was done before machining the final fatigue specimen, only the front and back faces of the fatigue specimens are glass bead blasted, see section 3.1.2. However, the fatigue resistance increased drastically even though the sides were not glass bead blasted. This reinforces the previous point that the crack initiation resistance of the surface is reduced compared with the bulk material due to the extrusion lines and recrystallized layer. With glass bead blasting, the crack initiation point appeared to be along the sides close to the corner, as shown in section 4.6. This indicates that the resistance to crack initiation of the glass bead blasted surface was greater than the fine-grained center with a fine machined finish. This supports the idea that compressive residual stresses from glass bead blasting was affecting the crack initiation resistance, as the rough recrystallized surface would likely be more susceptible to crack initiation than the machined fine-grained surface if not for compressive residual stresses.

5.3. Fatigue Behavior of Corroded Specimens

5.3.1. As Extruded Specimens

As shown in section 4.5., fatigue lives were reduced substantially with the introduction of pre-corrosion. The reduction in fatigue life was most substantial between uncorroded and the lowest corrosion condition. The lowest corrosion condition was 1 h immersion and resulted in a maximum corrosion depth of 112 µm. This reduced the average fatigue life from 241 571 for uncorroded specimens to 93 848. The difference in fatigue life between each level of pre-corrosion was less substantial than between uncorroded specimens and corroded specimens. This is the same behavior seen in literature, see section 2.4.4. For a maximum corrosion depth of 112 µm the average fatigue life was 93 848, and with an increase in corrosion depth to 424 µm the average fatigue life was reduced to 66 353. This could indicate that the crack initiation is not a large proportion of the fatigue life for pre-corroded specimens, with the fatigue life being reduced to being made up of mostly crack propagation life, where the difference in corrosion depth affects the fatigue life through determining the initial crack depth.

SEM images presented in section 4.6. show that fatigue cracks in pre-corroded specimens initiated from depth of the intergranular corrosion under the surface, rather than from the

surface. This was true for all pre-corroded specimens. The sharp intergranular corrosion likely led to a large increase in stresses at the tips, facilitating crack initiation. Many sites of crack initiation were found from locations of corrosion damage along the crack growth area edge. The failure was likely driven by a main fatigue crack which started propagating from one of the most severe sites of corrosion damage, with other cracks joining up with the main crack once it had advanced far enough. The SEM images also showed that the crack growth areas for some pre-corroded specimens had large skips up and down in height along the edge. This likely corresponds with where different crack initiation sites joined up diagonally as the main fatigue crack propagated.

The fatigue results presented in section 4.5. shows that fatigue lives were substantially reduced by all the levels of pre-corroded tested. However, with the lower levels of pre-corrosion tested, the corrosion damage was not visible to the naked eye. Due to the corrosion form in the recycled alloy being intergranular corrosion, the corrosion damage was not visible until it had advanced to a state where surface grains were freed from the surface, as shown in section 4.4. This means that the fatigue behavior of the recycled alloy was drastically reduced from corrosion well before the corrosion was visible on the surface. This should be carefully considered in possible applications of this alloy, with service and inspection plans accounting for this behavior.

Another important difference between the uncorroded and corroded results is the reduction in scatter for pre-corroded specimens. This is also indicative of a fatigue life consisting mostly of crack propagation, as the crack propagation life for a given initial crack depth would be consistent for all specimens, as variation fatigue life at the same loading conditions is primarily caused by the variation in initiation life. With the initiation life being a small proportion of the total fatigue life, the variation in initiation life does not lead to as much scatter in the total fatigue life.

5.3.2. Glass Bead Blasted Specimens

Glass bead blasted specimens with pre-corrosion also saw a drastic reduction in fatigue life compared to the uncorroded results, see section 4.5. As shown in section 5.2.2, the glass bead blasted specimens showed a substantially increased fatigue resistance compared to as extruded surface condition uncorroded. With the introduction of corrosion, the glass blead blasted specimens also had longer fatigue lives than the as extruded specimens. However, this difference was much less substantial. The improved pre-corroded fatigue life of glass bead blasted specimens can be attributed to introduction of compressive residual stresses close to the surface, as the changes in surface topography was unlikely to have a considerable influence on fatigue life with widespread intergranular corrosion deep below the surface, see section 5.1.3. This further supports the idea that compressive residual stresses have been introduced by glass bead blasting, and that these are associated with increased fatigue resistance both for uncorroded and pre-corroded specimens.

As shown in section 4.3., as extruded and glass bead blasted specimens with 24 h pre-corrosion had similar corrosion depth. The glass bead blasted specimens had slightly longer fatigue lives than the as extruded at this corrosion duration, as seen in section 4.5. However, at 12 h pre-corrosion the glass bead blasted specimens had more severe corrosion damage, but still had a

longer fatigue life than the as extruded specimens. This can be attributed to higher compressive residual stresses from glass bead blasting closer to the surface. For even lower corrosion depths, the improvement in fatigue life with glass bead blasting could be much more substantial. However, this was not tested as part of the scope of this project.

The SEM images of the fracture surface of glass bead blasted specimens with pre-corrosion are similar to those for as extruded specimens. This is shown in section 4.6. The fatigue cracks initiated from the depth of the intergranular corrosion damage far below the surface. The mechanisms involved in fatigue failure appeared to be the same, the only difference being that the compressive residual stresses slowed crack initiation and early propagation causing slightly longer fatigue lives.

5.4. Fatigue Life as Function of Defect Area

The root area method can be used to describe the fatigue behavior of materials with known defects. With this method, fatigue life is related to the initial stress intensity factor from the combination of loading and defect area, as explained in section 2.3.3. This was done for all fatigue specimens tested with pre-corrosion. The method and results for defect area measurements are described in sections 3.2.6. and 4.6, respectively. The initial stress intensity factor was calculated from the applied stress range, 162 MPa, and defect area according to Equation 9 [25].

$$K_{max} = 0.65\sigma_{max}\sqrt{\pi\sqrt{area}} \tag{9}$$

Figure 55 shows the relation of initial stress intensity factors to fatigue lives with defect areas calculated from a smooth shape containing the defect from corrosion damage for as extruded specimens. Figure 56 shows the relation of initial stress intensity factors to fatigue lives with defect areas calculated with the defect area as the exact corrosion damage shape for as extruded specimens. The equations for the regression lines are shown in Table 29. Note that the data and regression was calculated for K_{max} at $R = 0.1$. A correlation is observed between the initial stress intensity factor and fatigue life for the as extruded specimens. However, there is large amount of scatter in the data. Calculating the defect area with a smooth shape containing the defect and the exact corroded area appears to have similar correlation with fatigue life in this case.

Table 29: Regression for K_{max}-N data for smooth and exact defect area.

Defect area	Regression equation
Smooth defect area	$K_{max} = 4.161 \cdot 10^7 \text{MPa} \cdot {N_f}^{-1.449}$
Exact defect area	$K_{max} = 1.568 \cdot 10^7 \text{MPa} \cdot {N_f}^{-1.369}$

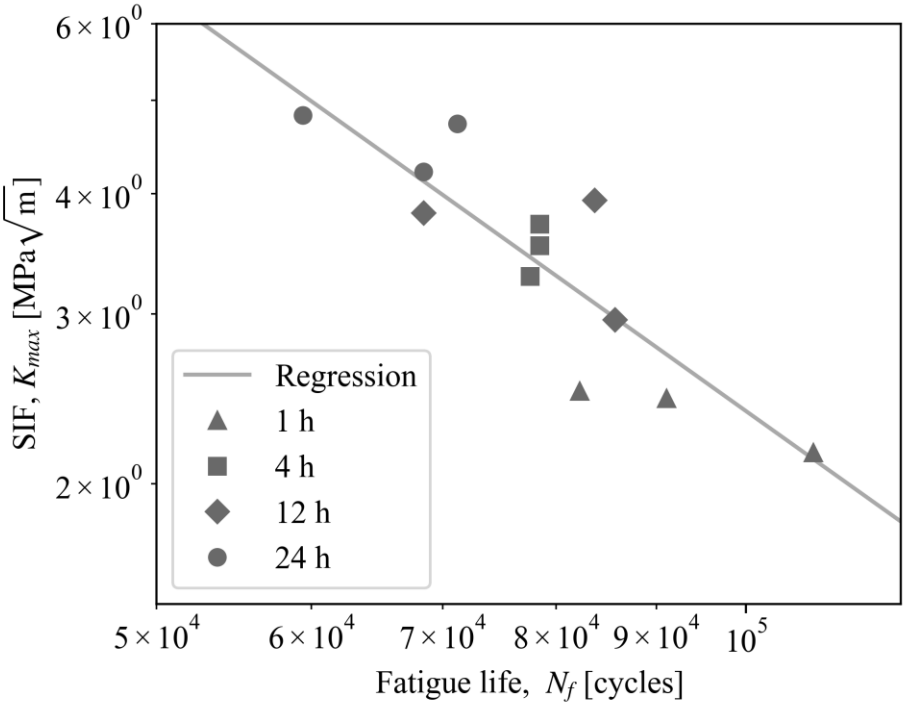

Figure 55: K_{max}-N data for smooth defect area of as extruded specimens.

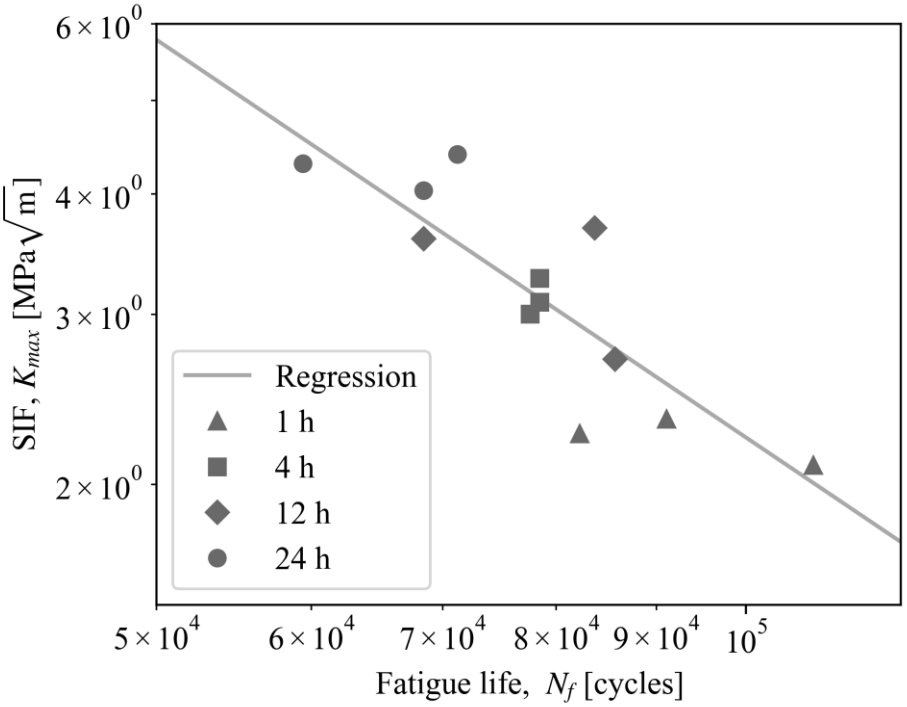

Figure 56: K_{max}-N data for exact defect area of as extruded specimens.

As mentioned in section 4.6., the defect area responsible for crack initiation is clear for conditions with local corrosion damage, as the defects are separate from each other. For the 24 h pre-corroded specimens however, the corrosion is widespread along the entire surface. This made determining what should be included in the defect area open to interpretation. As mentioned in section 3.2.6, this was done here by selecting the area with connected corrosion

that contributed to the same crack initiation, as shown in Figure 53 in section 4.6. In addition to making the selection of defect area less reliable for heavily corroded specimens, the widespread corrosion could also have resulted in more complex interaction between the corrosion damage in nearby areas in crack initiation.

Figure 57 shows the relation of initial stress intensity factors to fatigue lives with defect areas calculated from a smooth shaped defect area containing the corrosion damage for glass bead blasted specimens. In this data, there is no identifiable correlation between initial stress intensity factor and fatigue life. This is likely a combination of several factors. Firstly, all pre-corroded glass bead blasted specimens had widespread intergranular corrosion covering the entire surface. Therefore, it is not as clear from SEM images what area constitutes the defect responsible for crack initiation compared to the conditions with localized corrosion attacks. Secondly, the widespread corrosion likely means that several areas of corrosion are interacting in a complex way to initiate fatigue, rather than once singular defect acting alone. This is not accounted for in the method used for calculating the stress intensity factor. Finally, the glass bead blasted specimens have compressive residual stresses influencing crack imitation and propagation. As explained in section 5.3.2., this has likely led to higher increase in resistance to crack initiation with the slightly lower corrosion depth for specimens with 12 h pre-corrosion compared to 24 h pre-corrosion. This could have resulted in disproportionately long life with 12 h pre-corrosion, even though the stress intensity factor from nominal stress and defect areas are similar for 12 and 24 h pre-corrosion.

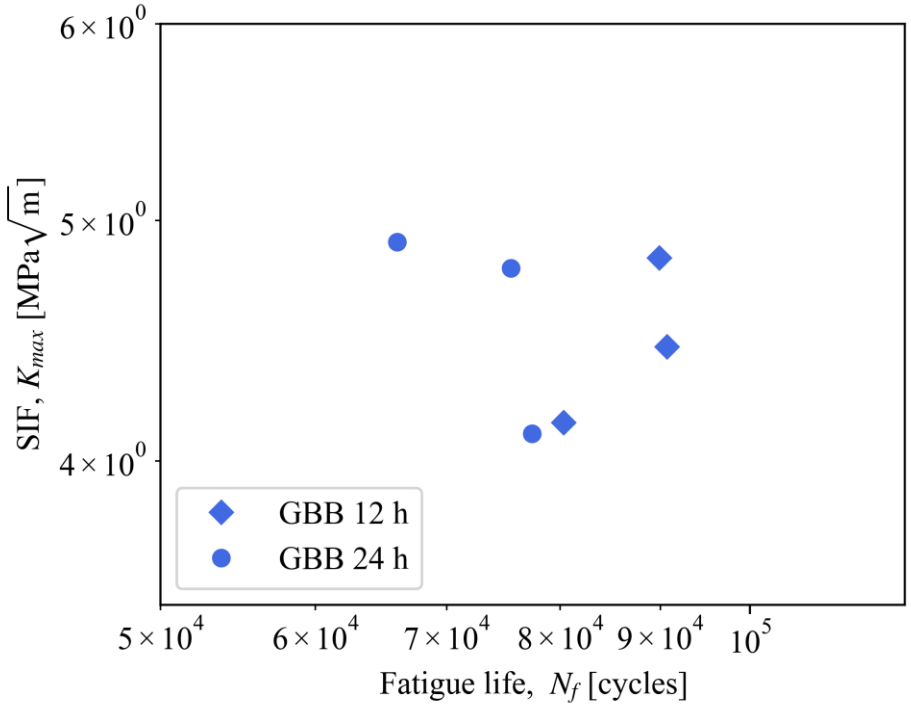

Figure 57: K_{max}-N data for smooth defect area of glass bead blasted specimens.

The square root of defect area method appears to be applicable to fatigue specimens with local intergranular corrosion damage and no surface treatment affecting crack initiation. For more severely corroded specimens the approach to calculating defect area used in this thesis did not

provide very reliable results. Other approaches to determining the defect area could be more accurate, such as the defect area approximation for shallow and wide surface defects calculated only from depth described by Murakami [25].

5.5. Crack Propagation Life

To better understand the influence of the damage from pre-corrosion on the crack initiation phase, the experimental data was compared to theoretical crack propagation lives resulting from ideal initial cracks of similar size. This comparison was only done for as extruded specimens. The difference in theoretical crack propagation life and experimental fatigue life for a given defect size can give an indication of how the fatigue life is distributed between the crack initiation and propagation phases for pre-corroded specimens. In addition, it can provide insight into what equivalent initial crack length represents intergranular corrosion with different depths and/or defect areas. The fatigue crack growth approach to estimating fatigue life for pre-corroded specimens with initial cracks representing the corrosion damage has been shown to correspond well with experimental data [45, 50].

Crack propagation life from an initial to a final crack length can be calculated based on the Paris law as described in section 2.3.3. For this, the Paris law coefficients, C and m, must be determined. This was done by using the striation spacing measured at different crack lengths with SEM. The striation spacing corresponds with the fatigue crack growth per cycle. The striation data was only obtained for one uncorroded specimen, as crack growth rate is a function of the bulk material properties and will not be affected by pre-corrosion of the surface. The corresponding ΔK for each crack length was calculated from the crack length and the applied stress range.

$$\Delta K = F\Delta\sigma\sqrt{\pi a} \tag{10}$$

As the striation spacing was measured for large crack lengths relative to the size of the cross section, the variation in the geometric factor F must be accounted for. An approximate value of F corresponding each crack length was determined from the results of simulations done by Toribio *et al.* [51] on geometric factors for stress intensity factor for corner cracked specimens with a rectangular cross section. The geometry closest resembling that of crack growth seen with the fatigue specimen was that of a crack length in the thickness direction being half the crack length in the specimen's width direction. This gave the values for F and ΔK for the applied stress range 162 MPa presented in

Table 30. The crack growth rate curve is shown in Figure 58. The Paris law coefficients were determined with regression analysis to be $C = 4.9138 \cdot 10^{-10}$ (m/cycle)/(MPa·m$^{0.5}$)^m and $m = 2.3269$. As described in section 2.3.3., m can be considered independent of stress ratio while C depends on stress ratio. In this case the C determined from the striation measurement was C for $R = 0.1$. As a result, this C can be applied directly to estimating crack propagation life at $R = 0.1$.

Table 30: Stress intensity factors at striation measurement crack lengths.

Crack length [mm]	**Crack growth rate [µm/cycle]**	***F***	***ΔK* [MPa·m$^{0.5}$]**
1.8642	0.1248	0.8985	11.139
2.8743	0.2860	0.9709	14.945
3.8475	0.5064	1.0665	18.994
4.8625	0.7240	1.1932	23.891

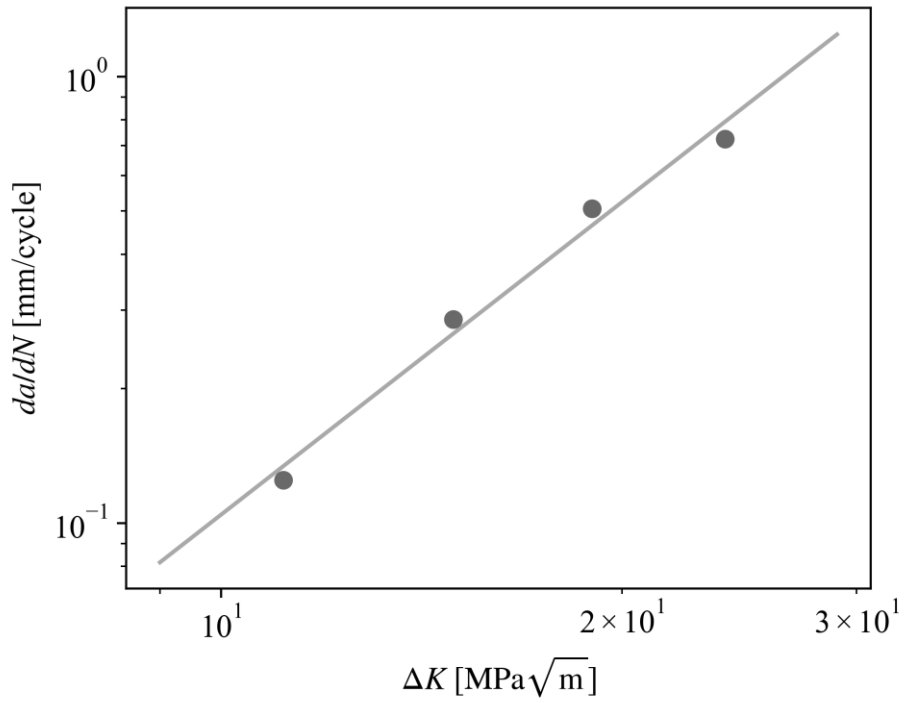

Figure 58: Crack growth rate as function of stress intensity factor range.

The final crack length is a result of the reduction in cross section required for static overload of the remaining area. Final crack length will therefore be approximately the same for all specimens with the same geometry and tensile properties tested under the same loading conditions. As the tensile properties of the material will not be considerably affected by corrosion, final crack length was assumed not to be affected by corrosion. This was confirmed by measuring final crack length for uncorroded and corroded specimens. From SEM images of the fracture surfaces, the final crack lengths were found to be between 5.6 and 5.8 mm. As the loading cycles close to final failure have a high crack growth rate compared to most of the crack propagation life, they make up a small proportion of the crack propagation life and the precise final crack length therefore only has a marginal impact on life. A final crack length of 5.7 mm was used in calculating crack propagation life.

The total crack propagation life can be calculated from an initial crack length accounting for a changing geometric factor by adding up the crack growth from each loading cycle and counting the total cycled required to reach the final crack length. From this, the theoretical crack propagation life as a function of initial crack length was determined. Figure 59 shows the

theoretical crack propagation life with initial crack lengths from 0.05 to 0.5 mm plotted against experimental results in terms of average life to maximum measured intergranular corrosion depth and individual specimen life to square root of their respective defect areas.

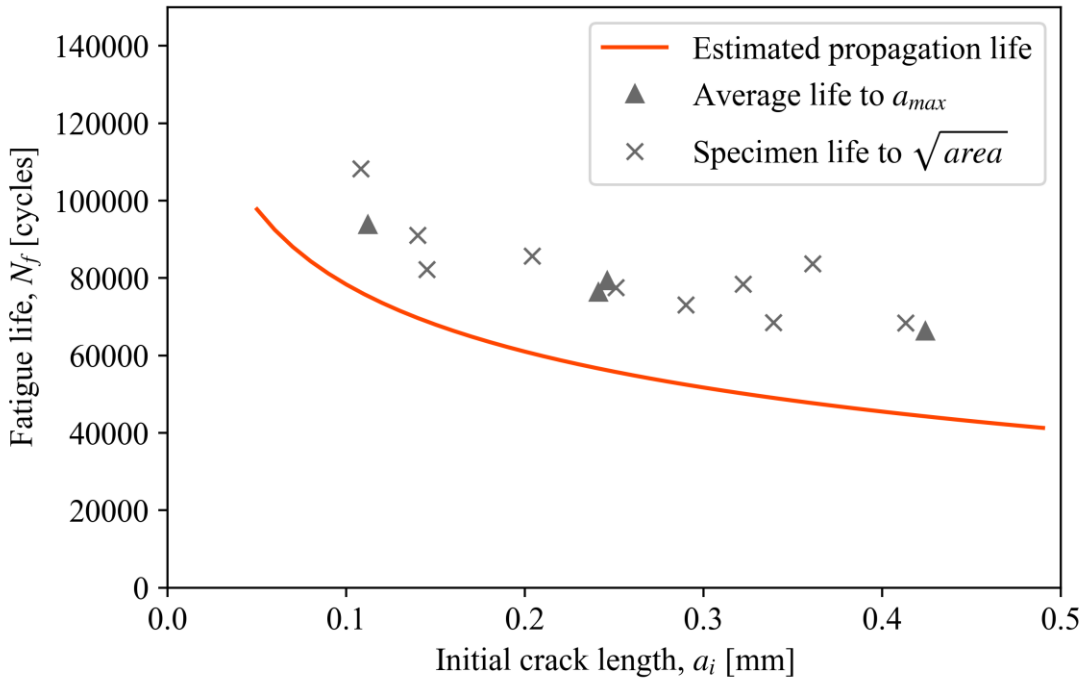

Figure 59: Comparison of theoretical crack propagation life and experimental results.

The theoretical crack propagation life curve follows slightly under the experimental data. This indicates that the crack initiation phase is short for pre-corroded specimens and that stable crack propagation makes up most of the fatigue life. As the difference in fatigue life between the experimental data and crack propagation life corresponds with crack initiation life, the difference would be expected to decrease with increasing corrosion damage. However, the difference appears to remain roughly constant for all experimental data. One possible explanation for this is that the Paris law coefficients have not been determined accurately enough to provide an estimation of the crack propagation life accurate enough to show this effect. This is likely due to the assumptions and approximations used in determining the geometric factor F for each crack length. Another possible explanation is that the equivalent crack depth is not the same as intergranular corrosion depth or defect area. In comparing the experimental life and the propagation life estimation, the corrosion damage is assumed to act as a single defect. However, as corrosion progresses with longer corrosion duration the intergranular corrosion becomes far more widespread on the surface. This could have caused the effective crack length, representing the difference from the general corrosion depth to the maximum, to be lower than the measured maximum corrosion depth. This conceptual framework also entails a reduction in effective load bearing area. Although this increases the effective alternating stress on the load bearing cross section, the reduction in effective initial crack length likely reduces the initial stress intensity factor resulting in a longer fatigue life.

5.6. Comparison with Literature

As described in the literature review section, section 2.4., the existing literature on pre-corroded fatigue of 6000-series aluminum covers different alloys and corrosion conditions. Both Abdulstaar *et al.* [36] and Munõz *et al.* [38] tested 6082-T6 alloys. However, as Abdulstaar *et al.* used different corrosion conditions and did not provide any quantification of the resulting corrosion damage, comparison with this study is not meaningful. The results from Munõz *et al.* are therefore the most meaningful for comparison as this study provided detailed quantification on corrosion damage, and also used the same loading conditions of axial loading at $R = 0.1$.

Figure 60 compares experimental results from this thesis with results obtained by Munõz *et al.* on fatigue life as a function of maximum corrosion depth. The stress level for each curve is maximum cyclic stress, σ_{max}. All data points for Munõz *et al.* represent experimental data except for σ_{max} = 180 MPa, which was calculated for comparison with the results of this thesis from the Basquin law coefficients the paper provided for each corrosion level. The same is true for all data points for the most severe corrosion level, as this condition was tested at slightly different stress levels than the other conditions.

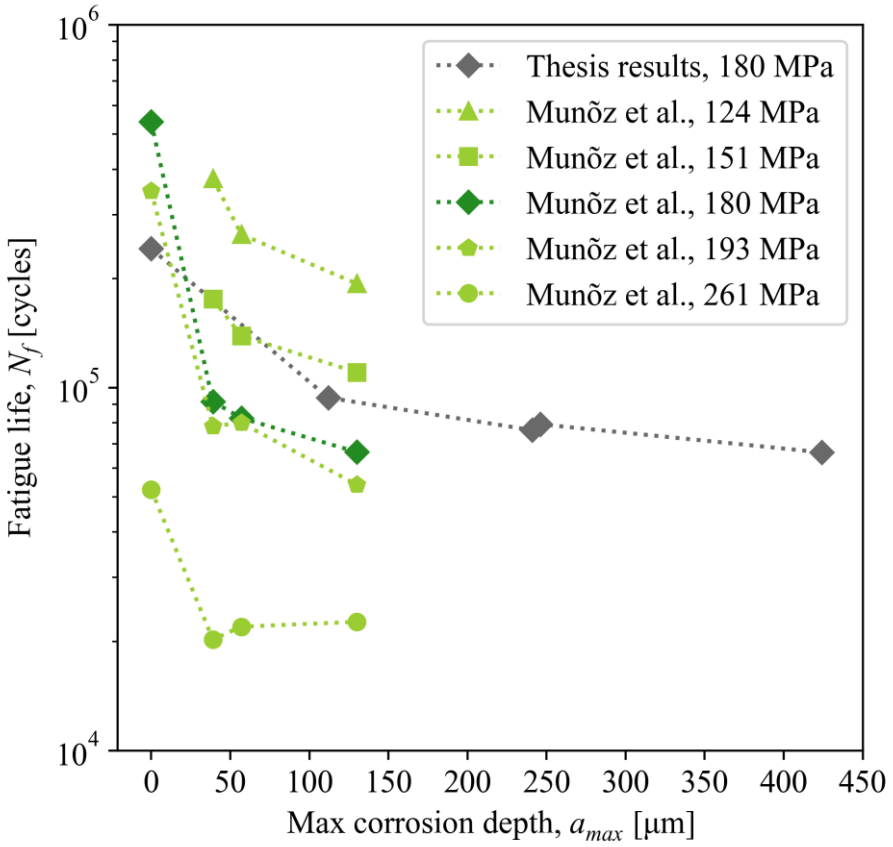

Figure 60: Comparison of experimental results in this thesis with results obtained by Munõz *et al.* [38]. Stresses are maximum cyclic stress (σ_{max}) at $R = 0.1$.

The comparison shows that the uncorroded fatigue lives were shorter in the results of this thesis than those obtained by Munõz *et al.*, 241 571 compared to 540 616 cycles. There are several possible explanations for this. Firstly, differences in surface topography of the specimens tested in this thesis and those tested by Munõz *et al.* may have influenced crack initiation differently.

The fatigue specimens tested by Munõz *et al.* were extracted from a rolled sheet in the rolling direction, while the fatigue specimens in this thesis were extracted from an extruded profile perpendicular to the extrusion direction. Secondly, the presence of a recrystallized layer of the specimens tested in this thesis likely reduced the resistance to crack initiation. No information is provided on the microstructure of the material used by Munõz *et al.* Finally, the impurities in the recycled alloy tested in this thesis could have reduced the fatigue resistance. No information is provided on the precise chemical composition in Munõz *et al.*

For pre-corroded specimens, the fatigue results in this thesis show longer fatigue lives at similar corrosion depths. There are several possible explanations to this. Firstly, intergranular corrosion could be less damaging to fatigue behavior than pitting corrosion of the same depth, contrary to what would be expected for sharper defects [15]. Another possible explanation is that chemical composition, microstructure, or other factors make the alloy tested in this thesis more resistant to crack propagation or crack initiation from defects. Note that the recycled alloy has a tensile strength than the alloy tested by Munõz *et al.* Finally, as crack propagation likely makes up a large proportion of fatigue life for pre-corroded specimens, the differences in geometry of the specimens could also impact the fatigue life. Specimens tested by Munõz *et al.* had a thickness of 2 mm, while the specimens in this thesis had a thickness of 6 mm.

Overall, the results of this thesis and Munõz *et al.* were similar in terms of fatigue life and response the pre-corrosion, even though the alloys tested experienced different corrosion forms. This indicates that the influence of intergranular corrosion on fatigue life of 6082 alloys is likely not very different to that of pitting corrosion of similar depth. It also indicates that the impurities in the recycled 6082 alloy likely do not influence the fatigue lives resulting from similar levels of corrosion drastically. However, the two mentioned points are speculative and would require more comparative data to confirm.

6. Conclusion

In this thesis the influence of prior corrosion on fatigue behavior of recycled aluminum was investigated through high cycle fatigue testing of pre-corroded specimens of a 6082 aluminum alloy with a chemical composition representing a recycled alloy. The fatigue lives of different levels of pre-corrosion were compared with those of uncorroded specimens. The viability of glass bead blasting as a method of improving pre-corroded fatigue behavior was also investigated.

The main conclusions drawn from the work described in this thesis are:

- The recycled 6082 alloy was shown to experience intergranular corrosion as opposed to pitting corrosion usually observed for 6082 alloys. This is a result of impurity elements found in the recycled alloy, with the presence of Cu on grain boundaries likely being the main factor.
- Prior corrosion led to a substantial reduction in fatigue life. This was due to intergranular corrosion damage facilitating the initiation of fatigue cracks.
- The difference in fatigue life between the different corrosion levels tested was not as substantial as the difference from uncorroded to the lowest level of corrosion. This was likely due to a substantial reduction in crack initiation life, leading to crack propagation representing a large proportion of the fatigue lives of pre-corroded specimens. Crack propagation life does not change as substantially with different initial defect size as crack initiation life.
- Intergranular corrosion can have a substantial influence on fatigue behavior without being clearly visible on the surface. This should be carefully considered in applications of recycled alloys susceptible to intergranular corrosion.
- Glass bead blasting can lead to a substantial improvement in fatigue behavior for the recycled 6082 alloy in uncorroded condition. This is likely due to introduction of compressive residual stresses close to the surface. However, the improvement in fatigue behavior with pre-corrosion was not substantial enough for glass bead blasting to be a viable method of improving the pre-corroded fatigue behavior for the corrosion levels tested.
- The root area method, relating initial stress intensity factor (K_{max}) to fatigue life (N_f), appears to be applicable to pre-corroded specimens with local corrosion damage.
- Comparison with a similar study conducted on a non-recycled 6082 alloy indicated that, despite the different corrosion form, the fatigue behavior was comparable for the two alloys at similar levels of corrosion damage.

Suggestions for future work:

- Fatigue testing of pre-corroded specimens at different loading conditions, such as different stress levels and stress ratios, could allow for a more comprehensive understanding of the influence of pre-corrosion on fatigue. This would, amongst other things, allow the fatigue limit to be determined with different levels of corrosion damage, which would be highly useful in design against fatigue in corrosive

environments. In addition, it would allow for determining whether the relationship between initial K_{max} and N_f established for varying defect sizes remains consistent when varying the applied stress level.

- Corrosion testing of the recycled alloy variants in realistic environments would allow for determining what level of corrosion damage can be expected from service in different environments. From this it can be decided which levels of corrosion damage should be tested in fatigue to determine pre-corroded fatigue behavior in realistic environments.
- Fatigue testing of pre-corroded specimens with lower levels of corrosion damage. This would allow for determining what level of corrosion damage is necessary to affect fatigue considerably. It would also reveal the nature of transition from uncorroded to corroded fatigue behavior, in terms of abruptness and scatter in results in the transition area.
- Fatigue testing of pre-corroded specimens with varying impurity content. Fatigue testing of GA1 and GA2 would allow for comparison of fatigue behavior with comparable corrosion levels in these alloys. From this it could be determined whether the influence of impurity content on pre-corroded fatigue is primarily through affecting corrosion resistance, or whether the different impurity levels also influence crack initiation resistance and crack growth rate with the same level of corrosion damage. Together with fatigue tests at low corrosion levels, any difference in threshold corrosion level for influencing fatigue behavior could also be identified.
- Testing the recycled alloy with other tempers than T6, such as T7, to assess whether this can reduce the susceptibility to corrosion, thus improving pre-corroded fatigue behavior.
- Fatigue testing of glass bead blasted specimens with lower levels of corrosion damage and associated corrosion testing in realistic environments could determine whether glass bead blasting is a viable method for improving pre-corroded fatigue behavior in mild corrosive environments.
- Corrosion-fatigue testing to assess the influence of the impurities from recycling on corrosion-fatigue. Due to the impurities in the recycled alloy making it more susceptible to corrosion, corrosion-fatigue will likely also occur in less corrosive environments and at higher loading frequency than would be required for an alloy without these impurities.

7. References

[1] S. Capuzzi and G. Timelli, "Preparation and Melting of Scrap in Aluminum Recycling: A Review," *Metals,* vol. 8, no. 4, 2018, Art no. 249, doi: https://doi.org/10.3390/met8040249.

[2] Hydro. "Hydro og samarbeidspartnerne tildelt 76,9 millioner kroner til grønn aluminiumplattform." https://www.hydro.com/no-NO/media/news/2021/hydro-og-samarbeidspartnerne-tildelt-76-millioner-kroner-til-gronn-aluminiumplattform/ (accessed May 2024).

[3] SINTEF. "AluGreen - Aluminium Green Platform." https://www.sintef.no/prosjekter/2021/alugreen/ (accessed May 2024).

[4] D. R. Askeland, P. P. Fulay, and W. J. Wright, "Nonferrous Alloys," in *The Science and Engineering of Materials SI*, Sixth ed. USA: Cengage Learning, 2011, pp. 539-569.

[5] J. G. Kaufman, "Aluminum Alloy and Temper Desigation Systems of the Aluminum Association," in *Introduction to Aluminum Alloys and Tempers*. USA: ASM International, 2000, pp. 39-76.

[6] J. G. Kaufman, "Applications of Aluminum Alloys and Tempers," in *Introduction to Aluminum Alloys and Tempers*. USA: ASM International, 2000, pp. 87-118.

[7] J. K. Solberg, "Aluminium og aluminiumslegeringer," in *Teknologiske metaller og legeringer*. Norway: Metallurgisk institutt, NTNU, 1999, pp. 182-232.

[8] Hydro, "Technical datasheet - Extruded products, Alloy EN AW-6082," Hydro Innovation & Technology, Sweden, 2019. [Online]. Available: https://www.hydro.com/Document/Doc/Hydro%20EN%20AW%206082.PDF?docId=7324

[9] *EN 573-3: Aluminium and aluminium alloys - Chemical composition and form of wrought products*, E. Standard, 2007.

[10] S. K. Das, "Emerging Trends in Aluminum Recycling: Reasons and Responses," in *Light Metals 2006*, USA, T. J. Galloway, Ed., 2006: TMS (The Minerals, Metals & Materials Society).

[11] A. Sarkar, N. Razavi, G. Ringen, and T. Welo, "Assessing the fatigue behaviour of recycled Al-alloys: A critical review," *Materialia,* vol. 32, 2023, Art no. 101938, doi: https://doi.org/10.1016/j.mtla.2023.101938.

[12] G. Gaustad, G. Olivetti, and R. Kirchain, "Improving aluminum recycling: A survey of sorting and impurity removal technologies," *Resources, Conservation and Recycling,* vol. 58, pp. 79-87, 2012, doi: https://doi.org/10.1016/j.resconrec.2011.10.010.

[13] E. Bardal, "Ulike korrosjonsformer ordna etter angrepets utseende," in *Korrosjon og korrosjonsvern*, Second Edition ed. Norway: Tapir, 1994, pp. 89-202.

[14] D. R. Askeland, P. P. Fulay, and W. J. Wright, "Corrosion and Wear," in *The Science and Engineering of Materials SI*, Sixth ed. USA: Cengage Learning, 2011, pp. 851-887.

[15] J. R. Davis, "Understanding the Corrosion Behavior of Aluminum," in *Corrosion of aluminum and aluminum alloys*, First ed. USA: ASM International, 1999, pp. 25-43.

[16] J. R. Davis, "Intergranular and Exfoliation Corrosion," in *Corrosion of aluminum and aluminum alloys*, First ed. USA: ASM International, 1999, pp. 63-74.

[17] G. Svenningsen, J. E. Lein, A. Bjørgum, J. H. Nordlien, Y. Yu, and K. Nisancioglu, "Effect of low copper content and heat treatment on intergranular corrosion of model AlMgSi alloys," *Corrosion Science,* vol. 48, pp. 226-242, 2006, doi: https://doi.org/10.1016/j.corsci.2004.11.025.

[18] M. Stoknes, "Effect of Copper and Zinc on Corrosion Behaviour and Mechanical Properties in 6082-Alloys," Masters Thesis, Department of Materials Science and Engineering, Norwegian University of Science and Technology, Norway, 2015. [Online]. Available: https://ntnuopen.ntnu.no/ntnu-xmlui/handle/11250/2377266

[19] G. Svenningsen, M. H. Larsen, J. C. Walmsley, J. H. Nordlien & K. Nisancioglu, "Effect of artificial aging on intergranular corrosion of extruded AlMgSi alloy with small Cu content," *Corrosion Science,* vol. 48, pp. 1528-1543, 2006, doi: https://10.1016/j.corsci.2005.05.045.

[20] S. K. Kairy, P. A. Rometsch, C. H. J. Davies, and N. Birbilis, "On the Intergranular Corrosion and Hardness Evolution of 6xxx Series Al Alloys as a Function of Si:Mg Ratio, Cu Content, and Aging Condition," *Corrosion,* vol. 73, no. 10, pp. 1280-1295, 2017, doi: http://dx.doi.org/10.5006/2506.

[21] W. J. Liang, P. A. Rometsch, L. F. Cao, and N. Birbilis, "General aspects related to the corrosion of 6xxx series aluminium alloys: Exploring the influence of Mg/Si ratio and Cu," *Corrosion Science,* vol. 76, pp. 119-128, 2013, doi: http://dx.doi.org/10.1016/j.corsci.2013.06.035.

[22] N. E. Dowling, S. L. Kampe, and M. V. Kral, "Fatigue of Materials: Introduction and Stress-Based Approach," in *Mechanical Behavior of Materials*, Fifth ed. United Kingdom: Pearson Education, 2020, pp. 375-449.

[23] R. G. Budynas and J. K. Nisbett, "Fatigue Failure Resulting from Variable Loading," in *Shigley's Mechanical Engineering Design SI Units* Eleventh ed. USA: McGraw Hill Education, 2021, pp. 288-344.

[24] N. E. Dowling, S. L. Kampe, and M. V. Kral, "Fatigue Crack Growth," in *Mechanical Behavior of Materials*, Fifth ed. United Kingdom: Pearson Education, 2020, pp. 517-588.

[25] Y. Murakami, "Stress Concentration," in *Metal Fatigue: Effects of Small Defects and Nonmetallic Inclusions*, First ed. United Kingdom: Elsevier Science, 2002, pp. 11-24.

[26] K. Solberg, S. Guan, N. Razavi, T. Welo, K. C. Chan, and F. Berto, "Fatigue of additively manufactured 316L stainless steel: The influence of porosity and surface roughness," *Fatigue & Fracture of Engineering Materials & Structures,* vol. 42, no. 9, pp. 2043-2052, 2019, doi: https://doi.org/10.1111/ffe.13077.

[27] K. S. R. Chandran, "The finding of the reciprocal relationship between fatigue (S-N) behavior and fatigue crack growth behavior enabling interconversion of data in structural materials," *Materialia,* vol. 25, 2022, Art no. 101541, doi: https://doi.org/10.1016/j.mtla.2022.101541.

[28] C. Y. Kung. and M. E. Fine., "Fatigue Crack initiation and microcrack growth in 2024-T4 and 2124-T4 aluminum alloys," *Metallurgical Transactions A,* vol. 10A, pp. 603-610, 1979, doi: https://doi.org/10.1007/BF02658324.

[29] W. B. Shou, D. Q. Yi, H. Q. Liu, C. Tang, F. H. Shen, and B. Wang, "Effect of grain size on the fatigue crack growth behavior of 2524-T3 aluminum alloy," *Archives of Civil and Mechanical Engineering,* vol. 16, pp. 304-316, 2016, doi: https://doi.org/10.1016/j.acme.2016.01.004.

[30] N. E. Dowling, S. L. Kampe, and M. V. Kral, "Stress Based Approach to Fatigue: Notched Members," in *Mechanical Behavior of Materials*, Fifth ed. United Kingdom: Pearson Education, 2020, pp. 450-516.

[31] S. K. Ås, B. Skallerud, and B. W. Tveiten, "Surface roughness characterization for fatigue life predictions using finite element analysis," *International Journal of Fatigue,* vol. 30, no. 12, pp. 2200-2209, 2008, doi: https://doi.org/10.1016/j.ijfatigue.2008.05.020.

[32] N. Nanninga and C. White, "The relationship between extrusion die line roughness and high cycle fatigue life of an AA6082 alloy," *International Journal of Fatigue,* vol. 31, no. 7, pp. 1215-1224, 2009, doi: https://doi.org/10.1016/j.ijfatigue.2008.11.015.

[33] H. Luong and M. R. Hill, "The effects of laser peening and shot peening on high cycle fatigue in 7050-T7451 aluminum alloy," *Materials Science and Engineering: A,* vol. 527, no. 3, pp. 699-707, 2010, doi: https://doi.org/10.1016/j.msea.2009.08.045.

[34] M. Mhaede, "Influence of surface treatments on surface layer properties, fatigue and corrosion fatigue performance of AA7075 T73," *Materials & Design,* vol. 41, pp. 61-66, 2012, doi: https://doi.org/10.1016/j.matdes.2012.04.056.

[35] G. M. D. Almaraz, J. L. Á. Ambriz, and E. C. Calderón, "Fatigue endurance and crack propagation under rotating bending fatigue tests on aluminum alloy AISI 6063-T5 with controlled corrosion attack," *Engineering Fracture Mechanics,* vol. 93, pp. 119-131, 2012, doi: https://doi.org/10.1016/j.engfracmech.2012.06.012.

[36] M. Abdulstaar, M. Mhaede, and L. Wagner, "Pre-Corrosion and Surface Treatments Effects on the Fatigue Life of AA6082 T6," *Advanced Engineering Materials,* vol. 15, no. 10, pp. 1002-1006, 2013, doi: https://doi.org/10.1002/adem.201300054.

[37] M. Weber, P. D. Eason, H. Özdes, and M. Tiryakioglu, "The effect of surface corrosion damage on the fatigue life of 6061-T6 aluminum alloy extrusions," *Materials Science and Engineering: A,* vol. 690, pp. 427-432, 2017, doi: https://doi.org/10.1016/j.msea.2017.03.026.

[38] A. F. Munóz, J. L. M. Buenhombre, A. I. García-Diez, C. C. Fabal, and J. J. G. Díaz, "Fatigue Study of the Pre-Corroded 6082-T6 Aluminum Alloy in Saline Atmosphere," *Metals,* vol. 10, no. 9, 2020, doi: https://doi.org/10.3390/met10091260.

[39] *EN ISO 11846: Corrosion of metals and alloys*, E. Standard, 2008.

[40] J. V. Jakobsen, "Microstructure and Mechanical Properties of Welded AA6082 Aluminium Alloys," Masters Thesis, Materials Science and Engineering, Norwegian University of Science and Technology, Norway, 2016. [Online]. Available: https://ntnuopen.ntnu.no/ntnu-xmlui/handle/11250/2406949

[41] J. K. Solberg, *Lysmikroskopi*. Norway: Department of Materials Science and Engineering, NTNU, 2011.

[42] K. Geels, "Mounting," in *Metallographic and Materialographic Specimen Preparation, Light Microscopy, Image Analysis and Hardness Testing*. USA: ASTM International, 2007, pp. 54-79.

[43] Struers. *Active Oxide Polishing Suspensions*. [Online]. Available: https://www.struers.com/-/media/Library/Brochures/English/Active-Oxide-Polishing.pdf

[44] K. Geels, "Hardness Testing," in *Metallographic and Materialographic Specimen Preparation, Light Microscopy, Image Analysis and Hardness Testing*. USA: ASTM International, 2007, pp. 623-648.

[45] Y. Huang, X. Ye, B. Hu, and L. Chen, "Equivalent crack size model for pre-corrosion fatigue life prediction of aluminum alloy 7075-T6," *International Journal of Fatigue,* vol. 88, 2016, doi: https://doi.org/10.1016/j.ijfatigue.2016.03.035.

[46] G. Stachowiak and A. W. Batchelor, "Fundamentals of Contact Between Solids," in *Engineering Tribology*, Third ed. USA: Elsevier, 2005, pp. 461-495.

[47] K. Geels, "Electron Microscopy - Scanning Probe Microscopy," in *Metallographic and Materialographic Specimen Preparation, Light Microscopy, Image Analysis and Hardness Testing*. USA: ASTM International, 2007, pp. 558-564.

[48] A. Nanakoudis. "SEM: Types of Electrons and the Information They Provide." ThermoFisher Scientific. https://www.thermofisher.com/blog/materials/sem-signal-types-electrons-and-the-information-they-provide/ (accessed May 2024).

[49] J. G. Kaufman, "Understanding the Aluminum Temper Designation System," in *Introduction to Aluminum Alloys and Tempers*. USA: ASM International, 2000, pp. 39-76.

[50] E. J. Dolley, B. Lee, and R. P. Wei, "The effect of pitting corrosion on fatigue life," *Fatigue & Fracture of Engineering Materials & Structures,* vol. 23, pp. 555-560, 2000, doi: https://doi.org/10.1046/j.1460-2695.2000.00323.x.

[51] J. Toribio, B. Gonzáles, J. Matos, and Ó. Mulas, "Stress Intensity Factors for Embedded, Surface, and Corner Cracks in Finite-Thickness Plates Subjected to Tensile Loading," *Materials,* vol. 14, no. 11, 2021, Art no. 2807, doi: https://doi.org/10.3390/ma14112807.

Appendix A: Test Matrix

Specimen	Surface condition	Corrosion duration [h]	Micro-structure	Hardness	Corrosion depth	Surface topography	Post-fatigue surface	Fatigue	SEM: Failure mechanism	SEM: Surface features	SEM: Striations	SEM: Defect area
Ref1	Extruded	0						X				X
Ref2	Extruded	0						X				X
Ref3	Extruded	0					X	X	X		X	X
0	Extruded	0	X	X		X						
I	Extruded	12			X	X						
II	Extruded	12						X	X			X
III	Extruded	12						X				X
IV	Extruded	12						X				X
V	Extruded	24	X		X	X						
VI	Extruded	24					X	X	X			X
VII	Extruded	24						X				X
VIII	Extruded	24						X				X
IX	GBB	12			X	X						
X	GBB	12						X				X
XI	GBB	12						X				X
XII	GBB	12						X	X	X		X
XIII	GBB	24			X	X						
XIV	GBB	24						X				X
XV	GBB	24						X				X
XVI	GBB	24					X	X	X	X		X
XVII	GBB	0					X	X	X	X		X
XVIII	GBB	0						X				X
XIX	GBB	0						X				X
XX	GBB	0	X	X		X	X					
XXI	Extruded	1			X	X						
XXII	Extruded	1						X				X
XXIII	Extruded	1						X	X			X
XXIV	Extruded	1						X				X
XXV	Extruded	4			X	X						
XXVI	Extruded	4						X				X
XXVII	Extruded	4						X				X
XXVIII	Extruded	4						X	X			X

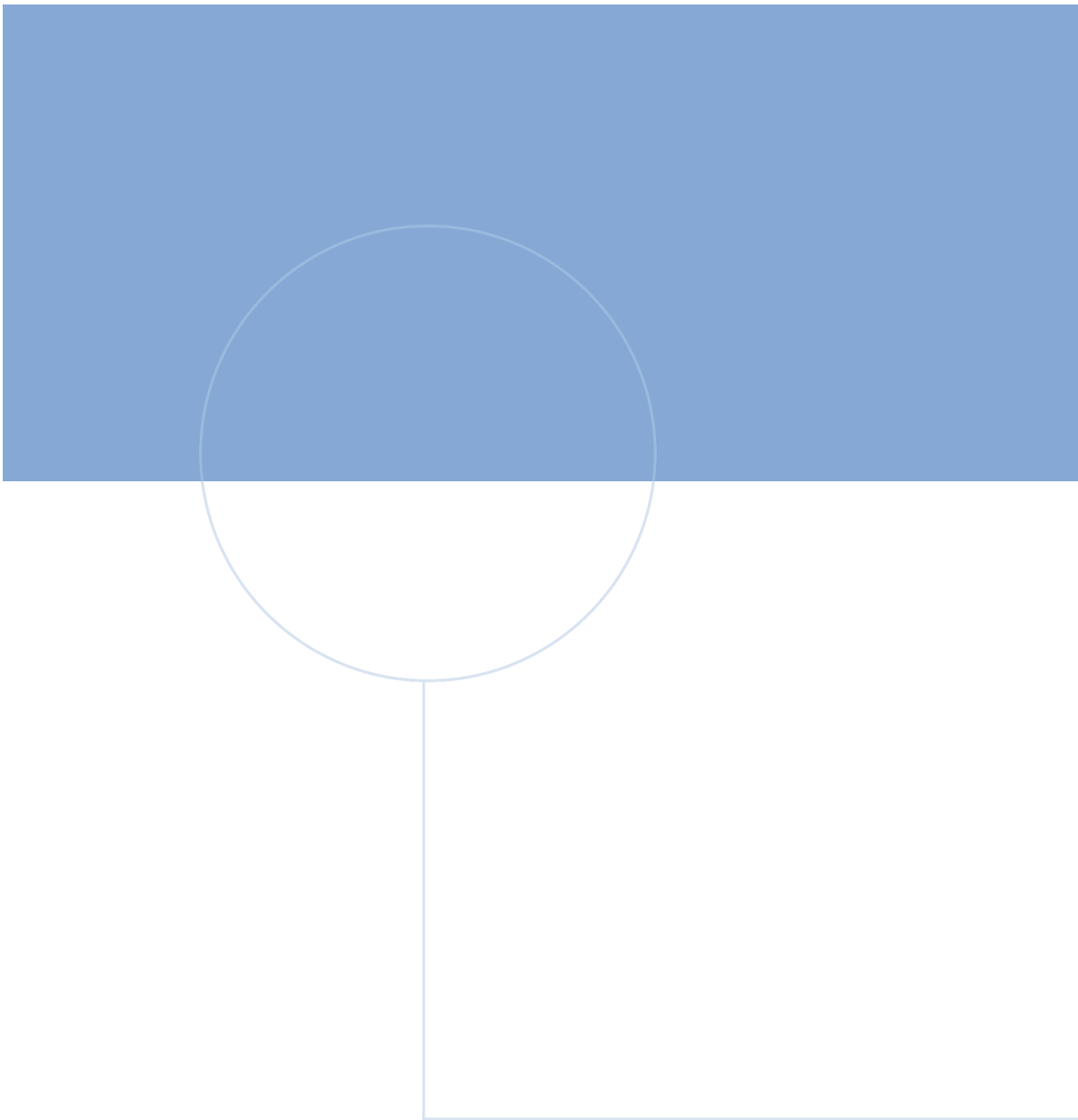

NTNU

Norwegian University of
Science and Technology